

# *FUSE* and *STIS* Observations of the Warm-Hot Intergalactic Medium towards PG 1259+593<sup>1</sup>

Philipp Richter<sup>2</sup>, Blair D. Savage<sup>3</sup>, Todd M. Tripp<sup>4,5</sup>

and

Kenneth R. Sembach<sup>6</sup>

## ABSTRACT

We use *Far Ultraviolet Spectroscopic Explorer* (FUSE) and *Space Telescope Imaging Spectrograph* (STIS) spectra to study intergalactic absorption towards the quasar PG 1259+593 ( $z_{\text{em}} = 0.478$ ), with a particular emphasis on the warm-hot intergalactic medium (WHIM). The combined FUSE and STIS spectrum of PG 1259+593 covers the full wavelength range between 905 and 1730 Å at a spectral resolution of  $\sim 25 \text{ km s}^{-1}$  for the FUSE bandpass ( $\lambda \leq 1180 \text{ Å}$ ) and  $\sim 7 \text{ km s}^{-1}$  for the STIS range ( $\lambda > 1150 \text{ Å}$ ). The signal-to-noise ratios (S/N) per resolution element are  $\sim 10 - 30$  (FUSE) and  $\sim 7 - 17$  (STIS). We identify 135 intergalactic absorption lines with equivalent widths  $\geq 10 \text{ mÅ}$ , tracing 78 absorption components in 72 Ly  $\alpha$ /Ly  $\beta$  absorption-line systems. Metal-line absorption by species such as C III, C IV, O III, O IV, O VI, and Si III is clearly detected in four systems, and is possibly seen in four additional cases. We study the distribution and physical properties of the WHIM as sampled by O VI and intrinsically broad Ly  $\alpha$  lines. The number of intervening O VI absorbers for equivalent widths  $W_{\lambda} \geq 24 \text{ mÅ}$  is 3 – 6 over an unobscured redshift path of  $\Delta z \approx 0.368$ . This implies a number density of O VI systems,  $dN_{\text{OVI}}/dz$ , of  $\sim 8 - 16$  above this equivalent width limit along this sight line. A seventh intervening O VI absorber is possibly detected with  $W_{\text{r}}(\text{O VI}) \approx 15 \text{ mÅ}$ . The range of  $dN_{\text{OVI}}/dz = 8 - 16$  for  $W_{\lambda} \geq 24 \text{ mÅ}$  is consistent with estimates from other sight lines, supporting the idea that intervening intergalactic O VI absorbers contain a substantial fraction of the baryonic mass in the low-redshift Universe. We identify a number of broad Ly  $\alpha$  absorbers with large Doppler parameters ( $b \sim 40 - 200$

---

<sup>1</sup>Based partly on observations with the NASA/ESA *Hubble Space Telescope* obtained at the Space Telescope Science Institute, which is operated by the Association of Universities for Research in Astronomy, Inc., under NASA contract NAS 5-26555.

<sup>2</sup>Institut für Astrophysik und Extraterrestrische Forschung, Universität Bonn, Auf dem Hügel 71, 53121 Bonn, Germany

<sup>3</sup>Department of Astronomy, University of Wisconsin-Madison, 475 N. Charter St., Madison, WI 53706, USA

<sup>4</sup>Princeton University Observatory, Peyton Hall, Ivy Lane, Princeton, NJ 08544, USA

<sup>5</sup>Department of Astronomy, University of Massachusetts, Amherst, MA 01003, USA

<sup>6</sup>Space Telescope Science Institute, 3700 San Martin Drive, Baltimore, MD 21218, USA

$\text{km s}^{-1}$ ) and low column densities ( $N(\text{H I}) < 10^{14} \text{ cm}^{-2}$ ). For pure thermal broadening, these widths correspond to temperatures of  $\sim 1 \times 10^5 - 3 \times 10^6 \text{ K}$ . While these broad absorbers could be caused by blends of multiple, unresolved lines, continuum undulations, or by kinematic flows and Hubble broadening, we consider the possibility that some of these features are single-component, thermally broadened  $\text{Ly } \alpha$  lines. These systems could represent WHIM absorbers that are too weak, too metal-poor, and/or too hot to be detected in O VI. If so, their widths and their frequency in the PG 1259+593 spectrum imply that these absorbers trace an even larger fraction of the baryons in the low-redshift Universe than the O VI absorbing systems. A thermal Doppler broadening explanation for one of these broad features is supported by the probable detection of O VI near the velocity of a broad  $\text{Ly } \alpha$  and  $\text{Ly } \beta$  absorber with an O VI line width  $\sim 4$  times smaller than for H I.

## 1. Introduction

The analysis of absorption lines in the local and distant intergalactic medium (IGM) towards extragalactic background sources such as quasars (QSOs) and active galactic nuclei (AGNs) has become an important research area to investigate the gaseous environment of galaxies and galaxy-clusters, and to study the large scale structure, the chemical evolution and the baryonic content of the IGM. The most sensitive tracer to follow the distribution and evolution of the IGM from high to low redshifts is the  $\text{Ly } \alpha$  line of neutral hydrogen. A large number of  $\text{Ly } \alpha$  lines occur along a typical QSO sight line, resulting in the “ $\text{Ly } \alpha$  forest” (e.g., Rauch 1998; Lu et al. 1996). For the low-redshift Universe, the observation of intergalactic  $\text{Ly } \alpha$  absorption requires space-based instrumentation, such as the former *Goddard High Resolution Spectrograph* (GHRS) and the more recently deployed *Space Telescope Imaging Spectrograph* (STIS), both installed on the *Hubble Space Telescope* (HST). For higher redshifts ( $z > 1.6$ ), ground based 8 m-class telescopes such as Keck and the *Very Large Telescope* (VLT) provide a wealth of information about the  $\text{Ly } \alpha$  forest in the early Universe (e.g., Kim et al. 2002). It is generally accepted that at  $z = 3$  almost all of the baryons in the Universe are located in the highly-ionized  $\text{Ly } \alpha$  forest (Rauch et al. 1997; Weinberg et al. 1997), whereas at lower redshifts an increasing fraction of the baryons may reside in a low-density, shock-heated component at temperatures between  $10^5$  to  $10^7 \text{ K}$ , the so-called warm-hot intergalactic medium (WHIM). In the local Universe (i.e., near  $z = 0$ ), the WHIM may contain as much as 30 to 40 percent of the baryons (e.g., Cen & Ostriker 1999). In comparison, the  $\text{Ly } \alpha$  forest at  $z = 0$  probably contains about 20 percent of the baryons (Penton, Shull & Stocke 2000). Detecting the WHIM phase at low redshifts is a challenging task. Absorption spectroscopy of the O VI doublet ( $\lambda\lambda 1031.9, 1037.6$ ) currently provides one of the best diagnostics to study the warm phase ( $10^5 - 10^6 \text{ K}$ ) of the WHIM at low redshift. However, observing O VI in the low-redshift IGM requires space-based high-resolution spectrographs such as STIS and the *Far Ultraviolet Spectroscopic Explorer* (FUSE) together with a substantial amount of observing time (e.g., Tripp, Savage & Jenkins 2000; Savage et al. 2002). Due to these instrumental restrictions, the number of sight-lines that have been analyzed

for O VI absorption at  $z < 1$  unfortunately is still very limited. So far, intervening WHIM O VI absorption for  $z < 1$  in FUSE and STIS data has been found towards H 1821+643 (Tripp, Savage & Jenkins 2000; Oegerle et al. 2000), PG 0953+415 (Tripp & Savage 2000; Savage et al. 2002), and PKS 0405–123 (Chen & Prochaska 2000). Together with the non-detections or marginal and weak detections reported for the sight lines towards PG 0804+761 (Richter et al. 2001a) and 3C 273 (Sembach et al. 2001), the current data imply a number of intervening O VI absorbers per unit redshift of  $dN_{\text{OVI}}/dz = 14^{+9}_{-6}$  for restframe equivalent widths  $W_r \geq 50 \text{ m}\text{\AA}$  at  $\langle z \rangle = 0.09$  (Savage et al. 2002). Assuming that the average metallicity of these absorbers is 0.1 solar, the cosmological mass density in the units of the current critical density is  $\Omega_b(\text{O VI}) \geq 0.002h_{75}^{-1}$ . Clearly, additional observations with FUSE and STIS are desired to improve the statistics on the intervening O VI absorbers, and to gain new insights about their physical properties (e.g., their ionization properties) and their metal abundances. For those absorbers that cannot be detected in O VI absorption (e.g., if the overall column density is too low, the metallicity is too low, or the temperature is too high), other tracers have to be used to study the warm-hot intergalactic gas phase. X-ray observations with *Chandra* and *XMM-Newton* (e.g., Rasmussen, Kahn, & Paerels 2003; Fang et al. 2002) hold the prospect of improving our understanding of the distribution and physical properties for the million-degree phase of the WHIM, which may contain the dominating fraction of the baryons at low redshifts. However, detecting X-ray signatures such as O VII and O VIII absorption from the low-redshift IGM is difficult with current instrumentation, and so far the information about the intergalactic X-ray forest is relatively sparse. For high-metallicity, high-column density absorbers, one may search for FUV absorption by Ne VIII  $\lambda\lambda 770.4, 780.3$ . But due to the relatively low cosmic abundance of Ne, Ne VIII is not expected to be a sensitive tracer for the WHIM in the low-redshift Universe. A promising approach to study the WHIM at low redshifts is to search for broad Ly  $\alpha$  lines. For pure thermal broadening, Ly  $\alpha$  absorbers with Doppler parameters exceeding  $b \approx 40 \text{ km s}^{-1}$  sample WHIM gas with temperatures  $T > 10^5 \text{ K}$ . There are some compelling detections of broad Ly  $\alpha$  lines at low redshifts (e.g., Tripp et al. 2001), but generally broad Ly  $\alpha$  lines are difficult to identify and analyze due to continuum placement uncertainties, line-blending problems, and relatively low signal-to-noise ratios in existing data.

In this paper we investigate intervening intergalactic absorption by H I, O VI and other species with FUSE and STIS in direction of the bright QSO PG 1259+593 ( $V = 15.84$ ;  $z_{\text{em}} = 0.478$ ;  $l = 120^\circ.6$ ,  $b = +58^\circ.1$ ). FUSE and STIS data of PG 1259+593 have been extensively used to study abundances and physical conditions in Galactic halo gas in this direction (Richter et al. 2001b; Collins, Shull & Giroux 2003; Sembach et al. 2004; Fox et al. 2004). With more than 600 ks of integration time it represents one of the prime objects of the FUSE mission. The line of sight towards PG 1259+593 samples several strong Ly  $\alpha$  systems, as shown by low-resolution *Faint Object Spectrograph* (FOS) data (Bahcall et al. 1993). The goal of this paper is to present an overview of the intergalactic absorption towards PG 1259+593, to identify the main absorption systems, to perform a first, basic analysis of these absorbers, and to search for the WHIM absorbers that may contain an important fraction of the baryonic mass in the low-redshift Universe. The outline of this paper is the following: in §2 we review the observations and the data reduction process. The analysis of

intergalactic absorption is presented in §3. In §3 we also describe the properties of the individual absorption systems and derive statistical information about the IGM towards PG 1259+593. We discuss our results in §4 and summarize our study in §5.

## 2. Observations and Data Reduction

### 2.1. FUSE Observations

FUSE observations of PG 1259+593 were carried out between February 2000 and March 2001 in various individual observation-runs. For a detailed description about the FUSE instrument and its performance in space see Moos et al. (2000) and Sahnou et al. (2000). Table 1 provides basic information about the individual FUSE data sets. PG 1259+593 was observed through the large (LWRS,  $30''.0 \times 30''.0$ ) aperture in the photon-address mode, which stores X/Y location, arrival time, and pulse-height of each detection as a photon list. The 236 exposures of PG 1259+593 provide a total of  $\sim 630$  ks of integration time. The raw data were processed with the standard FUSE reduction pipeline (CALFUSE v2.2.2). Extra care was taken to screen the raw data for possible particle event bursts, Earth limb avoidance, South Atlantic Anomaly passage, and pulse height distribution constraints. Summed exposure lists for each of the four FUSE channels (LiF 1, LiF 2, SiC 1, SiC 2) were created and corrected for geometric distortions, Doppler shifts, grating motions, astigmatism, detector backgrounds, and scattered light effects. The data were further flux calibrated and wavelength calibrated to a heliocentric velocity scale. The zero point of the FUSE wavelength scale was adjusted to that of the (more accurate) STIS wavelength scale by comparing the velocity scale of narrow interstellar absorption lines from atomic species such as Fe II and Si II in both the FUSE and the STIS wavelength range (see Sembach et al. 2004 for details). The average flux in the FUSE spectrum, which covers the wavelength range between 905 and 1187 Å, is  $\sim 2 \times 10^{-14}$  erg cm $^{-2}$  s $^{-1}$  Å $^{-1}$ . Note that the current FUSE flux calibration for PG 1259+593 does not account for the occurrence of dark horizontal stripes in the detector images that reduce the total flux in specific wavelength regions (see Fig. 1). The spectral resolution in the FUSE data is  $\sim 22 - 25$  km s $^{-1}$  at a rebinned pixel size of  $\sim 7.5$  km s $^{-1}$ . The signal-to-noise ratio (S/N) in the night+day FUSE data of PG 1259+593 data varies between 10 and 30 per spectral resolution element. A more detailed description of the FUSE data reduction of PG 1259+593 is provided in Sembach et al. (2004).

### 2.2. STIS Observations

STIS observations of PG 1259+593 were obtained in January and December 2001 (see Table 1) using the intermediate-resolution (FWHM  $\sim 7$  km s $^{-1}$ ) echelle far-UV grating (E140M) and the  $0''.2 \times 0''.06$  slit. The STIS data cover the wavelength range between 1150 and 1729 Å with small gaps between the echelle orders at wavelengths  $> 1634$  Å. The pixel size in the data is  $\sim 3.5$  km s $^{-1}$ .

Detailed information about the STIS instrument is provided by Woodgate et al. (1998), Kimble et al. (1998) and Leitherer et al. (2002). The PG 1259+593 STIS data were reduced following the individual steps described by Tripp et al. (2001). The data reduction includes a two-dimensional scattered light correction (Landsman & Bowers 1997; Bowers et al. 1998). Individual extracted flux-calibrated spectra were co-added together (weighted by their inverse variances averaged over a large region of the spectrum) to produce the final composite spectrum in a heliocentric velocity scale. Hot pixels that occasionally occur in the calibrated STIS data have been corrected for by interpolating between adjacent pixels. The resulting S/N per resolution element in the STIS data varies between  $\sim 7$  and 17. The highest S/N region in the STIS data occurs near 1400 Å.

### 2.3. Data Analysis

The combined FUSE and STIS spectrum of PG 1259+593 is shown in Fig. 1. More than 200 absorption features are seen in the FUSE and STIS data of PG 1259+593; these features are identified in Figs. 2–12. Wavelengths and oscillator strengths ( $f$  values) have been adopted from the compilations of Morton (2003, 1991) and Verner et al. (1994); they are listed in Table 2. Since both resolution and S/N is varying along the spectrum, typical  $3\sigma$  detection limits range from  $\sim 15$  to  $\sim 50$  mÅ. In a first step we have separated intergalactic absorption lines from local foreground absorption by the interstellar medium in the disk and halo of the Milky Way. The interstellar spectrum (FUSE and STIS) in the direction of PG 1259+593 is discussed in detail by Richter et al. (2001b) and Sembach et al. (2004). Interstellar absorption consists of three main velocity components located near  $v_{\text{LSR}} = -2$ ,  $-55$  and  $-129$  km s $^{-1}$  (Sembach et al. 2004), representing local Milky Way disk gas, gas from the Intermediate Velocity Arch (IV Arch), and gas from high-velocity cloud Complex C, respectively (note that  $v_{\text{LSR}} = v_{\text{helio}} + 10.5$  km s $^{-1}$  in this direction). Each of these velocity components have to be considered carefully for possible blending problems with intergalactic absorption. Stronger interstellar absorption features (with equivalent widths  $\geq 30$  mÅ, typically) have been marked with star symbols in the spectrum plots of PG 1259+593 in Figs. 2–12. After dealing with the interstellar absorption features, we have identified 135 intergalactic absorption lines from 78 individual absorption components in 72 different absorption systems (see next section for details). We have measured wavelengths and redshifts by fitting Voigt profiles (convolved with Gaussian instrumental profiles corresponding to the spectral resolution of the two instruments; see §2.1 and §2.2) to the absorption lines. Normalized velocity profiles have been created by fitting low-order polynomials to the (generally slightly varying) continuum flux of PG 1259+593 and transforming each absorption profile into a restframe velocity scale. Restframe equivalent widths,  $W_r$ , have been measured for each line by a pixel integration over the normalized velocity profile. Column densities have been derived by three different methods: if multiple lines from a species are available in a system (e.g., multiple H I Lyman series lines), we have constructed curves of growth (COG) from the measured equivalent widths and derived logarithmic column densities,  $\log N$ , and Doppler-parameters ( $b$  values). For these multi-line systems, the various Lyman series lines are located in both the higher-resolution STIS wavelength band and the lower-resolution FUSE regime,

thus in regions where different instrumental line spread functions apply. Here, the COG analysis (which requires only the equivalent width for each line as input parameter) represents a very robust method to determine column densities and  $b$  values for this inhomogeneous set of absorption lines. Moreover, the COG method allows to directly visualize the influence of outliers (e.g., lines that are partly blended) for deriving  $\log N$  and  $b$  for a multi-line system, and thus provides an important tool to estimate realistic uncertainties for these parameters. In some systems, we have fitted single lines from selected ions to curves of growth with  $b$  values previously derived for other species. In addition, we have used the apparent optical depth (AOD) method (see Savage & Sembach 1991 for a detailed description) in a number of cases to derive logarithmic column densities by integrating over the normalized velocity profiles of mostly unsaturated lines. Finally, we have determined  $\log N$  and  $b$  by Voigt-profile fitting of high S/N IGM lines located in the higher resolution STIS wavelength range. This method was preferred to derive column densities and  $b$  values for H I in the metal-line systems and the Ly  $\alpha$  forest, except for those absorbers that consist of a large number of Lyman series lines and for which the COG method was used.

Our measurements are compiled in Tables 3 – 6. Formal  $1\sigma$  errors for  $W_r$ ,  $\log N$ , and  $b$  are based on photon-statistics and continuum placement constraints. The combined use of the different methods for deriving  $N$  allows to check upon the possible existence of systematic errors that cannot be accounted for in the formal error estimate for each method. Such possible systematic errors could be unexpected continuum undulations, unresolved and unidentified line blending, unknown instrumental features, and fixed-pattern noise. Values for  $\log N$  derived by the different methods usually agree well within their formal  $2\sigma$  error range (see Table 3). However, for the Ly  $\alpha$  and Ly  $\beta$  forest lines a reliable identification and analysis of weak and broad absorption features is particularly difficult if such effects are present. In addition to the formal errors provided in Tables 3, 5 and 6 we therefore give an additional “reliability status” for those lines for which we see evidence that the estimates for  $\log N$  and  $b$  (and their formal errors) could be incorrect due to one of the effects listed above. Typical problematic cases are: stronger lines that show asymmetries or weak wings, weak lines that have unidentified features and undulations in the adjacent continuum, and apparently broad lines that show evidence that they are composed of several, unresolved sub-components. In Table 3 we flag those lines with the note “uncertain” in the last column. Similarly, we list in the seventh column of Table 5 the status of a Ly  $\alpha$  forest line as either OK or UC (uncertain).

### 3. Intergalactic Absorption

#### 3.1. Overview

For the 135 intergalactic absorption lines detected towards PG 1259+593 we have identified 72 corresponding absorption systems at redshifts between 0.002 and 0.436. Note that some of the identifications have to be considered as tentative due to the fact that some features have low S/N and/or they occur in regions where line blending problems do not allow unambiguous identifications.

These lines have been marked with question marks in Figs. 2–12. Six of the 72 systems consist of two sub-components each, so that the spectrum consists of 78 IGM absorption components in total. For these sub-components (in Tables 3, 4 and 5 given as “Component A” and “Component B”) we have measured column densities and  $b$  values separately. Of the identified 72 systems, four to eight are metal line systems detected in one or more lines of C III, C IV, O III, O IV, O VI, Si III, and possibly Ne VIII. These systems will be discussed in detail in §3.2. Rest-frame equivalent widths, column densities,  $b$  values, and other information for each system are listed in Table 3. Table 4 summarizes the column densities of the metal-line absorbers (note that all metal line systems detected towards PG 1259+593 have H I column densities  $\log N(\text{H I}) \geq 13.6$ ). Fourteen additional absorption systems are detected solely in H I in two or more lines from the Lyman series (Ly  $\alpha$ –Ly  $\epsilon$ ), but without corresponding metal lines. Also for these systems we list restframe equivalent widths, column densities, etc. in Tables 3 and 4, while their properties are discussed in §3.4. Finally, we find 50 absorbers detected only in one single line, which we generally assume to be Ly  $\alpha$ . Since the given wavelength limit ( $\lambda \leq 1729 \text{ \AA}$ ) does not allow us to detect Ly  $\alpha$  absorption for redshifts  $0.422 \leq z \leq 0.478$ , some of the lines between  $1458 \text{ \AA}$  and  $1516 \text{ \AA}$  identified as Ly  $\alpha$  may be actually Ly  $\beta$  belonging to Ly  $\alpha$  absorption outside the wavelength range of the STIS data. Without having additional high-resolution spectral data for  $\lambda > 1729 \text{ \AA}$ , however, we are not able to clarify the line identification for this redshift range at this point. The Ly  $\alpha$ /Ly  $\beta$  forest is discussed in detail in §3.4 and §3.5. Redshifts, logarithmic H I column densities and  $b$  values of the 50 systems seen solely in Ly  $\alpha$  absorption are given in Table 5. There is a good qualitative match between the high-resolution STIS data presented here and the low resolution (FWHM  $\sim 1 - 2 \text{ \AA}$ ) FOS data of PG 1259+593 (Bahcall et al. 1993). Bahcall et al. identified eight strong Ly  $\alpha$  absorbers (their Table 6) along the total redshift path towards PG 1259+593. These identifications coincide with the absorption systems at  $z = 0.04606, 0.08933, 0.21949, 0.22313, 0.28335, 0.29236, 0.43148$  and  $0.43569$  detected in the STIS spectrum (see Table 4).

### 3.2. Metal-Line Systems

#### 3.2.1. The System at $z = 0.00229$

This system (see Fig. 13) has the lowest redshift of all absorbers and is most likely related to the galaxy UGC 08146 ( $z = 0.00224$ ; see also §3.6.2). The absorber is detected in Ly  $\alpha$  and Ly  $\beta$ , and possibly in O VI  $\lambda 1031.9$ . The Ly  $\alpha$  absorption of this systems lies in the wing of the strong interstellar Ly  $\alpha$  absorption and therefore has a relatively low S/N. A profile fit yields  $\log N(\text{H I}) = 13.57 \pm 0.10$  and  $b = 42.1 \pm 4.4 \text{ km s}^{-1}$ . Using the relation between the Doppler parameter,  $b$ , and the temperature,  $T$ ,

$$b = 0.129 \sqrt{\frac{T}{A}} \text{ km s}^{-1} \quad (1)$$

(with  $A$  being the atomic weight for the element), this  $b$  value corresponds to  $T \leq 1.1 \times 10^5$  K. The temperature could be significantly lower than  $1.1 \times 10^5$  K if effects like turbulent gas motions, gas flows and unresolved sub-component structure contribute to the total breadth of the line<sup>1</sup>. O VI  $\lambda 1031.9$  absorption is possibly detected with  $\log N(\text{O VI}) = 13.73 \pm 0.14$ . Using the formal error calculation, the significance of the line is  $2.9\sigma$  (see §2.3 and Table 3); however, the absorption appears to be exceptionally broad (ranging from approximately  $-110$  to  $+120$   $\text{km s}^{-1}$ ) and we thus cannot exclude that this feature is an unexpected continuum undulation rather than O VI at  $z = 0.00229$ . We regard this case as a tentative intervening O VI detection. If the feature is produced by O VI, the absorption may have a multicomponent structure with the part of the absorption between  $-100$  and  $+50$   $\text{km s}^{-1}$  associated with the H I Ly  $\alpha$  absorption, and the more extended absorption from  $+50$  to  $+120$   $\text{km s}^{-1}$  occurring where H I absorption is not detected. Such multicomponent O VI and H I absorbers have been seen in STIS spectra of the QSO H 1821+643 ( $z_{\text{em}} = 0.297$ ) by Tripp et al. (2000). There is a possible H I absorption component near  $-240$   $\text{km s}^{-1}$  seen in Ly  $\alpha$ , but its significance is low ( $\sim 2.7\sigma$ ) due to the low S/N in the vicinity of the ISM Ly  $\alpha$  absorption. At this radial velocity, the feature would have  $z \approx 0.0015$  or  $v_{\text{rad}} = +450$   $\text{km s}^{-1}$  (in the heliocentric velocity frame), and thus might correspond to gas located in the Local Group. Unfortunately, possible O VI  $\lambda 1031.9$  absorption at this velocity is totally blended by Ly  $\beta$  at  $z = 0.00760$  (see next subsection).

### 3.2.2. The System at $z = 0.00760$

The absorption system at  $z = 0.00760$  (see Fig. 13) is detected in H I Ly  $\alpha$ , Ly  $\beta$ , and possibly O VI  $\lambda 1031.9$ . From a profile fit of the Ly  $\alpha$  absorption we obtain  $\log N(\text{H I}) = 14.05 \pm 0.05$  and  $b = 34.6 \pm 2.0$   $\text{km s}^{-1}$ . The  $b$  value implies  $T \leq 7.2 \times 10^4$  K (see previous subsection). The Ly  $\alpha$  absorption shows a wing at positive velocities, suggesting the presence of a weak second component near  $+60$   $\text{km s}^{-1}$ . Weak O VI  $\lambda 1031.9$  absorption is possibly detected in this system near  $1039.8$  Å at a column density of  $\log N(\text{O VI}) = 13.06 \pm 0.04$  (AOD method). The formal significance of this detection is  $3.8\sigma$  for the LiF 1A channel and  $1.8\sigma$  for the LiF 2B channel (see Table 3). However, the absorption unfortunately occurs in a wavelength region of the FUSE instrument where detector features are commonly observed (in particular in the LiF 1A channel). With an equivalent width of  $W_r \approx 15$  mÅ for the O VI  $\lambda 1031.9$  line, no detectable absorption is expected (and observed) to occur in the weaker O VI  $\lambda 1037.6$  line which could confirm the presence of O VI at  $z = 0.00760$ . Due to the very small equivalent width of the possible O VI absorption and the possible presence of detector features in the region where O VI at  $z = 0.00760$  is expected we regard this system as a tentative intervening O VI absorber.

---

<sup>1</sup>We will use equation (1) throughout this paper to estimate upper limits for  $T$  from measurements of Doppler parameters.



### 3.2.3. The System at $z = 0.04606$

This is one of the the two more complex metal-line systems towards PG 1259+593 (together with the system at  $z = 0.21949$ ). Absorption is seen in the first eight lines of the H I Lyman series (Ly  $\alpha$  to Ly  $\theta$ ), and in C III, Si III, C IV, and O VI (Fig. 14 and Table 3). A two-component structure is present (see, for instance, the absorption profiles of H I Ly  $\beta$  and C III), with the stronger component at  $0 \text{ km s}^{-1}$  in the  $z = 0.04606$  restframe (Component A) and the weaker one near  $+95 \text{ km s}^{-1}$  (Component B). Both components are present in H I Ly  $\alpha$ –Ly  $\delta$ , C III, and O VI  $\lambda 1031.9$ , but for Si III and C IV  $\lambda 1548.2$  line blends hamper the analysis of the positive-velocity component. The profiles of the H I lines reveal internal substructure within Component A. Component B appears to be a combination of a narrow and broad absorption components. With an H I column density of  $\log N(\text{H I}) = 15.81 \pm 0.08$  and a  $b$  value of  $33.2_{-5.1}^{+6.5} \text{ km s}^{-1}$  (from a curve-of-growth analysis; see Table 3) Component A represents the strongest IGM Ly  $\alpha$  absorber along this sight line. Having eight H I lines available in this system and a two-component structure that introduces significant uncertainties for the Voigt-profile fitting, we prefer the curve-of-growth technique to obtain values for  $\log N$  and  $b$  for the H I in this absorption system. The logarithmic column densities in Component A for the two intermediate ions C III and Si III are  $13.80 \pm 0.04$  and  $12.74 \pm 0.07$ , respectively (AOD method). The C IV absorption ( $\log N(\text{C IV}) = 13.61 \pm 0.08$ ; AOD) appears to be quite narrow, and is offset towards positive velocities (near  $+25 \text{ km s}^{-1}$ ) compared to the low ions and the H I ( $0 \text{ km s}^{-1}$ ). Note that unresolved saturation may possibly be affecting these C III, Si III, and C IV column density estimates. The O VI  $\lambda 1031.9$  absorption in Component A ( $\log N(\text{O VI}) = 13.68 \pm 0.05$ ; AOD) is broader than the C IV absorption and merges at positive velocities into an almost equally strong O VI absorption in Component B (see below). The O VI  $\lambda 1037.6$  line unfortunately has very low S/N (only the less sensitive SiC 1A channel is available for this line; see Fig. 4) and thus does not provide any further information on the O VI absorption in either Component A or Component B. The  $b$  value for the H I Lyman series in Component A ( $33.2 \text{ km s}^{-1}$ ) suggests  $T \leq 6.5 \times 10^4 \text{ K}$ . The presence of C III, Si III, C IV, and O VI absorption implies that Component A is a multi-phase absorber, possibly having a cooler interior surrounded by a high-temperature envelope. Due to the complexity of this system and the relatively low S/N in the data we refrain from performing a more detailed modelling of Component A.

The H I column density for Component B is  $\log N(\text{H I}) = 14.56 \pm 0.15$  (COG), thus significantly lower than for Component A. While the lines of Si III  $\lambda 1206.5$  and C IV  $\lambda 1548.2$  are blended by other IGM lines, C III absorption is clearly present ( $\log N(\text{C III}) = 13.42 \pm 0.04$ ; AOD method). Also the somewhat noisy C IV  $\lambda 1550.8$  line shows a weak absorption component near  $+95 \text{ km s}^{-1}$ . This feature, however, corresponds only to a  $1.7\sigma$  significance, so that we only can place an upper limit of  $\log N(\text{C IV}) \leq 13.64$ . O VI  $\lambda 1031.9$  absorption in Component B ( $\log N(\text{O VI}) = 13.63 \pm 0.06$ ; AOD) is nearly as strong as in Component A (again, no significant absorption is seen in the much noisier O VI  $\lambda 1037.6$  line; see above). The values of  $N(\text{H I})/N(\text{O VI})$  in Components A and B are 135 and 8.5, respectively. This ratio has been observed to range from  $\sim 0.1$  to 100 which suggests that although H I and O VI are observed to be coupled kinematically, the two species often arise in quite

different gaseous phases (Shull 2003).

### 3.2.4. The System at $z = 0.21949$

This is the second of the two more complex metal-line absorption systems (the  $z = 0.04606$  system being the other). Absorption is seen in eight lines of the H I Lyman series (Ly  $\alpha$ –Ly  $\epsilon$  and Ly  $\eta$ –Ly  $\iota$ ; Ly  $\zeta$  is blended by Galactic N I  $\lambda 1134.3$ ), as well as in C III, O III, Si III, O IV, and O VI (Fig. 16; note that H I Ly  $\iota$  has not been included in the plot). Absorption by N IV  $\lambda 765.1$  is possibly also detected. However, N V  $\lambda \lambda 1238.8, 1242.8$  and Si IV  $\lambda \lambda 1393.8, 1402.8$  are not detected with relatively large upper limits to their rest-frame equivalent widths that do not provide any useful information. The strong Ly  $\alpha$  line has a  $-50$  to  $-100$   $\text{km s}^{-1}$  wing, suggesting another absorption component at negative velocities. This feature is too weak to be present in any other of the lines from the H I Lyman series. The left wing of H I Ly  $\beta$  is blended by Galactic S II absorption. The H I column density of the main component (at  $0$   $\text{km s}^{-1}$ ) is  $\log N(\text{H I}) = 15.25 \pm 0.06$  (COG method; see Table 3 for details on the individual methods), thus being the second strongest IGM absorber towards PG 1259+593. From a Voigt profile fit of the Ly  $\beta$  line we obtain  $b = 32.3 \pm 1.4$   $\text{km s}^{-1}$ , implying  $T \leq 6.3 \times 10^4$  K. The logarithmic column densities of C III (ionization potential is  $\sim 48$  eV) and O III (ionization potential is  $\sim 55$  eV) are  $13.62 \pm 0.13$  (Voigt profile fit) and  $13.82 \pm 0.06$  (AOD method), respectively. For O IV we derive a column density of  $\log N(\text{O IV}) = 14.27 \pm 0.05$  (AOD method). Unresolved saturations may affect the C III and O IV absorption, so that the true values of  $N(\text{C III})$  and  $N(\text{O IV})$  could be somewhat larger than those listed. The Si III absorption at  $z = 0.21949$  is weak and relatively narrow. From a profile fit we obtain  $\log N(\text{Si III}) = 12.04 \pm 0.07$  and  $b = 7.9 \pm 2.0$   $\text{km s}^{-1}$  (see Table 3). N IV absorption is marginally detected at a  $1.9\sigma$  level near  $933$  Å, thus in a region where the FUSE spectrum is relatively noisy. We derive a  $3\sigma$  upper limit for the N IV column density of  $\log N(\text{N IV}) \leq 13.35$ . While the absorption of the intermediate ions (C III, O III, Si III, O IV, and N IV) is like H I centered at zero velocities, the O VI shows a very different absorption pattern. Two O VI absorption components are visible in the stronger O VI  $\lambda 1031.9$  line near  $0$  and  $-50$   $\text{km s}^{-1}$ . The negative velocity component possibly relates to the negative velocity wing seen in the Ly  $\alpha$  absorption. The weaker O VI  $\lambda 1037.6$  line is consistent with this two-component structure. The double-component O VI absorption is very symmetric, the entire structure having a center velocity near  $-25$   $\text{km s}^{-1}$ . It could possibly be related to an expanding shell or a symmetric outflow. A two-component Voigt profile fit yields identical column densities for both components ( $\log N(\text{O VI}) = 13.68 \pm 0.06$ ), and very similar  $b$  values ( $16.2 \pm 2.4$  and  $15.5 \pm 1.5$   $\text{km s}^{-1}$ ; see also Table 3). The total O VI column density is  $\log N(\text{O VI}) \approx 14.0$ . For pure thermal broadening, the individual  $b$  values correspond to temperatures of  $T \approx 2.5 \times 10^5$  and  $2.3 \times 10^5$  K, respectively, thus very close to the peak temperature for O VI in collisional ionization equilibrium ( $2.8 \times 10^5$  K; Sutherland & Dopita 1993).

With the simultaneous occurrence of O III, O IV, and O VI it is of interest to see if the main absorption component in this system can be modeled by assuming the gas is in photoionization

equilibrium with the background UV ionizing radiation. For the modeling we use the ionization equilibrium code CLOUDY (v94.00; Ferland 1996) to compute column densities of various ions through a slab illuminated with the Haardt & Madau (1996) UV radiation background from QSOs and AGNs appropriate for a redshift of  $\sim 0.2$ . The calculation assumes solar relative abundances from Anders & Grevesse (1989) for all elements except oxygen and carbon for which we adopt the new results from Allende Prieto, Lambert & Asplund (2001, 2002). Grain heating or cooling are ignored and the H I column density in the slab is taken to be  $\log N(\text{H I}) = 15.25$ . Since the column density of O IV is rather uncertain, we concentrate on the implications of  $\log N(\text{O III}) = 13.82 \pm 0.06$  and  $\log N(\text{O VI}) = 13.68 \pm 0.06$  in the component near  $0 \text{ km s}^{-1}$ . These O III and O VI column densities suggest an ionization parameter of  $\log U = -1.5$  where  $U = n_\gamma/n_{\text{H}}$  is the ratio of ionizing photon density to gas density. The resulting oxygen abundance is  $\log (\text{O}/\text{H}) - \log (\text{O}/\text{H})_\odot = [\text{O}/\text{H}] = -1.25 \pm 0.10$ . The model predicts  $\sim 0.2$  dex more O IV than is estimated from the probably saturated O IV line. For  $\log U = -1.5$ , the expected amount of Si III assuming a solar O to Si abundance ratio is 1.0 dex less than the observed value of  $\log N(\text{Si III}) = 12.04 \pm 0.07$ . This unrealistic abundance result suggests the absorption component near  $0 \text{ km s}^{-1}$  either is not Si III absorption at  $z = 0.21949$  (but another unidentified IGM line), or, more likely, it is Si III at  $z = 0.21949$  but tracing a multiphase mixture of absorbing structures. Disentangling the different contributions to each ion from each phase can not be reliably done with these relatively low S/N spectra which contain both weak absorption lines (O III, O VI, and Si III) and very strong lines (C III, O IV), which are probably saturated. Because of the difficulties introduced by the probable multiphase nature of the main absorption component, the abundance for oxygen and the value of  $\log U$  estimated above are not likely to be correct.

More can be learned about the O VI component near  $-50 \text{ km s}^{-1}$  with  $\log N(\text{O VI}) = 13.68 \pm 0.06$  since O IV is only marginally detected at that velocity and O III and C III are not detected. Integrating between  $-90$  and  $-35 \text{ km s}^{-1}$  we find that the weak O IV feature near  $-50 \text{ km s}^{-1}$  has  $W_r \approx 13 \text{ mÅ}$  ( $1\sigma$  evidence) which corresponds to  $\log N(\text{O IV}) \approx 13.43$ . If the O VI and the marginally detected O IV are produced by photoionization, the required value of the ionization parameter is  $\log U \approx -0.9$ . The hydrogen absorption possibly associated with this highly ionized absorber near  $-50 \text{ km s}^{-1}$  is visible as the broad negative velocity wing in the Ly  $\alpha$  profile. If we add an H I component with  $-50 \text{ km s}^{-1}$  to the principal H I absorption near zero velocities and fit the wing of the Ly  $\alpha$  profile, we obtain  $\log N(\text{H I}) \approx 13.5$  and  $b \approx 40 \text{ km s}^{-1}$  for the  $-50 \text{ km s}^{-1}$  component. This very uncertain value of  $b$  implies  $T \sim 10^5 \text{ K}$  if the broad feature is thermally broadened. Given the uncertainties, the line breadth is large enough to provide support to the collisional ionization explanation for the origin of O IV and O VI.

Observations of C IV (unfortunately located redwards of the wavelength range of the currently available STIS data) would be very useful to disentangle the ionization conditions in this interesting absorber in more detail. No Ne VIII  $\lambda 770.4$  is detected in the  $z = 0.21949$  absorber at a limiting logarithmic column density level of  $\log N(\text{Ne VIII}) \leq 13.94$  ( $3\sigma$ ). In collisional ionization equilibrium O VI and Ne VIII peak in abundance at  $2.8 \times 10^5 \text{ K}$  and  $7.0 \times 10^5 \text{ K}$ , respectively (Sutherland & Dopita

1993). Comparing the amount of O VI and Ne VIII therefore can provide temperature constraints. In our ionization discussions we will assume a solar abundance ratio for O/Ne and have taken the solar O and Ne abundances from Allende Prieto, Lambert & Asplund (2001) and Anders & Grevesse (1989), respectively. Relating the limit for Ne VIII to the total O VI column density in both components implies  $N(\text{O VI})/N(\text{Ne VIII}) \geq 0.1$  and  $T \leq 5.6 \times 10^5$  K, if the gas is in collisional ionization equilibrium.

### 3.2.5. The System at $z = 0.22313$

This system is detected in H I Ly  $\alpha$  and Ly  $\beta$ , and possibly in O VI  $\lambda 1037.6$  (Fig. 17). O VI  $\lambda 1031.9$  may also be present, but it lies in the vicinity of other strong IGM lines (e.g., Si III  $z = 0.04606$  and C III  $z = 0.29236$ , see also Fig. 7), which partly overlap the O VI absorption (Fig. 17). The H I Ly  $\alpha$  absorption is well fitted by a single-component absorber with  $\log N(\text{H I}) = 13.92 \pm 0.03$  and  $b = 34.8 \pm 1.1 \text{ km s}^{-1}$  (Voigt-profile fitting). Within the error range, the AOD method and COG fitting of the two Lyman lines result in very similar column densities (see Table 3). The O VI column density is  $\log N = 13.99 \pm 0.11$ , derived from O VI  $\lambda 1037.6$  via the AOD method. For pure thermal broadening, the  $b$  value from the H I profile fit yields  $T \leq 7.3 \times 10^4$  K. The O VI  $\lambda 1037.6$  line appears to be quite broad, ranging from approximately  $-90$  to  $+60 \text{ km s}^{-1}$  (Ly  $\alpha$ : approximately  $-60$  to  $+60 \text{ km s}^{-1}$ ). However, the O VI absorption is weak, so that the determined O VI velocity range is very sensitive to the continuum placement. Thus, the O VI line width is too uncertain to draw meaningful conclusions about the physical properties of the absorber. In view of the relatively low  $b$  value of the H I absorption it is plausible that H I absorption and O VI absorption occur in physically distinct regions. Although the O VI  $\lambda 1037.6$  absorption has a formal significance of  $\sim 4\sigma$ , we cannot completely exclude that this broad absorption feature is caused by a small-scale undulation in the continuum flux. Further it is possible that this feature is caused by a broad Ly  $\alpha$  absorption at  $z = 0.04417$  rather than being O VI at  $z = 0.22313$ . For these reasons, we can claim only a tentative detection of O VI absorption in this system.

There is a  $1.4\sigma$  absorption feature present precisely at the wavelength where Ne VIII  $\lambda 770.4$  at  $z = 0.22313$  would be expected (see lower-most right panel in Fig. 17). Due to the low significance, however, we cannot judge whether this feature is real or not. We derive a  $3\sigma$  upper limit of  $\log N(\text{Ne VIII}) \leq 13.75$ . The observed limit for the absorber at  $z = 0.22313$  of  $N(\text{O VI})/N(\text{Ne VIII}) > 1.7$  implies  $T < 5 \times 10^5$  K for the O VI absorber if the ionization is caused by electron collisions in gas close to collisional ionization equilibrium with a solar ratio of oxygen to neon.

### 3.2.6. The System at $z = 0.25971$

This system is seen in H I Ly  $\alpha$  and Ly  $\beta$ , O VI  $\lambda\lambda 1031.9, 1037.6$ , and possibly in Ne VIII  $\lambda 770.4$  (Fig. 18). Although the H I column density is relatively small ( $\log N(\text{H I}) = 13.84 \pm 0.12$  from profile

fitting; see Table 3 for details), the Ly  $\alpha$  absorption is quite broad, ranging approximately from  $-60$  to  $+60$  km s $^{-1}$  (see Fig. 18) and looks flat bottomed suggesting two blended H I absorption components of nearly equal strength. Also the O VI  $\lambda 1031.9$  absorption shows weak evidence for such a double-component structure. However, the S/N is formally not high enough to convincingly claim the existence of two (ore more) individual absorption components and we thus will adopt a single absorption component in the following. The one-component profile fit of the Ly  $\alpha$  line yields  $b = 40.5 \pm 4.9$  km s $^{-1}$ , equivalent to  $T \leq 10^5$  K <sup>2</sup>. No intermediate ions such as C III and O III are detected. The O VI absorption ( $\log N(\text{O VI}) = 13.84 \pm 0.07$ ; AOD; see Table 2) seems to span a velocity range roughly similar to that of the H I. A reliable estimate of the O VI line width by way of profile fitting, however, is not possible because the O VI absorption is relatively weak and the continuum in the vicinity of the O VI absorption appears to have some small-scale undulations (see Fig. 18)

There is a possible detection of Ne VIII  $\lambda 770.4$  in this system (see lower-most right panel in Fig. 18) at a  $1.9\sigma$  level. More data would be required to investigate whether this absorption feature is real. At this point, we only can place an upper limit of  $\log N(\text{Ne VIII}) \leq 13.96$ . The  $3\sigma$  limit on  $N(\text{O VI})/N(\text{Ne VIII}) > 0.76$  implies  $T < 6 \times 10^5$  K for gas in collisional ionization equilibrium with solar O and Ne abundance ratios. If instead we assume the possible Ne VIII feature observed with a  $1.9\sigma$  significance is real, the derived value of  $\log N(\text{Ne VIII})$  is  $\sim 13.8$  which is similar to the value for O VI. These two species will have the same abundance in a hot collisionally ionized plasma with solar abundance ratios if  $T$  is near  $5.6 \times 10^5$  K. However, this is inconsistent with the value of  $T \leq 10^5$  K estimated from the H I line assuming the H I line breadth is from pure thermal Doppler broadening. If Ne VIII actually is detected, the value of  $N(\text{O VI})/N(\text{Ne VIII})$  would suggest that the gas is not in collisional ionization equilibrium or the bulk of the H I absorption is formed in a cooler gas phase.

### 3.2.7. The System at $z = 0.29236$

Three H I Lyman lines (Ly  $\alpha$ , Ly  $\beta$ , and Ly  $\gamma$ ) are detected in this relatively strong system together with metal absorption from C III, O III, and O IV (Fig. 19). O VI and Ne VIII are not detected. The Ly  $\alpha$  line shows a very weak second absorption component near  $-80$  km s $^{-1}$ . The main component has an H I column density of  $\log N(\text{H I}) = 14.47 \pm 0.05$ , and the H I  $b$  value is  $26.2 \pm 1.6$  km s $^{-1}$ , as derived from a profile fit of the Ly  $\beta$  line (see Table 3). This  $b$  value corresponds to a temperature of  $\leq 4.1 \times 10^4$  K. Unfortunately, the C III line in the STIS part of the spectrum is partly blended by other IGM lines (see Figs. 7 & 19), so that it is difficult to reliably determine its behaviour at negative velocities. For the intermediate ions C III, O III, and O IV we derive logarithmic column densities of  $13.18 \pm 0.07$ ,  $13.80 \pm 0.06$  and  $14.16 \pm 0.04$  (AOD method) for the main component, respectively. The value for C III is very uncertain because of the

---

<sup>2</sup>Note that the temperature is much smaller if the absorber has two or more sub-components.

blending problems. In contrast, the measurements for H I , O III, and O IV appear quite reliable. The relatively low  $b$  value, the presence of various intermediate ion lines, as well as the lack of any high ions indicate that this system consists mainly of cooler gas with temperatures  $T \leq 4.1 \times 10^4$  K. If the gas in this system is in photoionization equilibrium, we can use the well determined values of  $N(\text{O III})$  and  $N(\text{O IV})$  to reliably estimate the ionization parameter and thereby obtain an estimate of the oxygen abundance in this low redshift system. For the system at  $z = 0.29236$  we use the Haardt & Madau (1996) UV radiation field for  $z = 0.3$  and take the H I column density in the slab to be  $\log N(\text{H I}) = 14.5$ . The column densities  $\log N(\text{O III}) = 13.80 \pm 0.06$  and  $\log N(\text{O IV}) = 14.16 \pm 0.04$  imply  $\log [N(\text{O III})/N(\text{O IV})] = -0.36 \pm 0.07$  which constrains the value of the ionization parameter  $\log U$  to be  $-1.68 \pm 0.10$ . With this value of  $\log U$ , the model yields the observed O III and O IV column densities for  $[\text{O}/\text{H}] = -0.5 \pm 0.1$ . These numbers decrease to  $[\text{O}/\text{H}] = -0.74 \pm 0.1$  if we instead use the older solar abundance from Anders & Grevesse (1989). Using the uncertain C III column density of  $\log N(\text{C III}) = 13.18 \pm 0.07$ , where the error does not adequately account for the uncertainty in the line blending correction, we obtain  $[\text{C}/\text{H}] = -1.0 \pm 0.1$ , implying  $[\text{C}/\text{O}] = -0.5 \pm 0.1$  in this absorption system. The listed errors do not allow for possible systematic errors associated with the photoionization modeling assumptions such as the geometry of the absorber and the shape of the ionizing background. Subsolar values of C/O are commonly found in low metallicity dwarf galaxies (Garnett et al. 1995) and the data point for this QSO absorption system fits on the observed trend of  $\log (\text{C}/\text{O})$  versus  $\log (\text{O}/\text{H})$  shown in Figure 3 of Garnett et al. (1995) after adjustment to the same reference abundances. In view of the substantial uncertainty in the C III measurement we will not discuss the various nucleosynthetic explanations for such a behavior (see Garnett et al. 1995). However, our measurements for this system illustrate the potential of UV and far-UV observations for providing interesting information on the nucleosynthetic history of the gas in QSO systems at low redshift. Although blending has created problems in this one case for C III, the blending problem is much less severe at low redshift than in the Ly  $\alpha$  forest at high redshift. The large ionization parameter  $\log U = -1.68$  required to fit the observations implies the gas density in the system is low with a total ( $\text{H}^+ + \text{H}^0$ ) hydrogen density  $n_{\text{H}} = 1.8 \times 10^{-5} \text{ cm}^{-3}$ . At this density, the absorber must have a thickness of 34 kpc in order to achieve the total O III and O IV column densities observed.

### 3.2.8. The System at $z = 0.31978$

This system is detected solely in H I (Ly  $\alpha$  and Ly  $\beta$ ) and possibly O VI ( $\lambda 1031.9$ ; see Fig. 19). The Ly  $\alpha$  absorption is very broad, spanning from approximately  $-150$  to  $+100 \text{ km s}^{-1}$ , while the candidate O VI  $\lambda 1031.9$  line is quite narrow and well defined. The weaker O VI  $\lambda 1037.6$  line is heavily blended by interstellar Ni II  $\lambda 1370.1$  absorption in the Complex C component near  $+20 \text{ km s}^{-1}$  (in the  $z = 0.31978$  restframe), and possibly also by a broad, weak Ly  $\alpha$  absorbers near  $-100 \text{ km s}^{-1}$ . However, a multi-component fit of the entire area including Ni II and a broad Ly  $\alpha$  component indicates that there is enough absorption to fit O VI  $\lambda 1037.6$  into this pattern at the strength that would be expected from the stronger O VI  $\lambda 1031.9$  line.

Single-component Voigt profile fits to the Ly  $\alpha$  and O VI  $\lambda 1031.9$  lines yield redshifts of  $0.319775 \pm 0.000029$  and  $0.319731 \pm 0.000009$ , respectively. The redshift difference of  $0.000044 \pm 0.000030$  corresponds to a velocity difference of  $\Delta v = 10.0 \pm 7.0 \text{ km s}^{-1}$  in the restframe of the system. Although the data suggest a small velocity shift for the O VI absorption compared to H I, the size of the shift is only  $1.4\sigma$ . In addition, evidence of relative wavelength calibration errors as large as  $\sim 1$  pixel have been found in some STIS E140M spectra (Tripp et al. 2004, in preparation). Although wavelength calibration errors this large are quite rare in E140M spectra (Leitherer et al. 2002), it is possible that the O VI–H I offset could be a calibration artifact. Because of substantial continuum placement uncertainty, the Ly  $\beta$  measurement has a redshift uncertainty  $\sim 3$  times larger than for Ly  $\alpha$ . Therefore, Ly  $\beta$  is not helpful in establishing if the apparent small velocity shift between H I and O VI is real. There is a suggestion of a two component structure to the H I Ly  $\alpha$  absorption with a weak second component appearing near  $-120 \text{ km s}^{-1}$  in the  $z = 0.31978$  rest frame. However, the appearance of the feature is very strongly influenced by the adopted position of the uncertain continuum on the blue wing of the Ly  $\alpha$  line. Because of the uncertain continuum, we cannot claim this possible second component is real. The one component Voigt profile fits to the Ly  $\alpha$  and O VI  $\lambda 1031.9$  lines yield  $b(\text{H I}) = 74.4 \pm 8.7 \text{ km s}^{-1}$ ,  $b(\text{O VI}) = 19.3 \pm 4.2 \text{ km s}^{-1}$ , and  $\log N(\text{H I}) = 13.98 \pm 0.06$ . The ratio of these  $b$  values is  $3.85 \pm 0.97$  which is consistent with the expected ratio of 4 if these two species existed in the same hot gas with the line broadening dominated by thermal Doppler broadening. Assuming pure thermal Doppler broadening  $b(\text{H I})$  implies  $T = (3.3^{+0.8}_{-0.7}) \times 10^5 \text{ K}$  while  $b(\text{O VI})$  implies  $T = (3.6^{+1.7}_{-1.4}) \times 10^5 \text{ K}$ . Both values of  $T$  are close to the temperature of  $2.8 \times 10^5 \text{ K}$  where O VI peaks in abundance if collisional ionization equilibrium prevails. An upper limit for the temperature in the absorber can be determined from the absence of Ne VIII in the system. A quite stringent column density limit of  $\log N(\text{Ne VIII}) \leq 13.57$  can be placed due to the good S/N in the FUSE range where Ne VIII absorption would be expected to occur (near  $1017 \text{ \AA}$ , see Table 3 and Figure 19). With  $\log N(\text{O VI}) = 13.44 \pm 0.06$  from the AOD method we obtain  $N(\text{O VI})/N(\text{Ne VIII}) \geq 0.74$  for the absorber. If the gas in the system has a solar O to Ne abundance ratio and has a physical state close to collisional ionization equilibrium, this ionic ratio implies  $T \leq 6 \times 10^5 \text{ K}$  based on the collisional ionization equilibrium calculations of Sutherland & Dopita (1993). A similar approach can be used to determine a lower limit to  $T$  from the absence of O IV  $\lambda 787.7$  absorption with a  $3\sigma$  limit for  $\log N(\text{O IV}) \leq 13.30$  (see Table 3). With  $N(\text{O IV})/N(\text{O VI}) \leq 0.73$  the lower limit on  $T$  is  $2 \times 10^5 \text{ K}$ .

Due to its simplicity and its suggested high-temperature characteristics, this system represents an interesting case for a more detailed modelling of the physical conditions. The large H I  $b$  value and the presence of O VI already suggest that this absorption system consists mainly of hot gas at temperatures around  $3 \times 10^5 \text{ K}$ . However, due to the fact that the O VI  $\lambda 1037.6$  absorption is completely blended, we cannot exclude that the line that we had identified as O VI  $\lambda 1031.9$  at  $z = 0.31978$  is not O VI but just another weak (and narrow) Ly  $\alpha$  absorber or another unknown IGM line. From a conservative point of view, we therefore have to regard this system as a tentative intervening O VI absorber. If the relatively narrow line we identify as O VI really is O VI, the measurements imply that the broad profiles of Ly  $\alpha$  and Ly  $\beta$  probably are dominated by thermal

Doppler broadening at  $T \sim 3 \times 10^5$  K since the narrow O VI line, the broad Lyman lines, as well as the limits for Ne VIII and O IV yield nearly the same gas temperature. With the assumption that this absorbing gas is in collisional ionization equilibrium we can draw several additional interesting conclusions. The ionization fraction  $N(\text{H I})/N(\text{H}_{\text{total}})$  at  $T = 3 \times 10^5$  K is  $1.5 \times 10^{-6}$  (Sutherland & Dopita 1993). With  $\log N(\text{H I}) = 13.98 \pm 0.06$  this implies  $N(\text{H}_{\text{total}}) = 6.4 \times 10^{19} \text{ cm}^{-2}$ . Similarly,  $N(\text{O VI})/N(\text{O}_{\text{total}}) = 0.20$  at  $T = 3 \times 10^5$  K and therefore  $N(\text{O}_{\text{total}}) = 1.4 \times 10^{14} \text{ cm}^{-2}$  and  $N(\text{O}_{\text{total}})/N(\text{H}_{\text{total}}) = 2.1 \times 10^{-6}$ . With a solar value of  $(\text{O}/\text{H}) = 4.9 \times 10^{-4}$  (Allende Prieto, Lambert & Asplund 2001), these total column density estimates imply that the O abundance in this O VI system is  $\sim 4.3 \times 10^{-3}$  solar. The result is very sensitive to the adopted value of  $T$ . For example, for  $T = 2 \times 10^5$  or  $T = 4 \times 10^5$  K, the inferred oxygen abundance increases to  $8.9 \times 10^{-3}$  and  $7.7 \times 10^{-3}$  times solar, respectively. The derived metallicity for this absorber could change substantially if the H I and O VI component structure is more complex than we have assumed in our analysis.

While the estimates depend on the validity of the assumption of collisional ionization equilibrium in the absorbing gas, it is noteworthy that low density hot plasmas with such low abundances actually cool rather slowly since the principal heavy element coolants (C, N, and O) have low abundance. An abundance as low as  $\sim 4 \times 10^{-3}$  solar, if correct, has important implications since the estimated baryonic content of the O VI systems scales inversely with the assumed oxygen abundance. Savage et al. (2002) estimated that the gas in low redshift O VI systems contribute  $\sim 0.002$  to the cosmological closure density assuming the average oxygen abundance in O VI systems is 0.1 solar. This contribution is comparable to that found in galaxies but  $\sim 20$  times smaller than the total contribution for baryons estimated from the Cosmic Background radiation or from big bang nucleosynthesis. However, if the typical oxygen abundances in the O VI systems are 10 to 25 times smaller, the estimate for the baryonic content of these systems would increase by factors of 10 to 25.

### 3.3. O VI Absorbers

The analysis of the metal-line systems towards PG 1259+593 reveals the presence of at least three intervening O VI systems that are clearly detected in either one ( $z = 0.04606$ ) or both O VI lines ( $z = 0.21949$  and  $z = 0.25971$ ). We tentatively detect O VI in four additional systems ( $z = 0.00229, 0.00760, 0.22313, 0.31978$ ), but for these systems the data do not allow us to claim a firm detection. Therefore, we assume the number of intervening O VI absorbers towards PG 1259+593 to be 3 – 7 in total. Six of these lines have  $W_r \geq 25 \text{ m}\text{\AA}$ , the seventh has  $W_r = 15 \text{ m}\text{\AA}$ .

The available wavelength range for intervening O VI absorption towards PG 1259+593 is from  $\sim 1032$  to  $\sim 1495 \text{ \AA}$ . The latter wavelength separates intervening O VI absorption with radial velocities  $> 6000 \text{ km s}^{-1}$  away from the quasar from systems possibly associated with the QSO (“associated systems”). The wavelength range corresponds to a O VI redshift path of  $\Delta z \approx 0.449$ . In this regime, the S/N is roughly constant, and we estimate the typical lower equivalent width



limit to detect intervening O VI absorption to be  $W_r = 24 \text{ m}\text{\AA}$  ( $3\sigma$  restframe equivalent width limit). However, the many intergalactic and interstellar absorption lines in this wavelength range obscure a significant portion of this redshift path, so we have to correct  $\Delta z$  for this blocking effect. Integrating the blocking for each individual line between 1032 and 1495  $\text{\AA}$ , we find a total blocking of  $\Delta z_B = 0.085$ , so that the total unobscured redshift path for O VI absorption is  $\Delta z = 0.364$ . In this study we assume the presence of the stronger of the two O VI absorption lines to be sufficient to claim at least a tentative detection of an intervening O VI system, so that the blocking correction does not have to be applied twice. Thus, the number of intervening O VI systems with  $W_r \geq 24 \text{ m}\text{\AA}$  ( $3\sigma$ ) per unit redshift towards PG 1259+593 is  $dN_{\text{OVI}}/dz = 8 - 16$ <sup>3</sup>. At this sensitivity limit, this value is consistent with previous studies (e.g., Savage et al. 2002).

It is often difficult to determine if O VI systems are collisionally ionized or photoionized (e.g., Tripp et al. 2001, 2002). Consequently, it is valuable to compare the observed statistics of these O VI lines to the predicted statistics from theoretical work in order to test whether the O VI absorbers are generally consistent with the expected properties of the low-redshift WHIM. The number of intervening O VI absorbers per unit redshift is one of the most readily measured statistics, both in the theoretical models and the real observations. We find that the O VI  $dN/dz$  values that we observe toward PG1259+593 and other sight lines (Savage et al. 2002) are in agreement with the predictions of hydrodynamic simulations of cosmological structure growth (Cen et al. 2001; Fang & Bryan 2001; Chen et al. 2003), but only if the mean metallicity of the IGM is not too high. Chen et al. (2003) show that if the metallicity of the IGM were elevated to solar metallicity, for example, then their predicted  $dN/dz$  for O VI absorbers would be significantly higher than our observed values. However, with  $Z \sim 0.1 Z_\odot$ , the observed  $dN/dz$  is close to the predicted value from Chen et al. model. Since the baryonic content of the O VI systems is inversely proportional to the metallicity of the gas, the conclusion that  $Z < Z_\odot$  in O VI absorbers bolsters the finding that these systems contain a substantial fraction of the baryons at the present epoch. The observations also indicate that at least some O VI absorbers arise in photoionized gas, and this is predicted by the hydrodynamic models as well. At this juncture, the simulations and observations appear to be in good agreement with regard to the O VI absorber statistics.

### 3.4. The Ly $\alpha$ /Ly $\beta$ Forest

Of the systems that are detected solely in H I, 14 show absorption by at least two lines of the H I Lyman series, including one system ( $z = 0.43569$ ) for which the Ly  $\alpha$  absorption has been identified in the FOS spectrum of PG 1259+593 (Bahcall et al. 1993). Redshifts, H I column densities, and  $b$  values are listed in Table 3. Velocity plots are presented in Figs. 13, 15, 17, 18, 20 and 21. 50 systems are seen only in one single line, which we assume to be Ly  $\alpha$  (see discussion in §3.1).

---

<sup>3</sup>Note that at this equivalent width limit the weak tentative detection of O VI at  $z = 0.00760$  ( $W_r \approx 15 \text{ m}\text{\AA}$ ) is not included in our estimate for  $dN_{\text{OVI}}/dz$ .

Redshifts, column densities and  $b$  values for these systems (as derived by using Voigt-profile fitting) are given in Table 5. We have given every Ly  $\alpha$  line listed in Table 5 a “reliability flag” (Table 5, seventh column) to indicate the reliability of the listed line parameters (equivalent width, column density, Doppler parameter) for each line (see §2.3 for details). Including the eight metal-line systems discussed in the previous section, the line of sight towards PG 1259+593 consists of 72 intervening intergalactic absorption line systems (78 absorption components), for which a short statistical analysis is presented in the following sections.

### 3.4.1. $dN/dz$ for Ly $\alpha$ Absorbers

The wavelength range for possible intergalactic Ly  $\alpha$  absorption is  $\sim 511 \text{ \AA}$  ( $\sim 1218 - 1729 \text{ \AA}$ , corresponding to  $\Delta z \approx 0.420$ ), and there are 77 Ly  $\alpha$  lines detected in this range. It is misleading, however, to derive the number of Ly  $\alpha$  absorbers per unit redshift,  $dN_{\text{Ly}\alpha}/dz$ , for this redshift range given the fact that the S/N in the STIS data decreases significantly toward higher wavelengths, and some of the Ly  $\alpha$  identifications thus are doubtful. A roughly constant S/N of  $\sim 12$  per resolution element is provided for the range between 1218 and 1525  $\text{\AA}$  ( $\Delta z \approx 0.253$ ). In this range, 47 Ly  $\alpha$  lines are seen above an limiting rest-frame equivalent width of  $W_\lambda \geq 30 \text{ m\AA}$ . For this sensitivity limit, we find  $dN_{\text{Ly}\alpha}/dz = 190 \pm 28$  for the sight line towards PG 1259+593, after applying a blocking correction of  $\Delta z_B \approx 0.006$  for strong ISM lines to the above redshift path. This value is consistent with the low-redshift  $dN_{\text{Ly}\alpha}/dz$  distribution presented by Penton, Shull & Stocke (2000; their Fig. 8) for their GHRS sample of 15 extragalactic targets. Recent studies (e.g., Janknecht, Baade & Reimers 2002; Kim et al. 2002) suggest that a break in redshift evolution of the Ly  $\alpha$  forest (characterized by the power law  $dN/dz = (1+z)^\gamma$ ) appears at  $z \approx 1$ . For high-column density systems with  $13.65 \leq \log N \leq 16.00$  there is an abrupt change in  $\gamma$  from  $\sim 2.4$  for  $z > 1$  to  $\sim 0$  for  $z \leq 1$ . This break is less evident for weaker systems with  $13.10 \leq \log N \leq 14.00$ , where the evolution at higher redshift is slower ( $\gamma \sim 1.4$  for  $z > 1$ ; Janknecht, Baade & Reimers 2002). The redshift evolution of the Ly  $\alpha$  forest density usually is attributed to the combined (counteracting) effects of a decreasing ionizing background flux together with a decreasing gas density due to expansion of the Universe. Our data yields  $\log dN/dz \sim 2.0$  for Ly  $\alpha$  absorbers with  $13.6 \leq \log N \leq 16.0$  and  $\log dN/dz \sim 1.7$  for systems with  $13.1 \leq \log N \leq 14.0$  in our selected redshift range  $z \leq 0.25$ , thus consistent with the previous low redshift data (Weymann et al. 1998; Penton, Shull & Stocke 2000).

Interestingly, there is no absorber directly associated with the quasar PG 1259+593 itself. While the Ly  $\alpha$  line at or near  $z = 0.478$  lies outside the STIS range studied here, intrinsic Ly  $\beta$  absorption would be expected near 1516  $\text{\AA}$ , but no absorption is seen around this wavelength (see Fig. 10). The closest IGM line bluewards is at 1508.963, which we identify as Ly  $\alpha$   $z = 0.24126$  (see Table 5). If this line would be intrinsic Ly  $\beta$  rather than intervening Ly  $\alpha$ , it would already be more than  $1300 \text{ km s}^{-1}$  away from the quasar. Also the low-resolution FOS data of PG 1259+593 (Bahcall et al. 1993) show no evidence for a significant absorption line near 1797  $\text{\AA}$  where intrinsic Ly  $\alpha$  absorption would be expected. A broad Ly  $\alpha$  emission from the QSO itself, however, is clearly

seen at this wavelength (Bahcall et al. 1993).

### 3.4.2. *Distribution of $b$ Values and Column Densities*

Fig. 22, upper left panel, shows the number distribution of  $b$  values for the absorbers (and their sub-components), given in  $10 \text{ km s}^{-1}$  wide bins. The distribution plotted with the thin line represents the number distribution of all absorption components for which  $b$  values have been measured; the distribution plotted with the thick line shows the number distribution of  $b$  values excluding the cases that are flagged as “uncertain” (UC; see Tables 3, 5 and §2.3). The distribution of  $b$  values peaks around  $25 \text{ km s}^{-1}$ , very similar to what is found in the larger HST sample presented by Penton, Shull & Stocke (2000). The distribution shows a wing towards higher  $b$  values. This wing extends to  $100 \text{ km s}^{-1}$  in the distribution of the more reliable  $b$  values (thick line), and to  $210 \text{ km s}^{-1}$  for the total sample (thin line). Most of the high  $b$  values with  $100 \leq b \leq 210 \text{ km s}^{-1}$  most likely are caused by unresolved sub-component structure in lines, continuum undulations, and other effects that may produce broad spectral features. Thus, part of the wing feature in the  $b$  value distribution certainly is artificial in nature (see also discussion in Penton, Shull & Stocke, 2000). However, there are seven lines with  $b \geq 50 \text{ km s}^{-1}$  that do not show evidence that such effects are responsible for the large breadth of the line. These lines thus may represent intrinsically broad Ly  $\alpha$  absorbers; they will be discussed below. Examples for Voigt profiles fitted to broad Ly  $\alpha$  absorbers are presented in Figs. 23 and 24.

In the upper right panel of Fig. 22 we have plotted the distribution of column densities for the 78 absorption components, divided into bins of 0.4 for  $\log N(\text{H I})$ , starting at  $\log N(\text{H I}) = 12.6$ . Similar to the  $b$  value distribution, the thin line shows the distribution for  $\log N$  for the total sample, whereas the thick line shows the  $\log N$  distribution excluding the uncertain cases. This distribution has its maximum in the range between  $\log N(\text{H I}) = 13.0 - 13.8$ . Note that the determination of  $\log N(\text{H I})$  depends on the adopted  $b$  value for each individual system. At the same equivalent width, a lower  $b$  value would result in a higher column density. Therefore, the distribution of column densities and the distribution of  $b$  values are coupled by the curve-of-growth analysis (thus by the Voigt function). The observed distribution indicates a peak at column densities slightly higher than found in the sample by Penton, Shull & Stocke (2000), although the  $b$  value distribution is very similar.

In the lower panel of Fig. 22 we have plotted Doppler parameters versus logarithmic column densities. Systems for which  $b$  values and column densities can be reliably determined (status is ‘OK’) are shown as filled circles; systems for which the values of  $\log N$  and  $b$  are uncertain (status ‘UC’) are shown as open circles. Most of the data points with  $b < 60 \text{ km s}^{-1}$  follow the trend for a small increase of the  $b$  values with significantly increasing column densities. Such a trend is expected assuming that the higher column-density absorbers arise from clouds that have higher volume densities and higher temperatures (e.g., Davé & Tripp 2001). There appears to be, however, a second branch in this plot for  $b \geq 60 \text{ km s}^{-1}$ , indicating absorption systems that exhibit a strong

increase in  $b$  to very high Doppler parameters whereas the increase in  $N$  is only modest. Most of the uncertain, broad features lie on this branch (open circles), although there are a few systems with reliable values for  $\log N$  and  $b$  (filled circles). If this branch is not an artifact caused by line blending, continuum undulations and/or other effects, we may have found a new, independent class of low-column density H I absorbers with large to very large Doppler parameters. If thermal line broadening would be the dominating broadening mechanism for these systems, they may trace WHIM absorbers in the  $10^5$  to  $10^6$  K temperature range. Such WHIM absorbers naturally would have very low neutral gas fractions (Sutherland & Dopita 1993) and therefore low H I column densities. We consider the reliability and nature of these broad absorbers in the following section.

### 3.5. Broad Ly $\alpha$ Absorbers

From all Ly  $\alpha$  lines listed in Tables 3 and 5 we are particularly interested in those with  $b$  values exceeding  $40 \text{ km s}^{-1}$ , as they may sample intervening WHIM absorbers with temperatures above  $T \sim 10^5$  K. However, it is likely that next to thermal broadening other effects like line blends, unresolved sub-components, low S/N, kinematic flows, Hubble broadening and continuum undulations contribute to the population of broad absorbers along the line of sight towards PG 1259+593. For the single-line Ly  $\alpha$  absorbers listed in Table 5 we have analyzed in detail the shape and other properties of the absorbers in order to sort out those lines for which there is evidence that their width is caused not by thermal broadening but by something else. Some of the absorbers show typical signatures for unresolved sub-components, as indicated by asymmetric line shapes or positive/negative velocity wings. These cases have been marked accordingly in the last row of Table 5. Moreover, for many of the broader lines listed in Table 5 the estimate for  $b$  is very sensitive to the choice of the continuum level. This, together with the relatively low S/N for some of these lines, limits the credibility of the identification of broad lines with  $b$  values above  $40 \text{ km s}^{-1}$ , although the formal  $1\sigma$  errors derived from Voigt profile fitting (see Figs. 23, 24, and Table 5) may be only a few percent. From Tables 3 and 5 we find nine broad absorption systems detected solely in H I Ly  $\alpha$  (Table 5) and/or Ly  $\beta$  (Table 3) with  $b$  values larger than  $40 \text{ km s}^{-1}$  for which a) we can determine  $b$  with a reasonable accuracy (i.e., their status given in Table 5 is 'OK'), and b) which do not show any evidence for unresolved sub-structure or blending. These absorbers are listed in Table 6. Table 6 also lists the two O VI systems that have H I  $b$  values larger than  $40 \text{ km s}^{-1}$  and that do not show evidence for further sub-component structure (see §3.2). It is important to note at this point that the current STIS data are not accurate enough to *exclude* that line blending, sub-component structure, or continuum undulations contribute to the large widths of the absorbers given in Table 6. We can only claim that the current data *show no evidence* that these lines are affected by such processes. We thus regard these systems as possible candidates for thermally broadened WHIM absorbers with temperatures  $T \geq 10^5$  K. Despite the remaining uncertainty about their nature, we want to discuss their physical and statistical properties in the following to explore, what importance the possible existence of such systems has for our knowledge about the WHIM and its baryonic content. All of the candidates listed in Table 6 have  $40 \leq b \leq 100 \text{ km s}^{-1}$ , sampling a temperature

regime (for pure thermal broadening) of approximately  $1 \times 10^5$  to  $6 \times 10^5$  K. Thus, none of the really broad lines with  $b \geq 100 \text{ km s}^{-1}$  from Table 5 are considered to be sufficiently securely detected (see also Fig. 24, lower-most panel). This has to do mostly with the difficult continuum placement for the particularly broad and shallow features. As these broad absorbers (if real) may contain a large amount of the baryonic mass in the IGM, we will - nevertheless - discuss the importance of these lines for  $\Omega_b$  in the following. In principle, the broad Ly  $\alpha$  lines may sample WHIM absorbers a) that have total column densities too low for O VI being detectable, b) that have total column densities comparable to existing O VI systems but have very low oxygen abundances, or c) that have large total column densities but temperatures too high ( $T > 5 \times 10^5$  K) for O VI to be present unless the total hydrogen column density would be very large. The latter type of absorbers is particularly interesting, as such WHIM clouds would contain large amounts of baryonic matter and could be observed in X-ray O VII/O VIII absorption (“X-ray forest”; e.g., Rasmussen, Kahn & Paerels 2003; Fang et al. 2002). We expect the broad Ly  $\alpha$  absorbers to arise in shock-heated, highly-ionized gas clouds (e.g., Cen & Ostriker 1999), so the first step towards estimating their baryonic content is to determine their ionization fraction. In the following, we assume collisional ionization equilibrium (CIE) and use the models presented by Sutherland & Dopita (1993). For the cooler and denser clouds with  $T < 5 \times 10^5$  K the assumption of CIE may be somewhat problematic, as such gas may cool rapidly. However, the cooler absorbers also have the lowest baryon content, so their uncertainty contributes only little to the total uncertainty for deriving the overall baryonic content of the broad Ly  $\alpha$  lines. For the higher temperature Ly  $\alpha$  absorbers the assumption of CIE should be reasonably accurate. For the temperature regime between  $10^5$  and  $10^7$  K the ionization correction parameter calculated by Sutherland & Dopita (1993),  $\log f_H = -\log (H^0/(H^0+H^+)) \approx \log (H^+/H^0)$ , can be approximated by a simple polynomial:

$$\log f_H = \log f_H(T) \approx -13.9 + 5.4 \log T - 0.33 (\log T)^2. \quad (2)$$

From equation (1), it follows that  $\log T \approx \log(60 b^2)$  for hydrogen, which can be set into equation (2) to derive  $\log f_H$  for an individual absorber directly as a function of its  $b$  value (under the assumption that thermal broadening is the dominating broadening process). The cosmological mass density of the broad Ly  $\alpha$  absorbers,  $\Omega_b(\text{BL})$  (in units of the today’s critical density,  $\rho_c$ ), can be given as

$$\Omega_b(\text{BL}) = \frac{\mu m_H H_0}{\rho_c c \Delta X} \sum_i f_{H,i} N(\text{HI})_i \approx 1.667 \times 10^{-23} \Delta X^{-1} \sum_i f_{H,i} N(\text{HI})_i, \quad (3)$$

where  $\mu = 1.3$  corrects for the presence of helium,  $m_H = 1.673 \times 10^{-27} \text{ kg}$  is the proton mass,  $H_0 = 75 \text{ km s}^{-1} \text{ Mpc}^{-1}$  and  $\rho_c = 3H_0^2/8\pi G$ .  $\Delta X$  is the distance interval in which the broad Ly  $\alpha$  absorbers are located. The index  $i$  is running from 1 to  $n$ , where  $n$  is the number of broad Ly  $\alpha$  absorbers in the distance interval  $\Delta X$ . For a redshift range from  $z_{\min}$  to  $z_{\max}$  and with  $q_0 = 0$  we can write

$$\Delta X = 0.5 \{[(1 + z_{\max})^2] - [(1 + z_{\min})^2 - 1]\}. \quad (4)$$

However, a blocking correction has to be included for  $\Delta X$  to account for the regions in which possible broad Ly  $\alpha$  absorbers may remain unnoticed due to blending with other ISM or IGM lines. For PG 1259+593, the available redshift path to detect broad Ly  $\alpha$  absorbers is  $\Delta z = z_{\max} \approx 0.420$ . The total blocking from other intergalactic and interstellar lines for this redshift range sums up to  $\Delta z_B = 0.065$ , and we estimate  $\Delta X = 0.430$  from equation (4). If we take the eight candidates detected solely in H I Ly  $\alpha$  listed in Table 6 (ignoring the one broad Ly  $\beta$  system at  $z = 0.43569$  for which Ly  $\alpha$  lies outside the STIS wavelength range), we find a number of broad Ly  $\alpha$  absorbers per unit redshift of  $dN_{\text{BL}}/dz \approx 23$  toward PG 1259+593. Note that we do not consider the two additional O VI systems listed in Table 6 at this point, as they are treated separately to constrain  $dN_{\text{O VI}}/dz$  and the resulting  $\Omega_b(\text{O VI})$  (see also §3.3). For each of the eight Ly  $\alpha$  absorbers we can derive  $f_{\text{H,i}}$  from equation (2), as listed in Table 6 (seventh column). As we formally cannot exclude that processes other than thermal broadening contribute to the width of the lines given in Table 6, we conservatively list the values for  $f_{\text{H,i}}$  and  $T$  as upper limits. Together with the measured column densities,  $N(\text{H I})_i$ , we thus obtain  $\Omega_b(\text{BL}) \leq 0.0031 h_{75}^{-1}$ . This limit is higher than what is currently estimated for  $\Omega_b$  from gas residing in intervening O VI absorbers ( $\Omega_b(\text{O VI}) \geq 0.002 h_{75}^{-1}$  at  $\langle z \rangle = 0.09$  for O VI equivalent widths  $\geq 50 \text{ mÅ}$  and an average metallicity of 0.1 solar; see Savage et al. 2002). It is important to note that  $\Omega_b(\text{O VI})$  depends on the assumed metallicity, while  $\Omega_b(\text{BL})$  is determined independently of the metallicity. However, although we have very carefully selected our sub-sample of broad Ly  $\alpha$  lines, we are heavily biased against absorbers with large  $b$  values, which have the highest ionization correction and which thus contain most of the baryonic mass. All the absorbers listed in Table 6 have  $b$  values less than  $100 \text{ km s}^{-1}$ , because the shallow, broad absorbers with higher  $b$  values listed in Table 5 are most uncertain. However, if only one of the very broad features listed in Table 5 is a real thermally broadened H I absorber, the baryonic mass density derived from the presence of this *single* absorption system (if representative for the given redshift path) would be immense - it would have a larger baryonic content than the combined contributions of all nine systems not containing O VI listed in Table 6. For future observations it is therefore of crucial interest to investigate whether similar broad absorbers are seen also toward other low-redshift quasars, and to evaluate their frequency and physical properties.

### 3.6. Association with Known Galaxies/Galaxy-Clusters

#### 3.6.1. Overview

To further investigate the properties and nature of the detected metal line systems, it is of great interest to find possible connections between the absorption line systems and galaxies/galaxy-groups that are located in the general field of the background source PG 1259+593. We have searched the NED data archive (<http://nedwww.ipac.caltech.edu>) for a first inspection to find

nearby galaxies and galaxy-groups for which redshift data have been published. Moreover, Chen et al. (2001) provide information for two galaxies at  $z = 0.19620$  and  $z = 0.24120$  in the immediate vicinity of the PG 1259+593 sight line (angular separation  $< 2$  arcmin) based on HST WFPC2 data. Within a search radius of  $60''.0$  around the center position of PG 1259+593, NED finds 16 objects (14 galaxies and two galaxy groups) that have redshifts  $z \leq 0.478$ . We have listed these objects together with their coordinates and redshifts in Table 7. The most nearby absorbers found towards PG 1259+593 and their impact parameters,  $\rho_{75}$  (assuming  $H_0 = 75 \text{ km s}^{-1} \text{ Mpc}^{-1}$  and  $q_0 = 0$ ) are also listed (Table 7, columns seven and eight). Eight absorption systems have nearby galaxies with impact parameters  $\rho_{75} \leq 600$  kpc, three have  $\rho_{75} \leq 300$  kpc. For the future we are planning additional observations using the WIYN telescope to investigate in detail the relation between individual absorption-line systems and galaxies/galaxy-groups in the field of PG 1259+593.

### 3.6.2. UGC 08146

A very close match in redshift is found for the galaxy UGC 08146 ( $z = 0.00224$ ) and the absorption system at  $z = 0.00229$  (see §3.2.1), which shows H I absorption and possibly absorption by O VI. It thus appears plausible that the  $z = 0.00229$  absorption occurs in the halo or nearby intergalactic environment of UGC 08146. In Fig. 25 we show the sky positions of PG 1259+593 and UGC 08146 on an image taken from the *Digitized Sky Survey* (DSS). For UGC 08146 we have overlaid H I 21cm contours from data of the *Westerbork Synthesis Radio Telescope* (WSRT; from Rhee & von Albada 1996). Assuming  $H_0 = 75 \text{ km s}^{-1} \text{ Mpc}^{-1}$ , the redshift of  $z = 0.00224$  ( $v_r = 672 \text{ km s}^{-1}$ ) corresponds to a distance of  $\sim 9.0 h_{75}^{-1} \text{ Mpc}$ . Five arcmin in Fig. 25 therefore are equivalent to  $\sim 13$  kpc at the distance of UGC 08146. The angular separation between UGC 08146 and the line of sight to PG 1259+593 is  $\sim 21$  arcmin, so that the projected distance is only  $\sim 55 h_{75}^{-1} \text{ kpc}$ . If we take the small redshift difference of  $\Delta z = 5 \times 10^{-5}$  ( $\Delta v = 15 \text{ km s}^{-1}$ ) into account and assume a "pure" Hubble flow (see, e.g., Stocke et al. 1995), we derive a cloud-galaxy distance of  $\sim 207 h_{75}^{-1} \text{ kpc}$ . The sight line towards PG 1259+593 thus appears to pass through the immediate intergalactic environment of UGC 08146.

UGC 08146 is a dwarf spiral, classified as Sc(d) (e.g., Stil & Israel 2002). The optical diameter of UGC 08146 in the blue is  $\sim 9$  kpc (defined as  $25^{\text{th}}$  magnitude isophote, including an extinction correction), while the H I effective diameter (enclosing 50 percent of the H I mass) is 21 kpc or more than twice as large (Rhee & von Albada 1996). The undisturbed nature of the H I profile and the lack of any other nearby galaxies suggests that UGC 08146 is relatively isolated. Stil & Israel (2002) propose that UGC 08146 may be loosely associated with two other dwarf galaxies, DDO 123 and UGC 7544. If these galaxies are part of a loose galaxy group, the detected H I and the possible O VI absorption at  $z = 0.00229$  may sample one or more filaments in the hot intragroup gas. The feature that we have (tentatively) identified as O VI  $\lambda 1031.9$  absorption in the  $z = 0.00229$  absorber (see §3.2.1 and Fig. 13) is very broad, ranging from  $-100$  to  $+120 \text{ km s}^{-1}$ . This is much broader than what would be expected for pure thermal broadening for O VI based on the H I  $b$  value of

$\sim 42 \text{ km s}^{-1}$ . For pure thermal broadening one expects  $b(\text{O VI})=b(\text{H I})/4 \approx 10.5 \text{ km s}^{-1}$  because of the 16 times higher atomic weight of oxygen. However, the (very uncertain) width for O VI rather corresponds to  $b > 150 \text{ km s}^{-1}$ . Thus, if real, the O VI might trace very hot intragroup gas with a large velocity dispersion, while the H I samples somewhat cooler gas that is more confined. A value of  $b > 150 \text{ km s}^{-1}$  for hot intragroup gas would be in good agreement with typical line-of-sight velocity dispersions observed in loose groups of galaxies (e.g., Tucker et al. 2000). Additional UV and optical data would be very helpful to further investigate the possible connection between the  $z = 0.00229$  absorber and UGC 08146.

### 3.6.3. *Galaxies and Galaxy Groups near $z = 0.009$*

Six objects listed by NED (four galaxies and two galaxy groups) have redshifts between 0.00858 and 0.00953. They all could be related to the absorption system at  $z = 0.00760$ , which is detected in H I and possibly O VI (see §3.2.2). Impact parameters for the  $z = 0.00760$  system and these objects vary between 491 kpc (the galaxy UGC 08046) and 622 kpc (the galaxy group Mahtessian 185). The absorption at  $z = 0.00760$  thus may arise in the intragroup medium of WBL 425 or Mahtessian 185 (see Table 7), and/or is related to the intergalactic environment of one of the individual galaxies listed in Table 7.

### 3.6.4. *1259+5920 (+0270–0313)*

The elliptical or S0 galaxy 1259+5920 (+0270–0313) at  $z = 0.19670$  lies only  $\sim 0.7$  arcmin away from the line of sight towards PG 1259+593 (Chen et al. 2001), and most likely is associated with the two-component Ly  $\alpha$ /Ly  $\beta$  absorber at  $z = 0.19620$  (see Table 3). The impact parameter is  $\rho_{75} = 120$  kpc, suggesting that the  $z = 0.19620$  absorption occurs in the halo of 1259+5920 (+0270–0313) or in its nearby intergalactic environment.

### 3.6.5. *1259+5920 (–0234+0685)*

The late-type spiral galaxy 1259+5920 (–0234+0685) lies close to the direction of PG 1259+593 (angular separation  $\sim 1.2$  arcmin) and has a redshift ( $z = 0.24120$ ) very similar to that of the broad Ly  $\alpha$  absorber at  $z = 0.24126$  (see also Chen et al. 2001). We derive an impact parameter of  $\rho_{75} = 248$  kpc. The weak but very broad Ly  $\alpha$  absorption ( $b(\text{H I}) = 89.1 \pm 6.9 \text{ km s}^{-1}$ ) thus may arise in an extended halo of 1259+5920 (–0234+0685), or in an WHIM filament in the vicinity of this galaxy.



#### 4. Concluding Remarks

As the temperature of the intergalactic medium undergoes a significant change from high to low redshifts, a large fraction of the baryonic matter in the local Universe is expected to reside in the WHIM phase - a gas phase that is particularly difficult to detect. The combined FUSE and STIS spectrum of PG 1259+593 represents one of the few high-quality UV and FUV data sets currently available to study the distribution and physical properties of the low-redshift WHIM and the local Ly  $\alpha$  forest. However, the PG 1259+593 data also show how difficult the analysis of the local IGM is due to the limitations in S/N and spectral resolution in these space-based data. We have detected three intervening O VI absorption line systems towards PG 1259+593 and have found four additional candidates for which we cannot claim a firm detection. With a number of intervening O VI systems per unit redshift of  $dN_{\text{O VI}}/dz = 8 - 16$  for equivalent widths  $W_r \geq 24$  mÅ, the sight line towards PG 1259+593 adds important information about the distribution of intervening O VI absorbers in the local Universe. Savage et al. (2002) summarize previous FUSE and STIS absorption line measurements of intervening O VI in the low-redshift IGM, including the lines of sight toward H 1821+643, PG 0953+415, PG 0804+761, and 3C 273 (Tripp, Savage & Jenkins 2000; Oegerle et al. 2000; Tripp & Savage 2000; Richter et al. 2001a; Sembach et al. 2001). Six O VI systems are detected above an equivalent width limit of 50 mÅ for the O VI  $\lambda 1031.9$  line, suggesting that  $dN_{\text{O VI}}/dz = 14^{+9}_{-6}$  for  $\langle z \rangle = 0.09$ , and therefore  $\Omega_b(\text{O VI}) \geq 0.002 h_{75}^{-1}$  for an average metallicity of 0.1 solar (for details see Savage et al. 2002). The line of sight towards PG 1259+593 consists of 3 – 5 more intervening O VI systems with  $W_r \geq 50$  mÅ, in agreement with the previous observations and  $dN_{\text{O VI}}/dz$  estimates. The problem of having to separate clearly detected O VI systems from the many tentative absorbers yet remains somewhat unsatisfying, and more accurate sight-line analyses appear to be necessary to reduce the yet considerable uncertainty for  $\Omega_b(\text{O VI})$ .

The FUSE and STIS absorption line measurements suggest that intervening O VI absorption lines reliably trace the WHIM in the low-redshift Universe, although some O VI may also arise in low-density, photoionized gas (see Savage et al. 2002). We note at this point that the collisional ionization interpretation for most of the weak O VI absorbers holds only for the low-redshift Universe, where a significant fraction of the intergalactic gas is expected to reside in the WHIM phase (Cen & Ostriker 1999) at  $T \geq 10^5$  K. At higher redshifts ( $z \sim 2$ ), a larger fraction of the O VI absorbing systems apparently traces intergalactic structures that are photoionized by a hard UV background. This is evident from the narrow line widths ( $b_{\text{O VI}} \leq 10 \text{ km s}^{-1}$ ) of some of the weaker O VI absorbing structures at high redshifts with  $\log N(\text{H I}) \leq 15$  (Bergeron et al. 2002; Carswell, Schaye & Kim 2002). Such small  $b$  values are inconsistent with temperatures  $T \geq 10^5$  K. However, the results of Simcoe, Sargent, & Rauch (2002) imply that collisional ionization has to be taken into account for the higher-column density O VI systems at  $z \sim 2$  ( $\log N(\text{H I}) \geq 15$ ), as this gas possibly traces shock-heated material from supernova-driven galactic winds. An important but yet unanswered question is, what baryonic mass fraction of the WHIM at low  $z$  is not detected in studies that concentrate solely on O VI absorption? WHIM clouds that have intrinsically low gas column densities, and/or low metallicities, and/or very high temperatures ( $\geq 10^{5.5}$  K) are difficult to detect

in O VI absorption. Other high ions such as Ne VIII may trace the WHIM in a higher temperature regime, but our study (and other measurements) provide no evidence that there exists a significant number of detectable intervening Ne VIII absorbers at low redshifts. Towards PG 1259+593 we have not found significant ( $\geq 3\sigma$ ) Ne VIII absorption in any of the absorption systems. The possibility to detect Ne VIII absorption in FUSE and STIS data, however, is probably low due to the relatively low cosmic abundance of neon compared to oxygen ( $\log (\text{Ne}/\text{O})_{\odot} = -0.61$ ; Allende Prieto, Lambert, & Asplund 2001, 2002; Anders & Grevesse 1989) and the lower S/N of the FUSE data in the spectral region where the Ne VIII lines are accessible. In two systems ( $z = 0.22313$  and  $z = 0.25971$ ) Ne VIII absorption may be present at low statistical confidence ( $\leq 1.9\sigma$ ); if more Ne VIII data from other sight lines will become available, one may find evidence for Ne VIII absorption in WHIM absorbers by stacking together a larger number of Ne VIII velocity profiles. Observations of the X-ray absorption in the lines of O VII, O VIII and other species are becoming an important way to trace hot gas in the local intergalactic medium (Rasmussen, Kahn & Paerels 2003; Fang et al. 2002; Nicastro et al. 2002). But even with the most modern X-ray observatories, such as *Chandra* and *XMM-Newton*, observations of intervening intergalactic X-ray absorbers represent a challenging task, and so far the number of detected X-ray absorption features in the IGM is quite low. Thus, good statistics about the low-redshift X-ray forest will not be readily available in the near future.

A promising approach to trace the WHIM at temperatures up to  $T \sim 10^6$  K is to search for broad, shallow Ly  $\alpha$  absorbers. With the FUSE and STIS data presented here we possibly have found for the first time evidence that at least part of the WHIM up to  $T \sim 10^6$  K may be traced by Ly  $\alpha$  absorption. Support for the detectability of gas this hot in Ly  $\alpha$  comes from X-ray observations. Studies of the immediate intergalactic environment of the Milky Way suggest the possible presence of an WHIM filament with an O VII column density of  $\sim 10^{16} \text{ cm}^{-2}$  (see Rasmussen, Kahn, & Paerels 2003). If this O VII column density is representative for a WHIM absorber, and if we further assume a temperature of  $10^6$  K together with collisional ionization equilibrium (Sutherland & Dopita 1993) and a metallicity of the gas of 0.1 solar, we would expect to see Ly  $\alpha$  absorption at the level of  $\log N(\text{H I}) \approx 13.5$  and  $b \approx 130 \text{ km s}^{-1}$ , in line with some of the broader absorbers towards PG 1259+593 listed in Table 5. Depending on the column density and temperature distribution of the WHIM absorbers, it may be that only a small fraction of these systems can be detected in H I absorption. There could be, however, also a number of WHIM systems that are somewhat cooler than the X-ray absorbing systems, and thus have larger neutral gas column densities and possibly O VI absorption. The relatively strong and broad  $z = 0.31978$  absorber towards PG 1259+593 could be an example for such a “transition system”. The H I  $b$  value ( $\sim 74 \text{ km s}^{-1}$ ), the probable detection of O VI absorption and the resulting O VI  $b$  value ( $\sim 19 \text{ km s}^{-1}$ ), as well as the limits derived for O IV and Ne VIII are all consistent with a WHIM absorber at  $T \sim 3 \times 10^5$  K. This system thus may represent the best observational evidence that some broad Ly  $\alpha$  absorbers indeed trace the WHIM.

Davé & Tripp (2001) have performed hydrodynamic simulations to produce artificial absorption line spectra to compare the characteristics of the simulated Ly  $\alpha$  absorption with STIS absorption

line data for the low-redshift IGM towards PG 0953+415 and H 1821+643. They use an automated Voigt profile fitting technique to determine column densities and  $b$  values for both artificial and real spectra, finding excellent agreement between these two data sets. As shown in their Fig. 4, they do not find a population of very broad Ly  $\alpha$  absorbers that would trace the WHIM at  $T > 3 \times 10^5$  K. However, it is not clear what sensitivity the automated fitting routine has for very broad, shallow absorption features. Since artificial and real data are fitted in an identical manner, the routine possibly could miss weak absorbers with large Doppler parameters, mainly because such features would be treated as continuum undulations and removed in the normalization process. Thus, a population of weak, broad Ly  $\alpha$  lines may remain unnoticed in the simulated spectra and the STIS data of PG 0953+415 and H 1821+643 using this technique. A careful re-inspection of these data is necessary to clarify this point. Additional high S/N observations with STIS will be important to investigate whether the broad features we have detected in the line of sight towards PG 1259+593 really arise from high-temperature WHIM absorbers, or whether they only represent a mixture of instrumental effects and unresolved absorption components. Having available a larger number of sight lines with different background continua clearly would help to tackle some of the systematic effects that hamper the non-ambiguous identification of broad, shallow absorption features. Also, combined X-ray and FUV observations will help to answer the question of whether broad Ly  $\alpha$  features can serve as a reliable tracer for gas with temperatures up to  $\sim 10^6$  K. If so, studying broad Ly  $\alpha$  absorbers in high S/N FUV spectra could be a big step forward to understand the distribution and physical properties of the WHIM at low redshifts and its baryonic content.

## 5. Summary

We have analyzed intergalactic absorption in FUSE and STIS FUV spectra of the QSO PG 1259+593 ( $z_{\text{em}} = 0.478$ ).

1. We identify 135 intergalactic absorption lines at  $W_r \geq 10$  mÅ, including 4 – 8 metal line systems that are detected in one or more lines of C III, C IV, O III, O IV, O VI, and Si III. We determine equivalent widths and column densities for 72 absorption line systems. The overall distribution of Doppler parameters ( $b$  values) and column densities for the local Ly  $\alpha$  forest towards PG 1259+593 is consistent with results from previous studies considering lines with  $b \leq 40$  km s $^{-1}$ .

2. We discuss physical conditions in the metal-line systems. The two strongest absorption systems at  $z = 0.04606$  and  $0.21949$  consist of multiple absorption components with different gas-phases. For the single-component system at  $z = 0.29236$  the analysis of H I, C III, O III, and O IV absorption implies abundance ratios of  $\log [\text{O}/\text{H}] = -0.5$  and  $\log [\text{C}/\text{O}] = -0.5$ . This is comparable with what is found in low-metallicity dwarf galaxies.

3. The number of intervening O VI absorbers along this line of sight is 3 – 6 for a typical equivalent width limit of  $W_\lambda \geq 24$  mÅ. Together with an unobscured redshift path of  $\Delta z \approx 0.368$  this number implies  $dN_{\text{O VI}}/dz \sim 8 - 16$  in this direction. At this equivalent width limit, the finding

is consistent with  $dN_{\text{O VI}}/dz$  results from previous absorption line studies. The result supports the idea that intervening O VI systems trace a significant fraction of the baryons in the local Universe residing in the warm phase of the warm-hot intergalactic medium (WHIM).

4. A broad Ly  $\alpha$  absorption system ( $b \approx 74 \text{ km s}^{-1}$ ) is found at  $z = 0.31978$ . The system is possibly also detected in O VI  $\lambda 1031.9$  absorption. This absorber may represent a collisionally ionized intergalactic gas cloud at a temperature of  $\sim 3 \times 10^5 \text{ K}$  and a very low but uncertain oxygen abundance, (O/H), of  $4.3 \times 10^{-3}$  solar.

5. We detect a large number of broad Ly  $\alpha$  lines along the line of sight towards PG 1259+593 with Doppler parameters  $b \geq 40 \text{ km s}^{-1}$  and relatively low column densities ( $\log N(\text{H I}) < 14$ ). If thermal broadening determines the large widths of these lines, their  $b$  values correspond to temperatures between  $10^5$  and several  $10^6 \text{ K}$ . Although some of these lines may be composites of several blended, unresolved absorption features, caused by continuum undulations, or are produced by gas flows and Hubble broadening, we speculate that at least some of these features represent WHIM absorbers that are not detected in O VI absorption. From a sub-set of eight well-detected broad Ly  $\alpha$  lines (BL) with  $40 \text{ km s}^{-1} < b < 100 \text{ km s}^{-1}$  we estimate  $dN_{\text{BL}}/dz \approx 23$  and  $\Omega_b = 0.0031 h_{75}^{-1}$ . If the line widths are dominated by thermal Doppler broadening, then these absorbers would contain a large fraction of the baryons in the low-redshift IGM.

This work is based on data obtained for the the Guaranteed Time Team by the NASA-CNES-CSA FUSE mission operated by the Johns Hopkins University. Financial support has been provided by NASA contract NAS5-32985. The STIS observations of PG1259+593 were obtained for HST GO program 8695, with financial support from NASA grant GO-8695.01-A from the Space Telescope Science Institute. P.R. was supported by the research grant RI 1124 from the *Deutsche Forschungsgemeinschaft*. T.M.T received support from NASA Long Term Space Astrophysics grant NAG5-11136. P.R. acknowledges the opportunity to visit the Osservatorio Astrofisico di Arcetri, Florence, Italy between spring 2002 and fall 2003; a substantial part of this paper was written at this institute.

## REFERENCES

- Allende Prieto, C., Lambert, D. L., & Asplund, M. 2001, ApJ, 556, L63
- Allende Prieto, C., Lambert, D. L., & Asplund, M. 2002, ApJ, 573, L137
- Anders F., & Grevesse, N. 1989, Geochim. Cosmochim. Acta, 53, 197
- Bahcall, J.N., et al. 1993, ApJS, 87, 1
- Bergeron, J., Aracil, B., Petitjean, P., & Pichon, C. 2002, A&A, 396, L11
- Bowers, C.W., et al. 1998, Proc.SPIE, 3356, 401

- Carswell, R., Schaye, J., & Kim, T.-S. 2002, *ApJ*, 578, 43
- Cen, R., & Ostriker, J. 1999, *ApJ*, 514, 1
- Cen, R., Tripp, T.M., Ostriker, J.P., & Jenkins, E.B. 2001, *ApJ*, 559, L5
- Chen, H.-W., & Prochaska, J.X. 2000, *ApJ*, 543, L9
- Chen, H.-W., Lanzetta, K.M., Webb, J.K., & Barcons, X. 2001, *ApJ*, 559, 654
- Chen, X., Weinberg, D.H., Katz, N., & Davé, R. 2003, *ApJ*, 594, 42
- Collins, J.A., Shull, J.M., & Giroux, M.L. 2002, *ApJ*, 585, 336
- Davé, R., & Tripp, T.M. 2001, *ApJ*, 553, 528
- Fang, T., & Bryan, G.L. 2001, *ApJ*, 561, L31
- Fang, T., Marshall, H.L., Lee, J.C., Davis, D.S., & Canizares, C.R. 2002, *ApJ*, 572, L127
- Ferland, G. 1996, *Hazy, a Brief Introduction to CLOUDY 90*, Univ. Kentucky Phys. Dept. Int. Rep.
- Fox, A.J., Savage, B.D., Wakker, B.P., Richter, P., Sembach K.R., & Tripp, T.M. 2004, *ApJ*, 602, 738
- Haardt, F. & Madau, P. 1996, *ApJ*, 461, 20
- Janknecht, E., Baade, R., & Reimers, D. 2002, *A&A*, 391, L11
- Kim, T.-S., Carswell, R.F., Cristiani, S., D’Odorico, S., & Giallongo, E. 2002, *MNRAS*, 335, 555
- Kimble, R.A., et al. 1998, *ApJ*, 492, L83
- Landsman, W., & Bowers, C.W. 1997, in *HST Calibration Workshop with a new generation of Instruments*, ed. S. Casertano, R. Jedrzejewski, C.D. Keyes, & M. Stevens (Baltimore: STScI), 132
- Leitherer, C., et al. 2002, *STIS Instrument Handbook, v6.0*, (Baltimore: STScI)
- Lu, L., Sargent, W.L.W., Womble, D.S., & Takada-Hidai, M. 1996, *ApJ*, 472, 509
- Moos, H.W., et al. 2000, *ApJ*, 538, L1
- Morton, D.C. 1991, *ApJS*, 77, 119
- Morton, D.C. 2003, in preparation
- Nicastro, F., et al. 2002, *ApJ*, 573, 157

- Oegerle, W.R., et al. 2000, ApJ, 538, L23
- Penton, S.V., Shull, J.M., & Stocke, J.T. 2000, ApJ, 544, 150
- Rasmussen, A., Kahn, S.M., & Paerels, F. 2003, astro-ph/0301183
- Rauch, M., et al. 1997, ApJ, 489, 7
- Rauch, M. 1998, ARA&A, 36, 267
- Rhee, M.-H., & van Albada, T.S. 1996, A&AS, 115, 407
- Richter, P., Savage, B.D., Wakker, B.P., Sembach, K.R., & Kalberla, P.M.W. 2001a, ApJ, 549, 281
- Richter, P., et al. 2001b, ApJ, 559, 318
- Sahnou, D.J., et al. 2000, ApJ, 538, L7
- Savage, B.D., & Sembach, K.R. 1991, ApJ, 379, 245
- Savage, B.D., Sembach, K.R., Tripp, T.M., & Richter, P. 2002, ApJ, 564, 631
- Sembach, K.R., Howk, J.C., Savage, B.D., Shull, J.M., & Oegerle, W.R. 2001, ApJ, 561, 573
- Sembach, K.R., et al. 2004, ApJS, 150, 387
- Shull, J. M. 2003, in The IGM/Galaxy Connection: The Distribution of Baryons at  $z = 0$ , eds. J. L. Rosenberg and M. E. Putman (Dordrecht: Kluwer Academic Pub.), 1
- Stil, J.M., & Israel, F.P. 2002, A&A, 389, 29
- Stocke, J.T., Shull, J.M., Penton, S., Donahue, M., & Carilli, C. 1995, ApJ, 451, 24
- Sutherland, R.S., & Dopita, M.A. 1993, ApJS, 88, 253
- Tripp, T.M., Savage, B.D., & Jenkins, E.B. 2000, ApJ, 534, L1
- Tripp, T.M., & Savage, B.D. 2000, ApJ, 542, 42
- Tripp, T.M., Giroux, M.L., Stocke, J.T., Tumlinson, J., & Oegerle, W.R. 2001, ApJ, 563, 724
- Tripp, T.M., et al. 2002, ApJ, 575, 697
- Tucker, D.L., et al. 2002, ApJS, 130, 237
- Verner, D., Barthel, P., & Tytler, D. 1994, A&AS, 108, 287
- Weinberg, D.H., Miralda-Escudé, J., Hernquist, L., & Katz, N. 1997, ApJ, 490, 564
- Weymann, R.J., Jannuzi, B.T., Lu, L., et al. 1998, ApJ, 506, 1

Woodgate, B.E., et al. 1998, PASP, 110, 1183

Fig. 1.— Combined FUSE and STIS spectrum of PG 1259+593. For this plot, the data have been binned to  $0.3 \text{ \AA}$  wide pixels. Note that most of the narrow interstellar and intergalactic absorption features are not resolved at this bin size. At  $\lambda > 1634 \text{ \AA}$  the STIS data have several small gaps between the individual echelle orders. At the junction between the FUSE and the STIS data at  $1180 \text{ \AA}$  the absolute flux in the FUSE LiF 2A channel is inconsistent with the (correct) flux in the STIS data ( $F_{\text{STIS}} \approx 1.5 F_{\text{FUSE}}$ ) because of dark horizontal stripes in the two-dimensional FUSE detector images (“worms”) that reduce the total flux in the respective wavelength regions (in this case for  $\lambda > 1160 \text{ \AA}$ ) and that are not accounted for in the FUSE flux calibration of PG 1259+593.

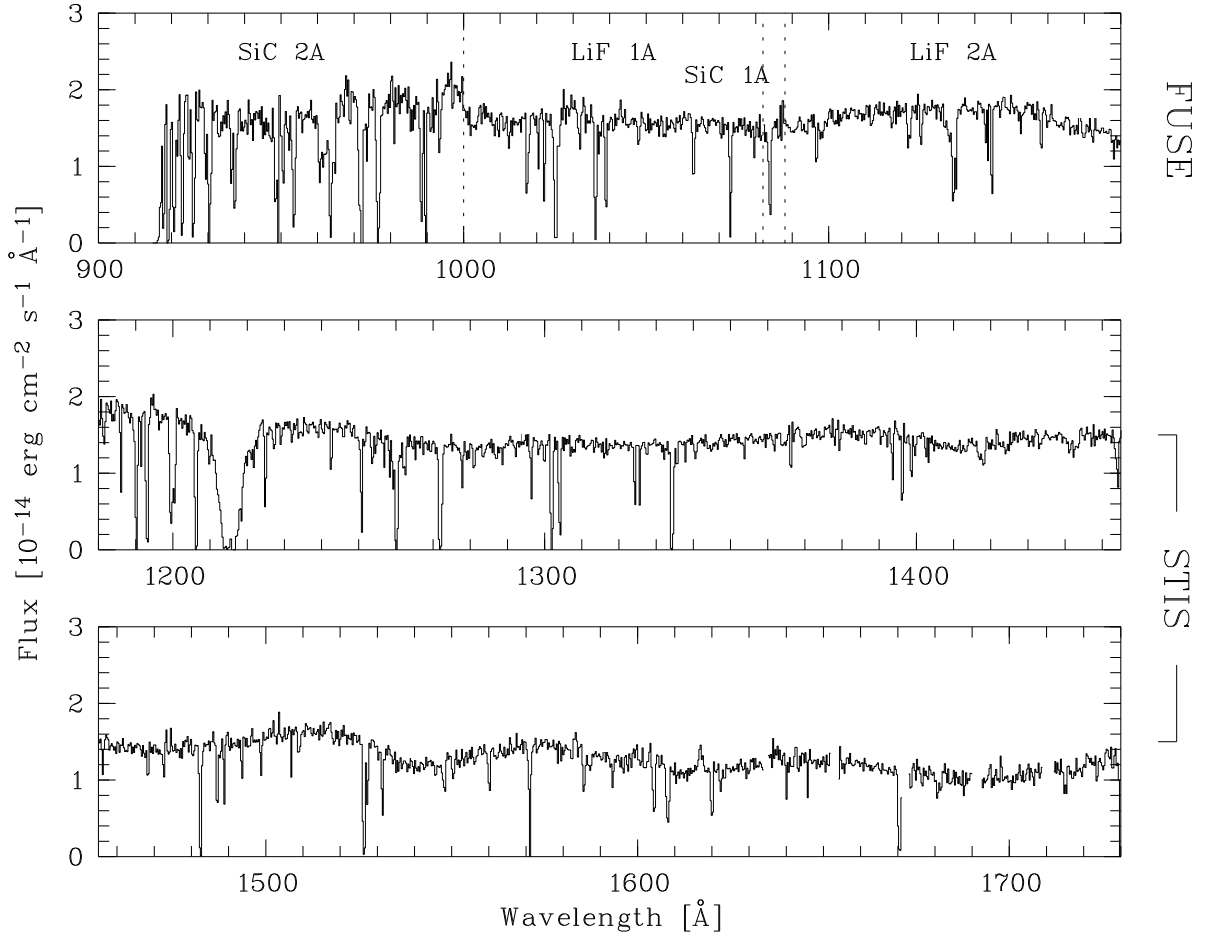




Fig. 2.— FUV spectrum of PG 1259+593 (Figs. 2-12), including FUSE data (916 – 1188 Å) and STIS data (1180 – 1729 Å). For these plots, the data have been binned to 0.025 Å wide pixels, except for the SiC 1A and SiC 2B data, which have been binned to 0.1 Å wide pixels. IGM lines are indicated with tic marks and numbers above the spectrum and are identified on the right hand side; absorption features from local interstellar lines are labeled with a star symbol. Uncertain lines and apparently broad Ly  $\alpha$  absorbers are marked with ‘?’ and ‘B’, respectively (see §2.3 for more details).

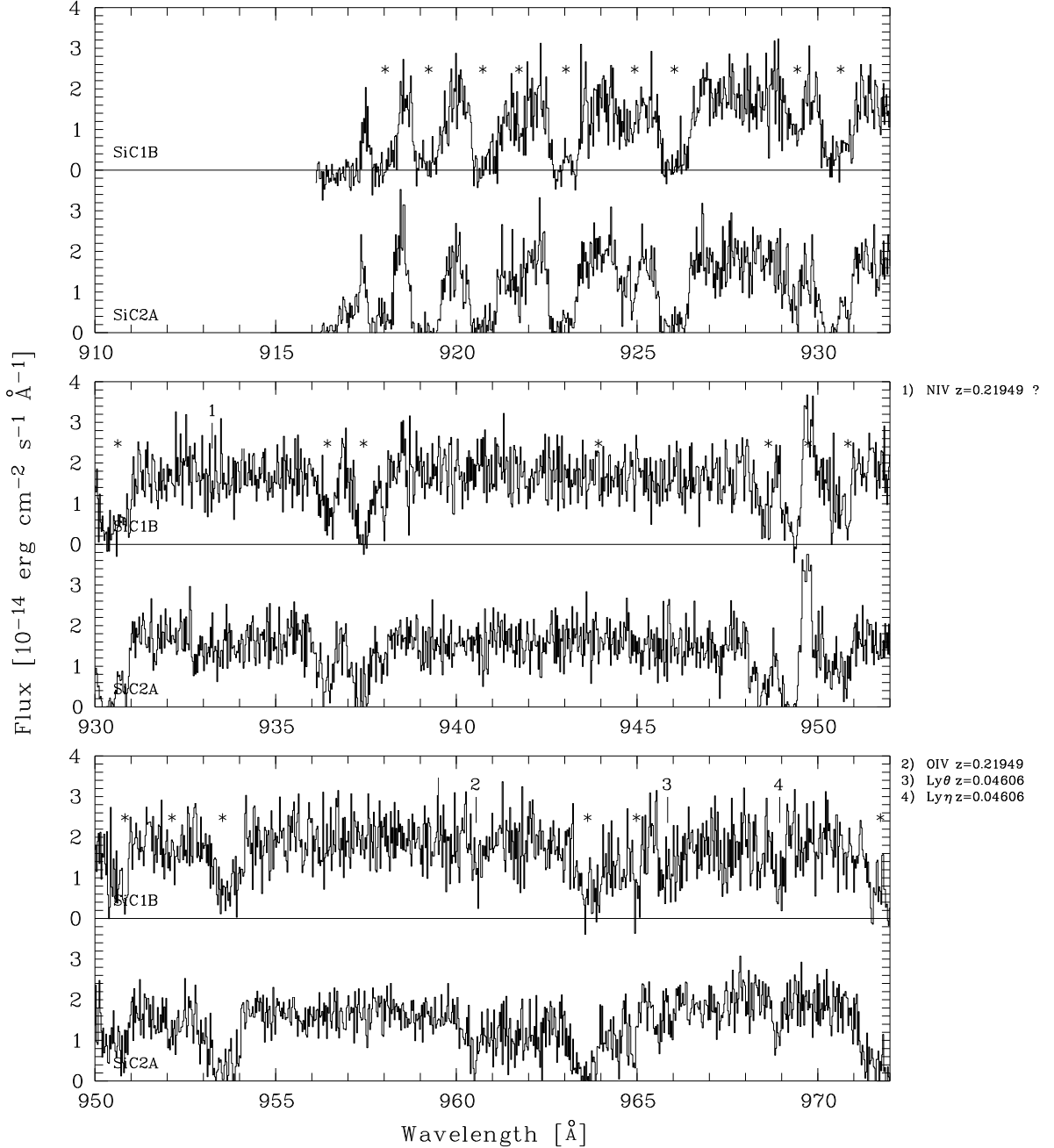


Fig. 3.— FUV spectrum of PG 1259+593 (see caption to Fig. 2).

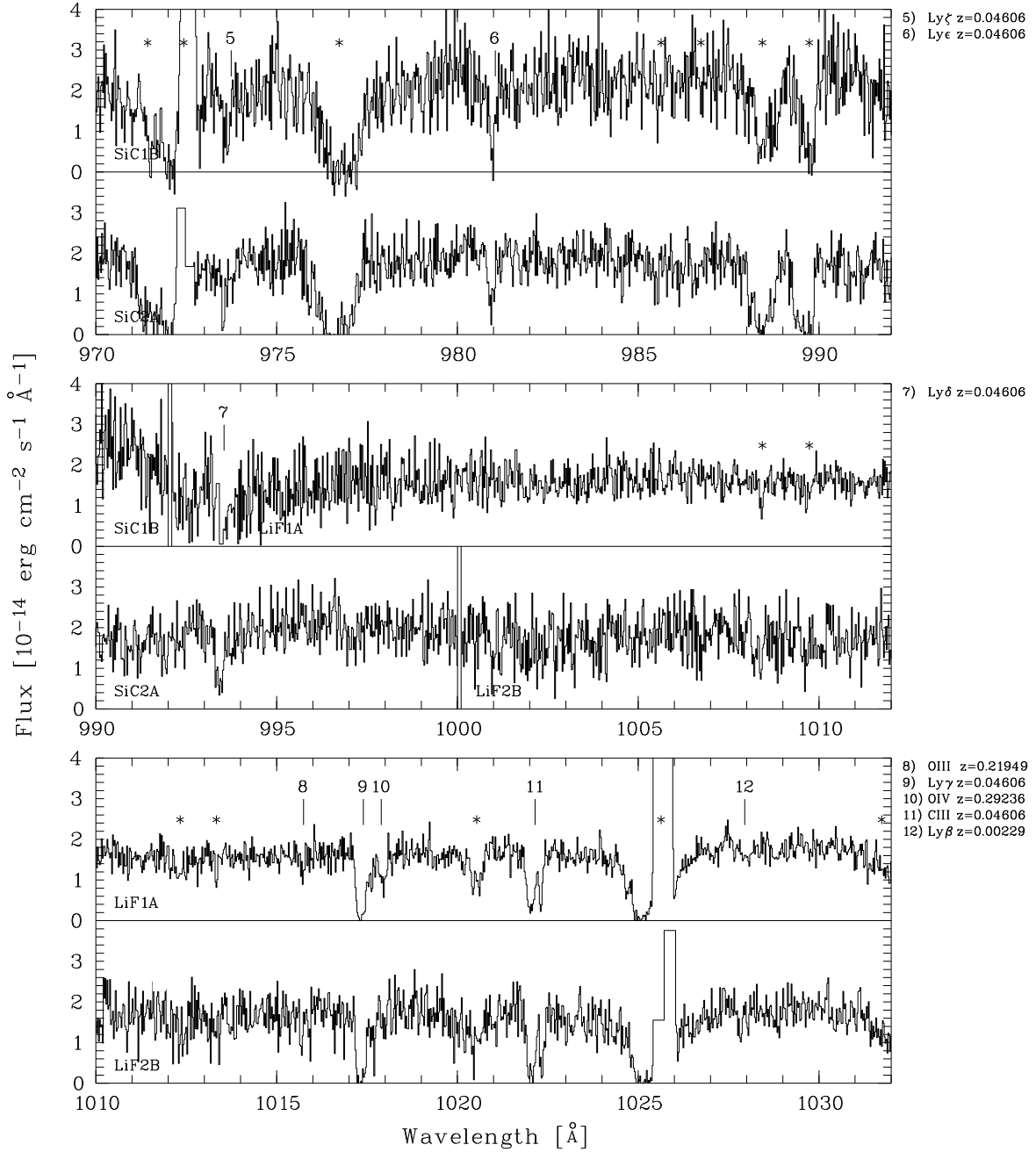


Fig. 4.— FUV spectrum of PG 1259+593 (see caption to Fig. 2).

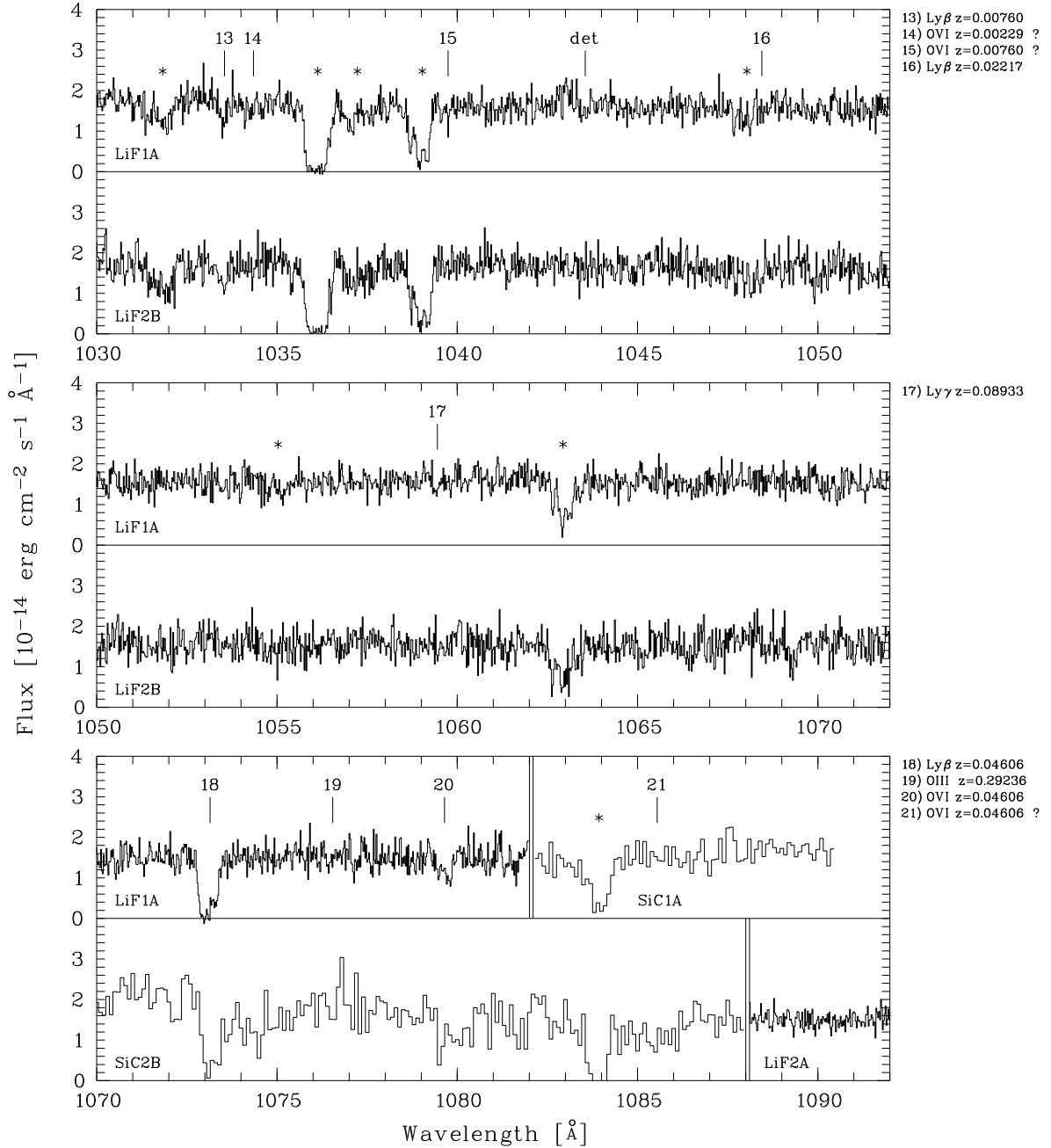


Fig. 5.— FUV spectrum of PG 1259+593 (see caption to Fig. 2).

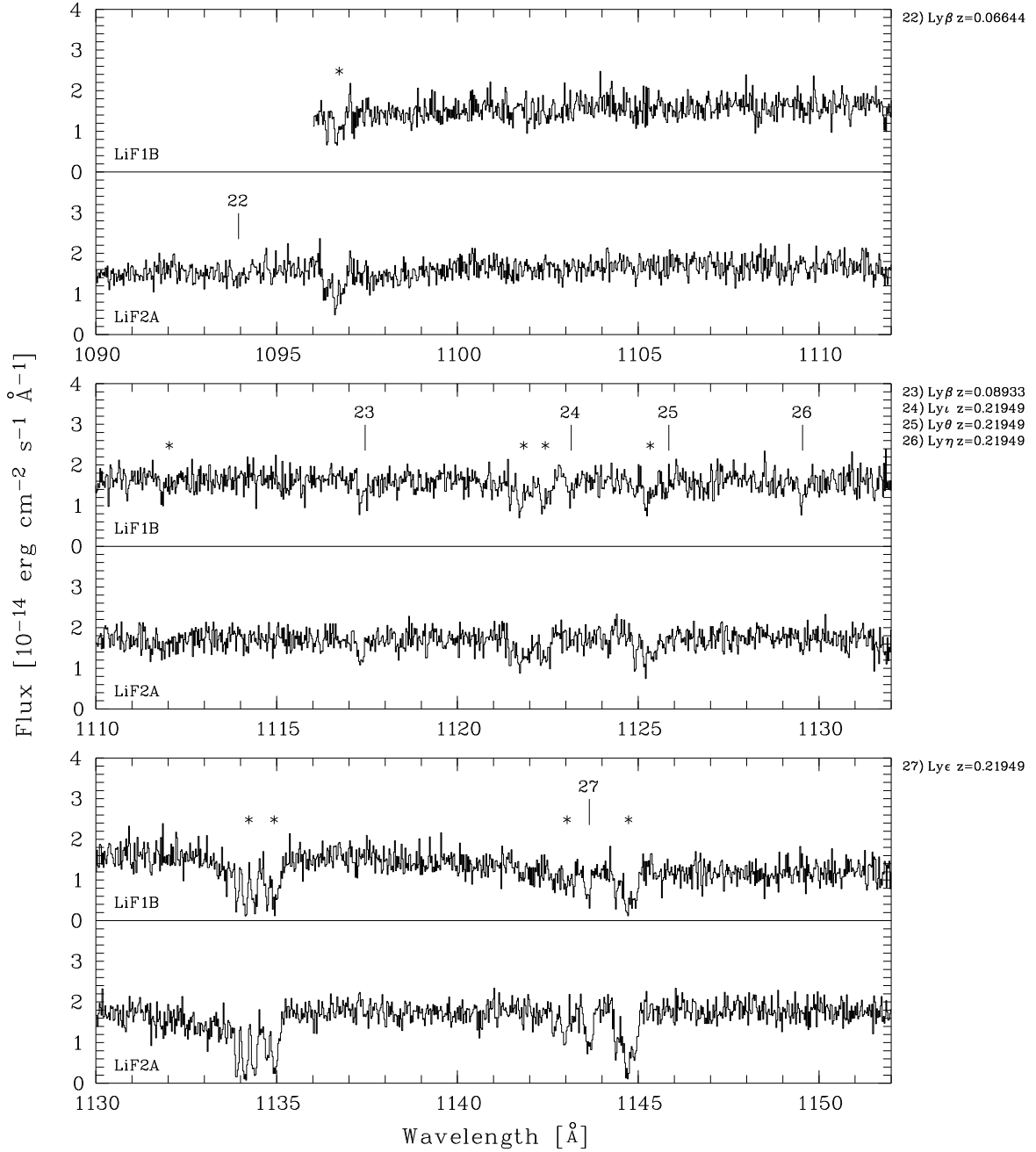


Fig. 6.— FUV spectrum of PG 1259+593 (see caption to Fig. 2).

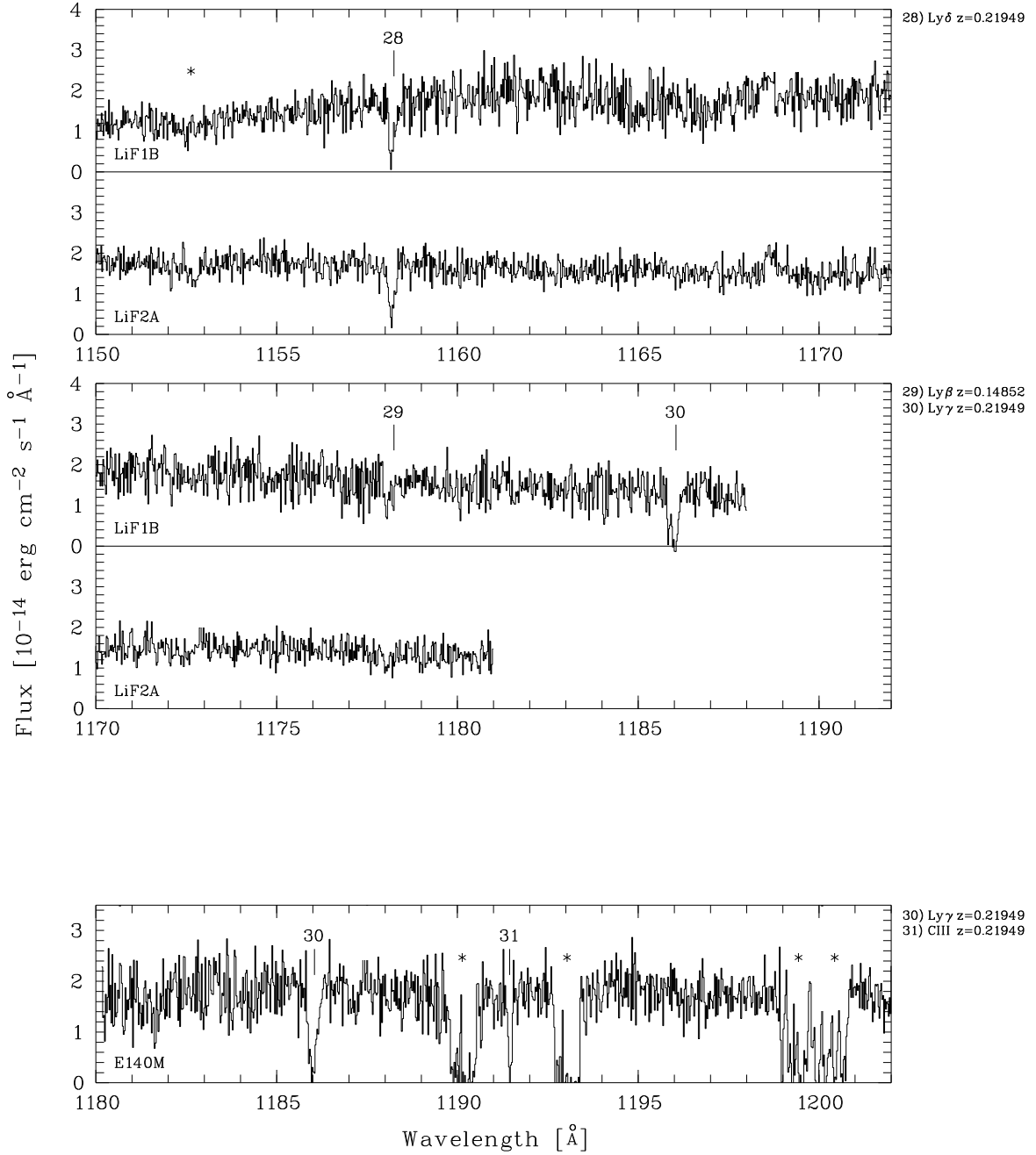


Fig. 7.— FUV spectrum of PG 1259+593 (see caption to Fig. 2).

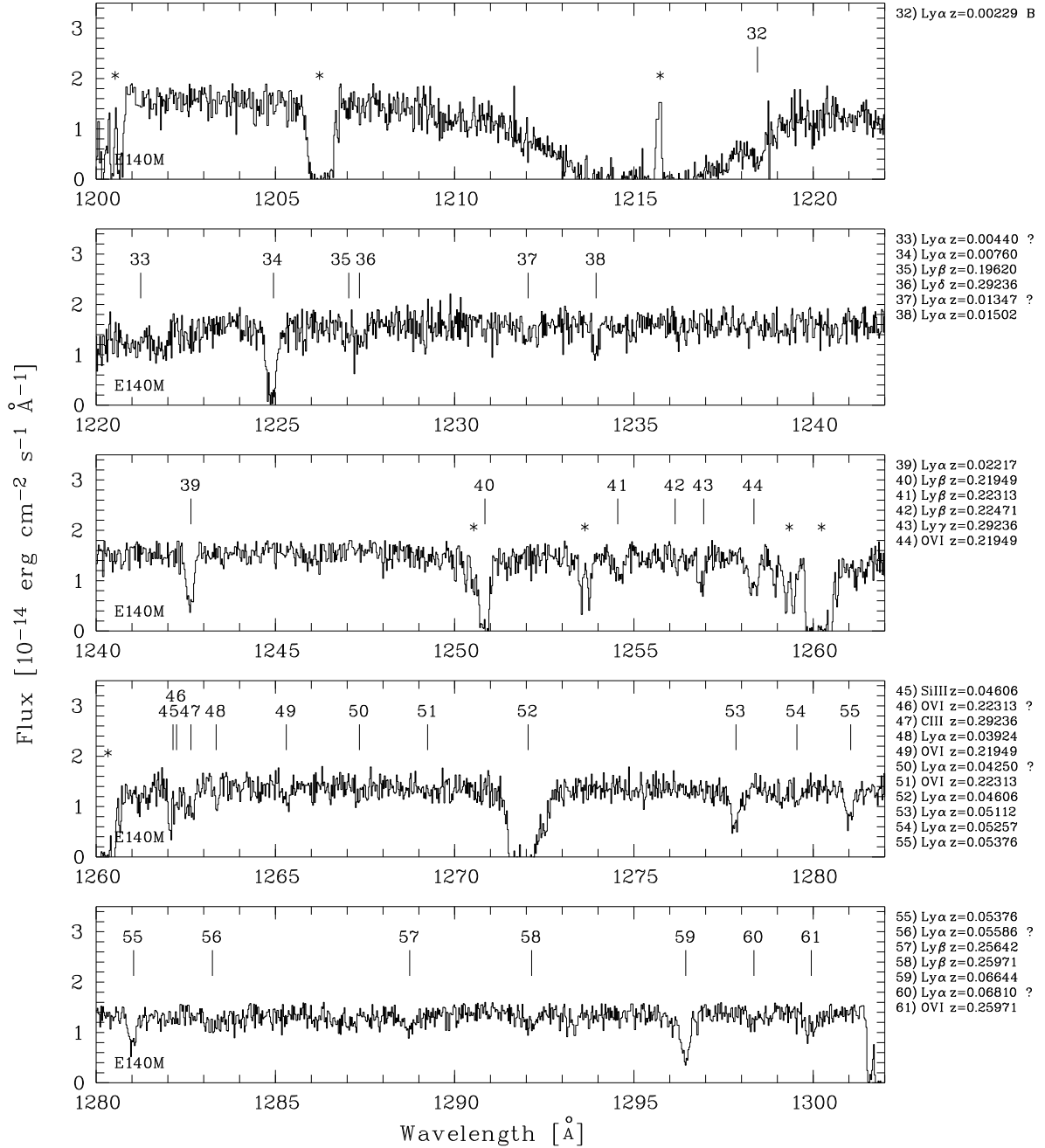


Fig. 8.— FUV spectrum of PG 1259+593 (see caption to Fig. 2).

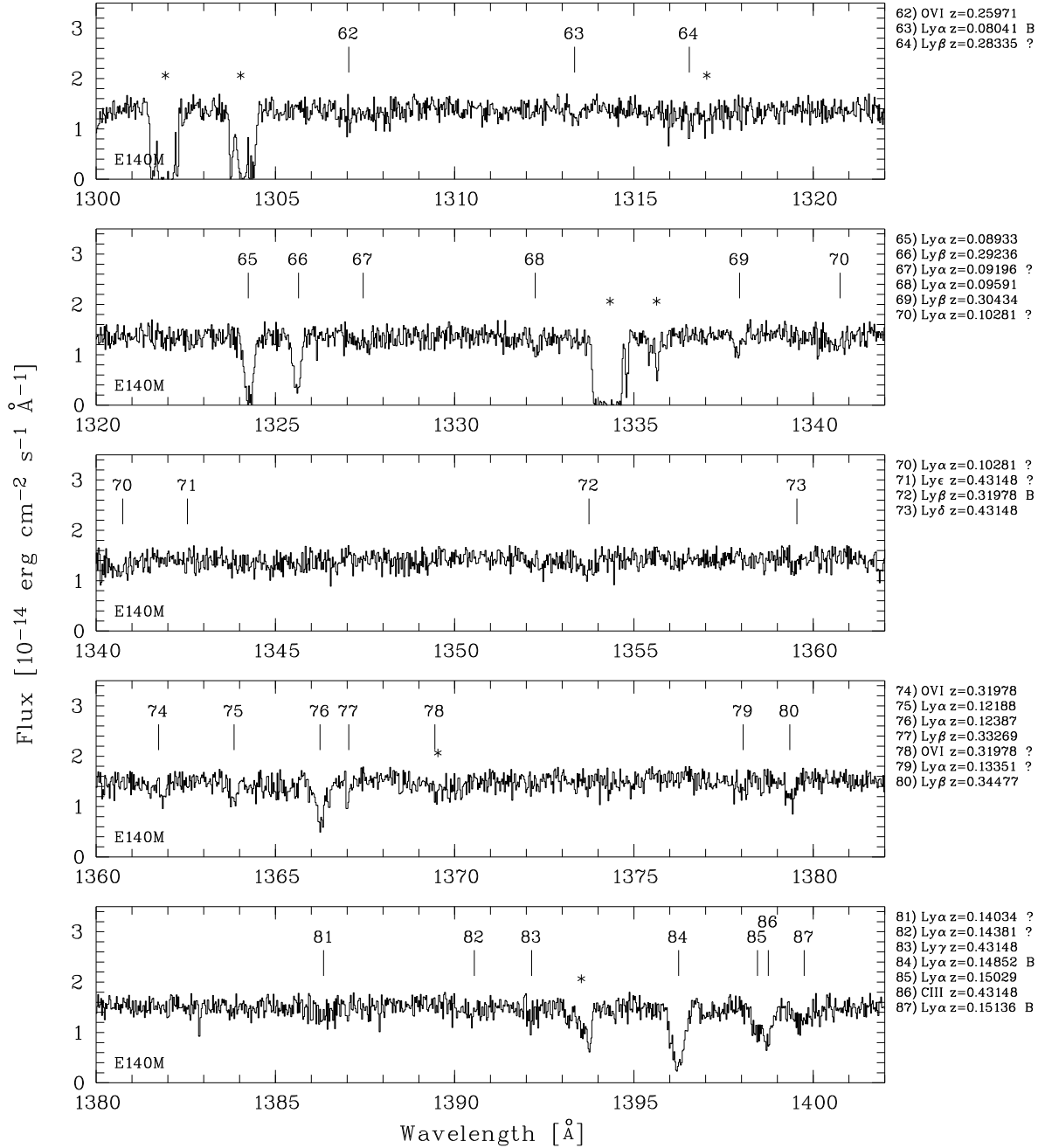


Fig. 9.— FUV spectrum of PG 1259+593 (see caption to Fig. 2).

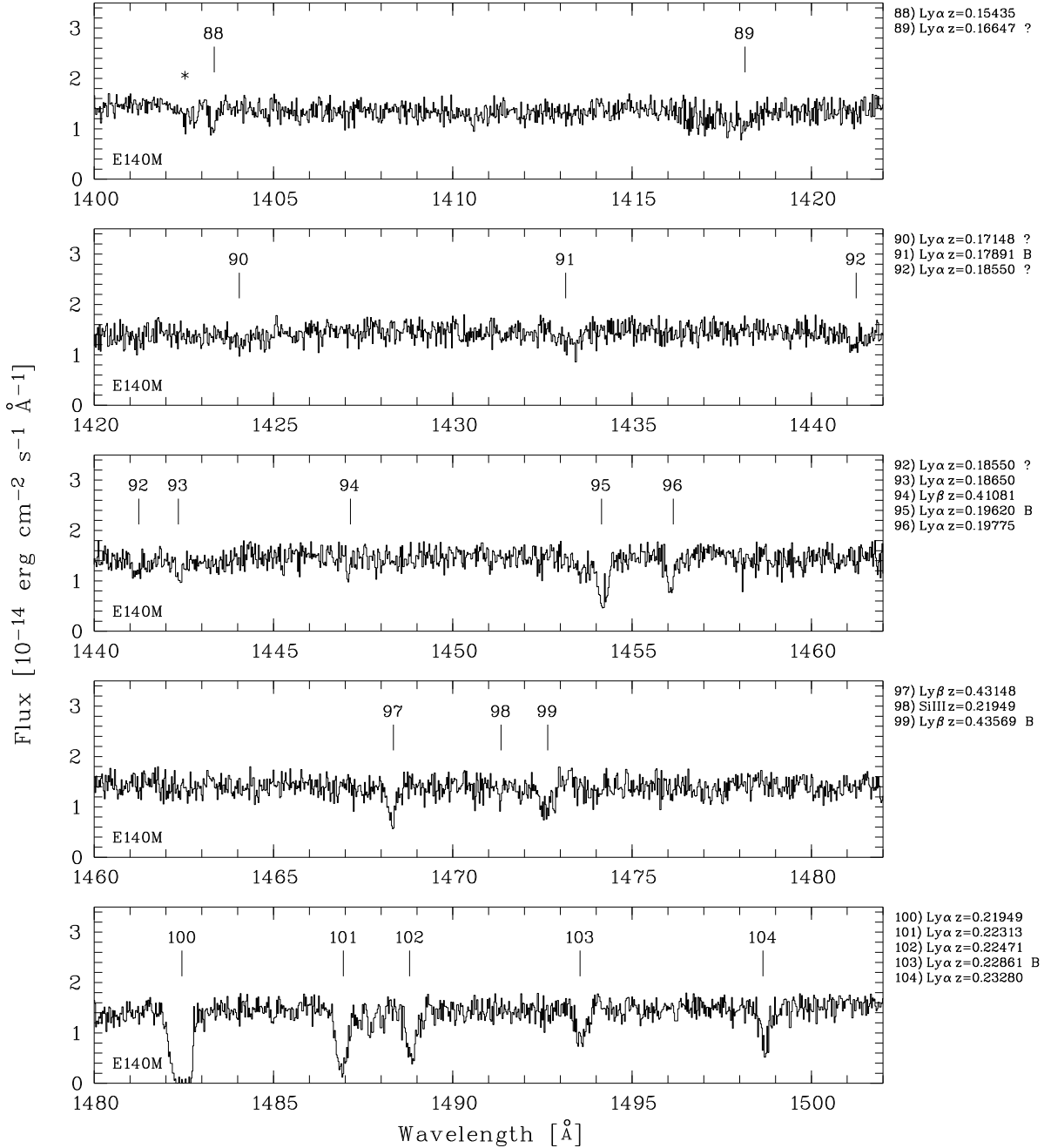




Fig. 10.— FUV spectrum of PG 1259+593 (see caption to Fig. 2).

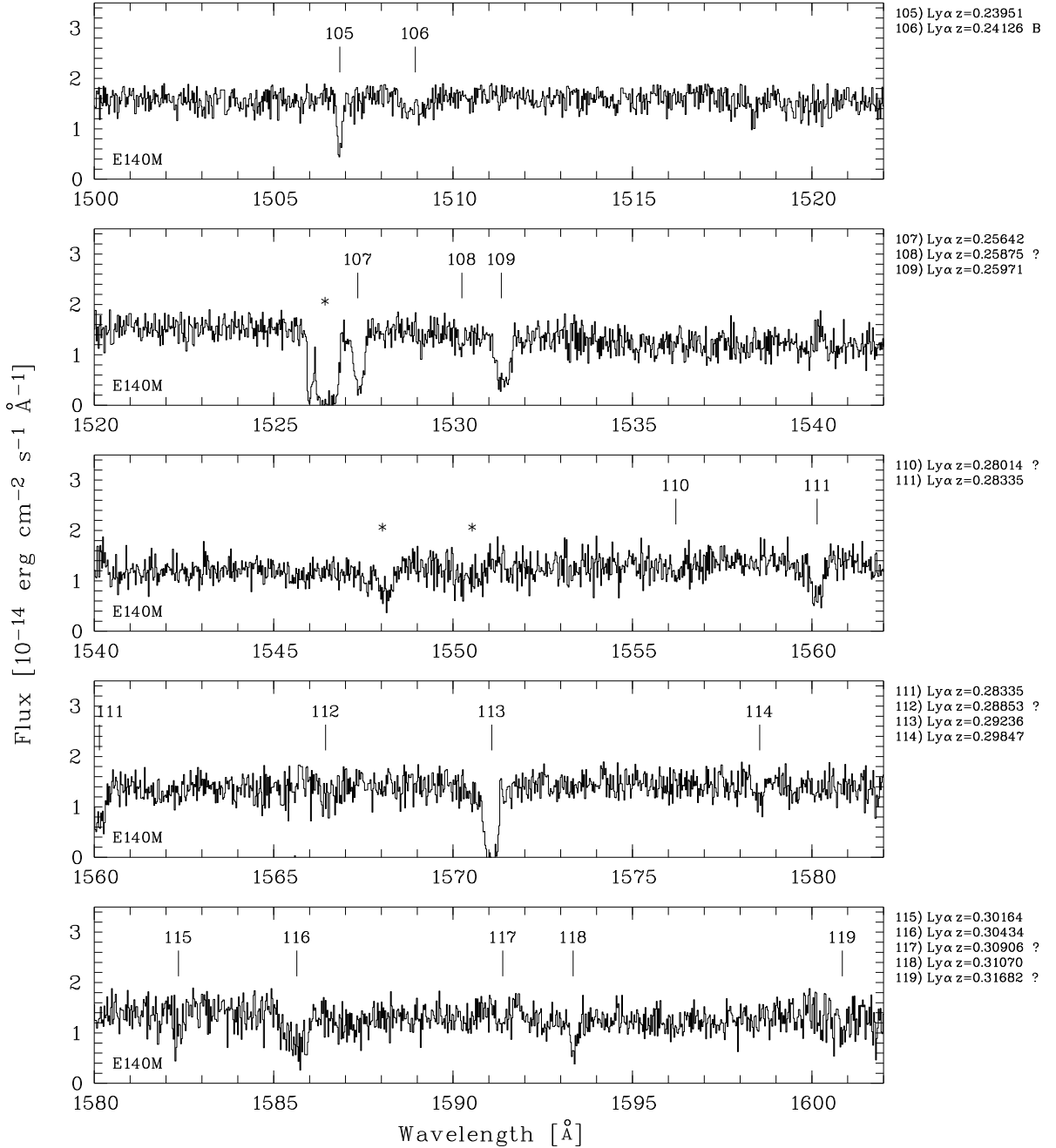


Fig. 11.— FUV spectrum of PG 1259+593 (see caption to Fig. 2).

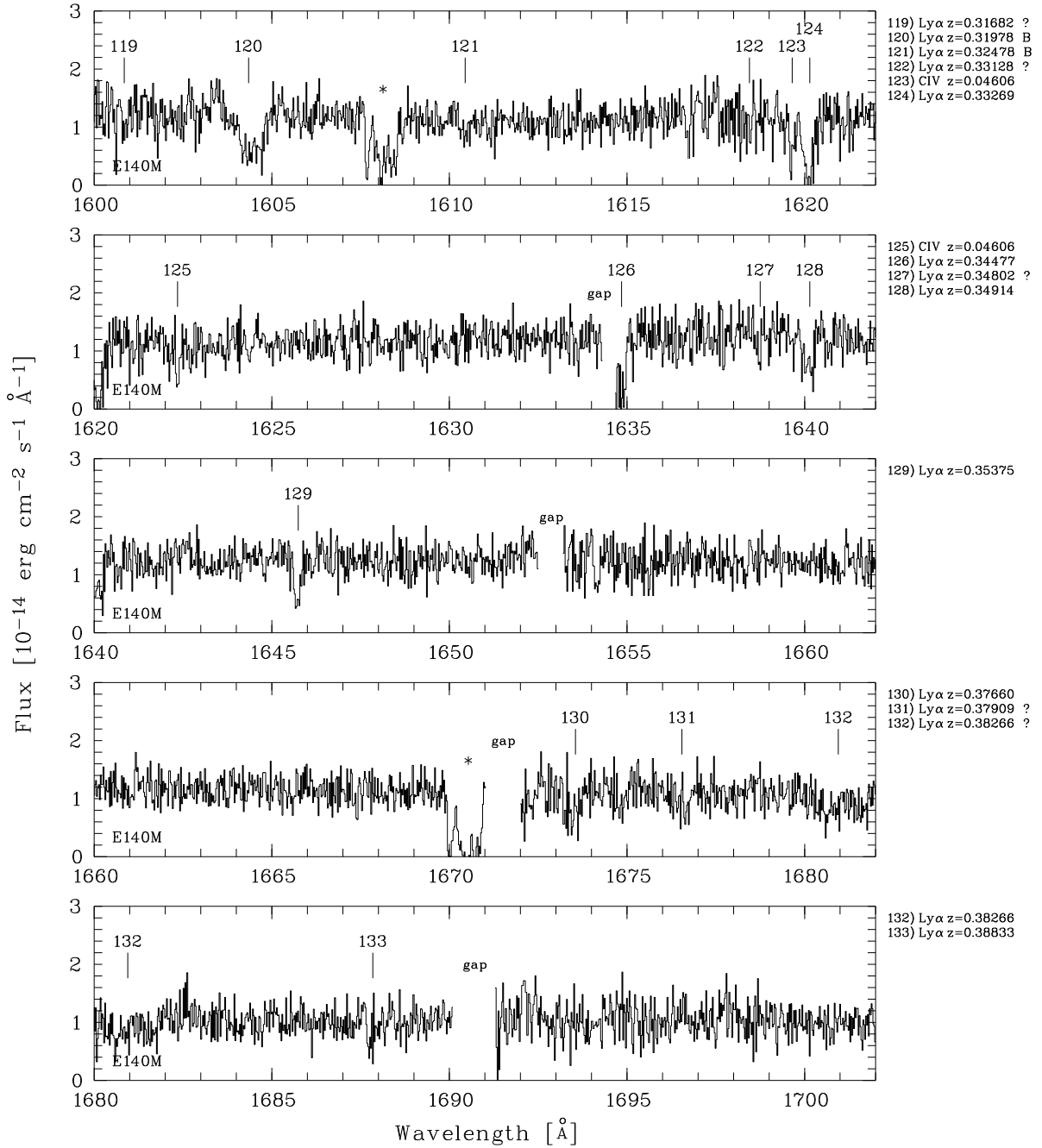


Fig. 12.— FUV spectrum of PG 1259+593 (see caption to Fig. 2).

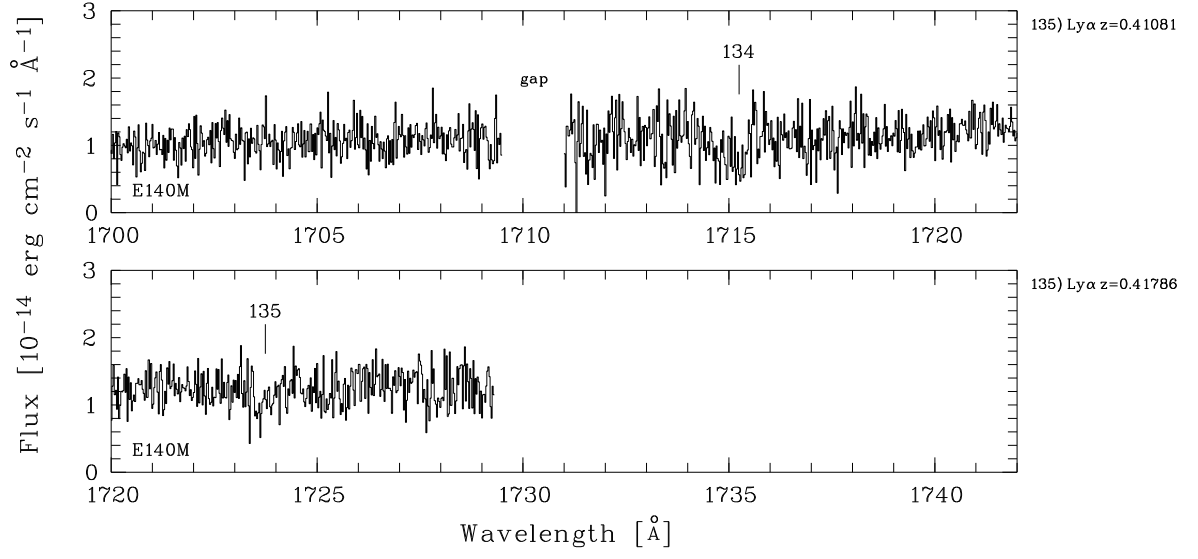


Fig. 13.— Continuum-normalized absorption profiles of multiple-line IGM absorbers towards PG 1259+593 plotted versus rest-frame velocities. For this plot, the data has been binned to  $6 \text{ km s}^{-1}$  wide pixels.

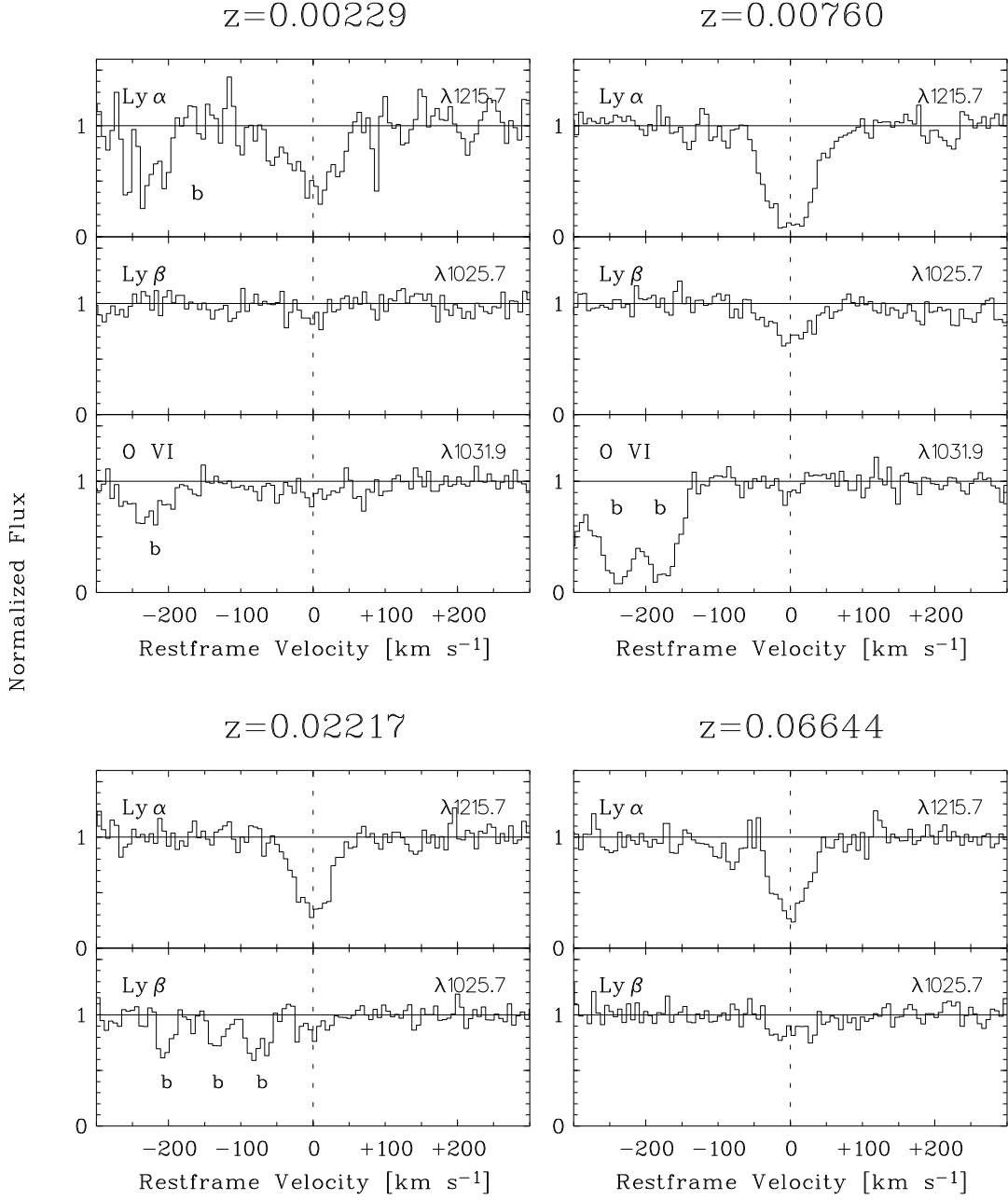


Fig. 14.— Continuum-normalized absorption profiles of multiple-line IGM absorbers towards PG 1259+593 (ctd).

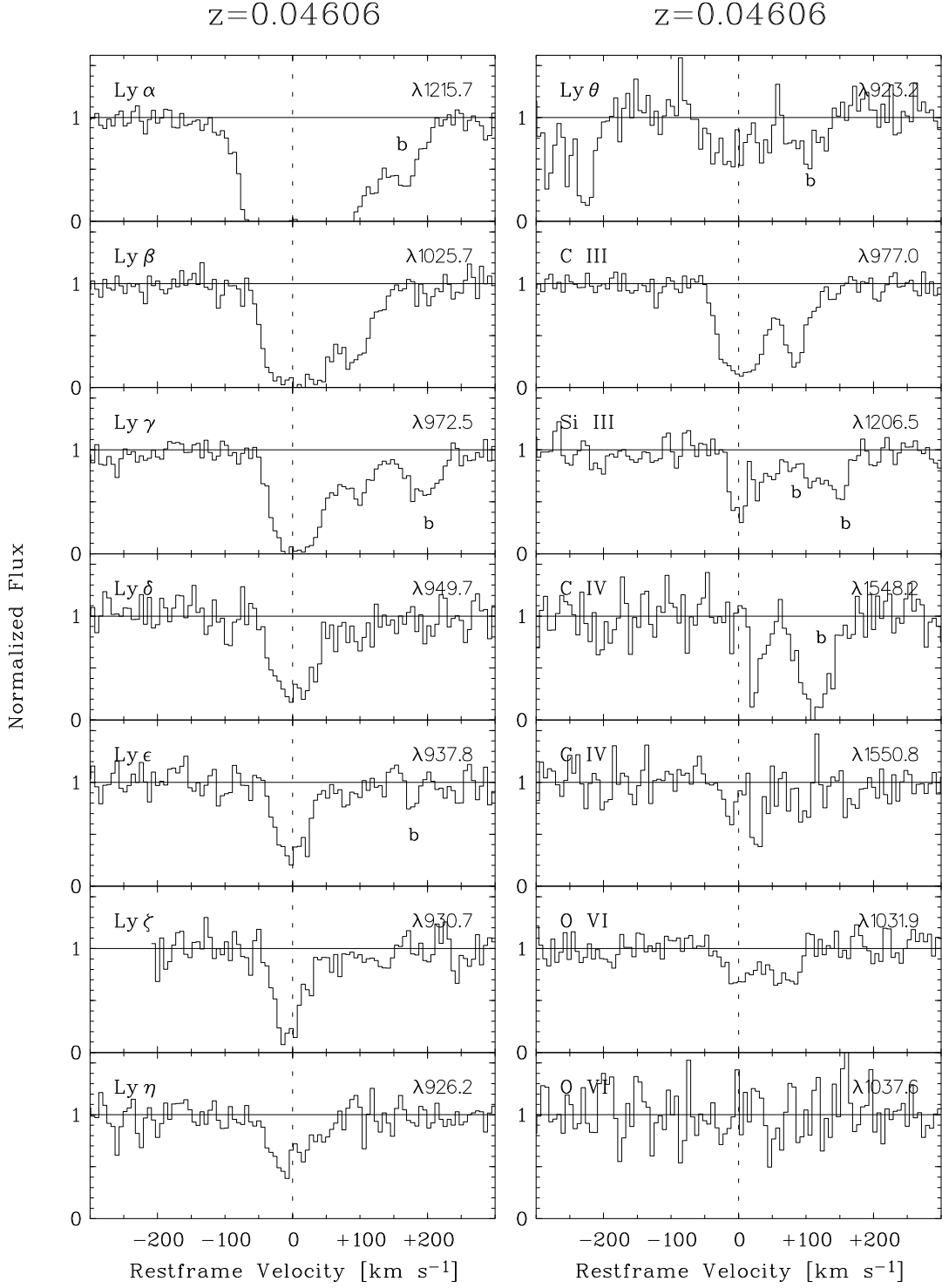


Fig. 15.— Continuum-normalized absorption profiles of multiple-line IGM absorbers towards PG 1259+593 (ctd).

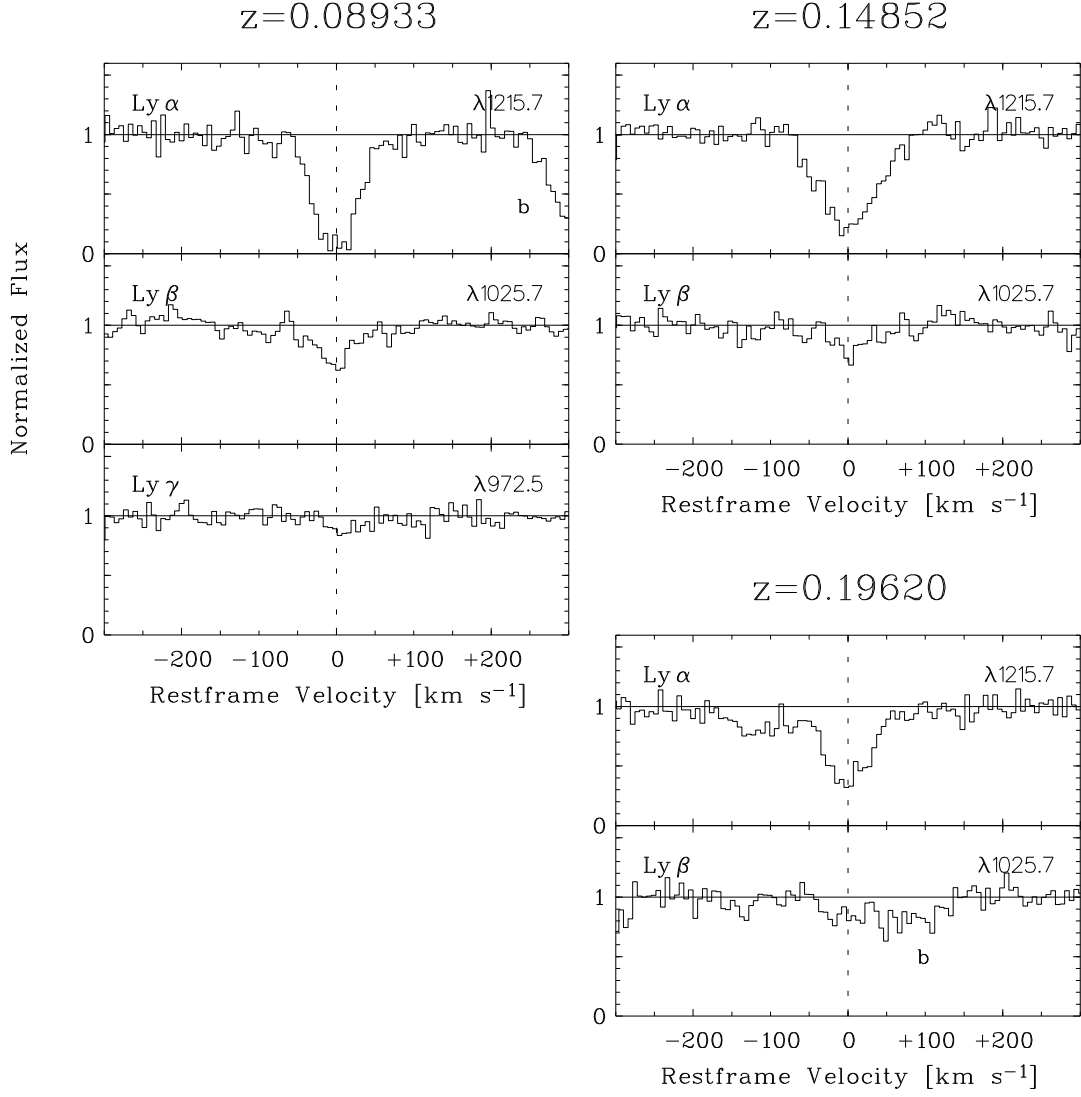


Fig. 16.— Continuum-normalized absorption profiles of multiple-line IGM absorbers towards PG 1259+593 (ctd).

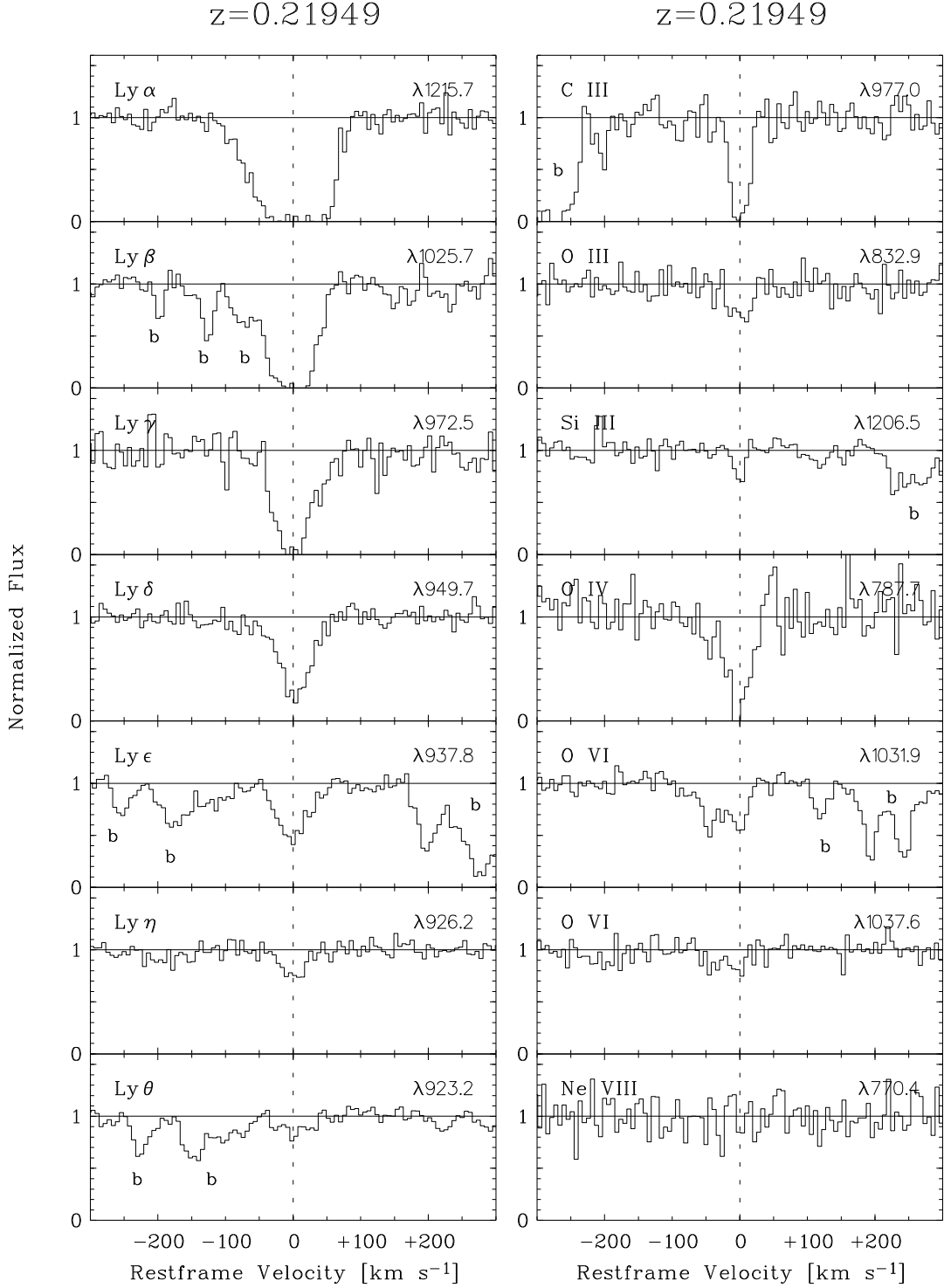


Fig. 17.— Continuum-normalized absorption profiles of multiple-line IGM absorbers towards PG 1259+593 (ctd).

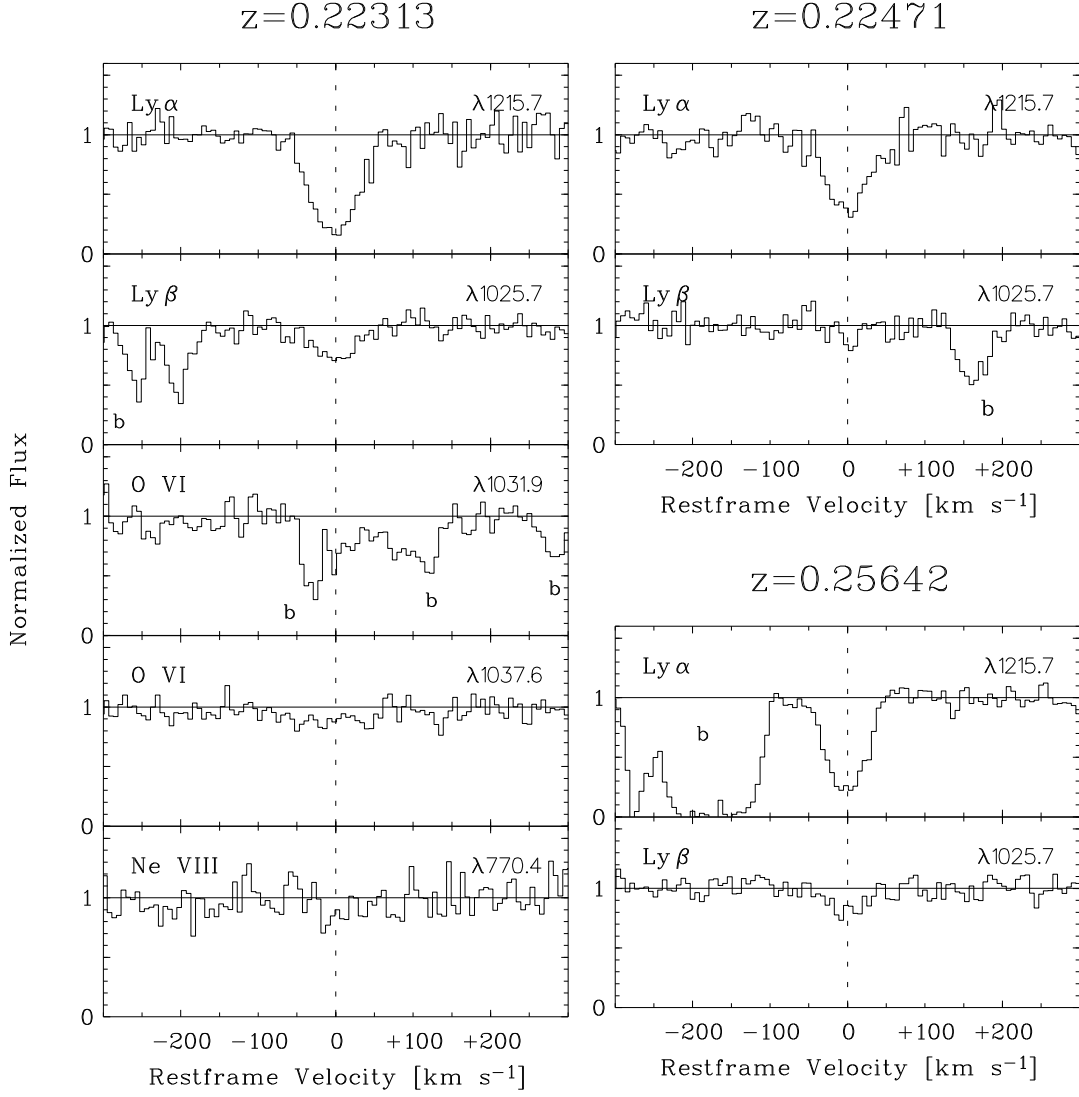




Fig. 18.— Continuum-normalized absorption profiles of multiple-line IGM absorbers towards PG 1259+593 (ctd).

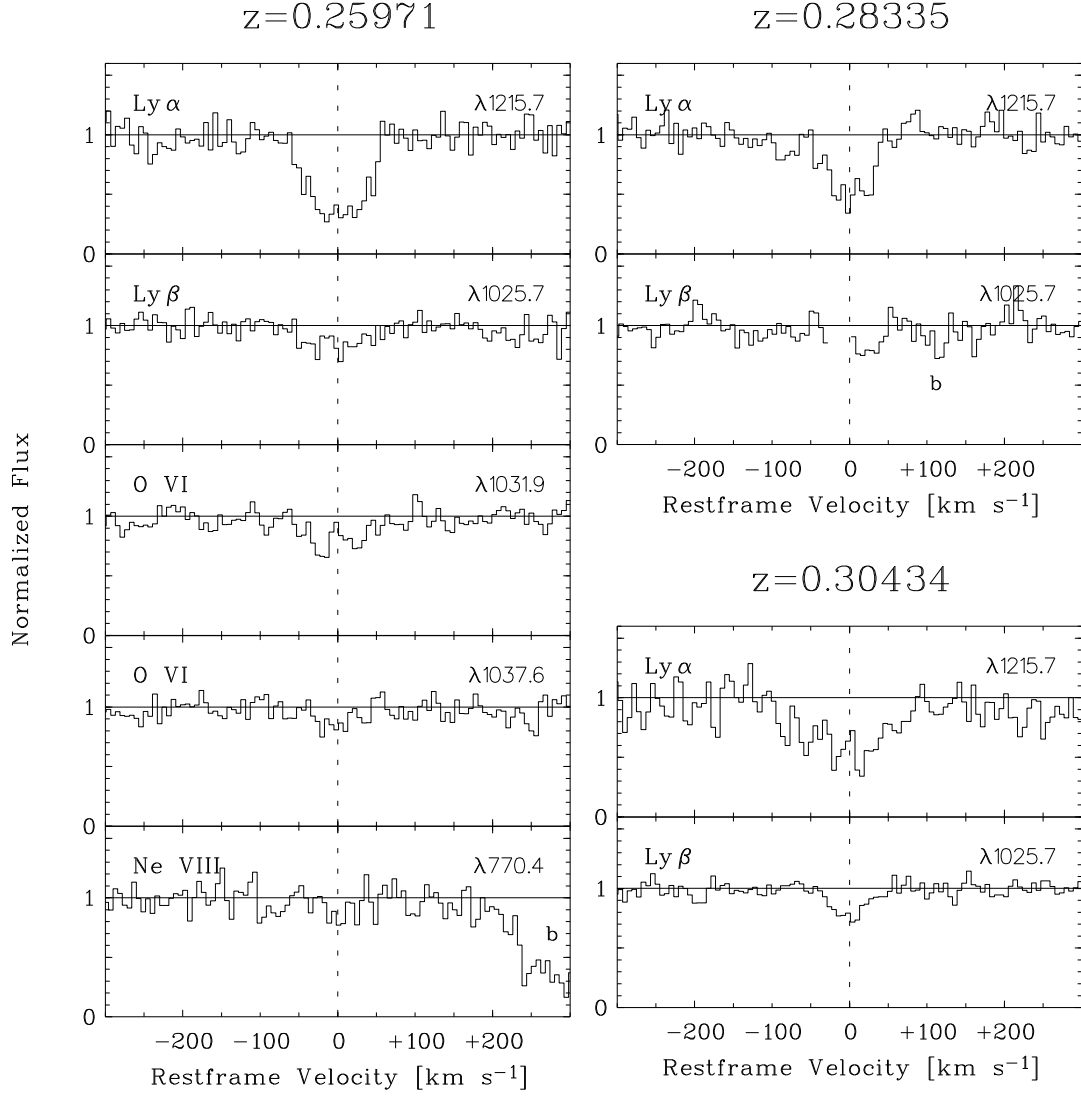


Fig. 19.— Continuum-normalized absorption profiles of multiple-line IGM absorbers towards PG 1259+593 (ctd).

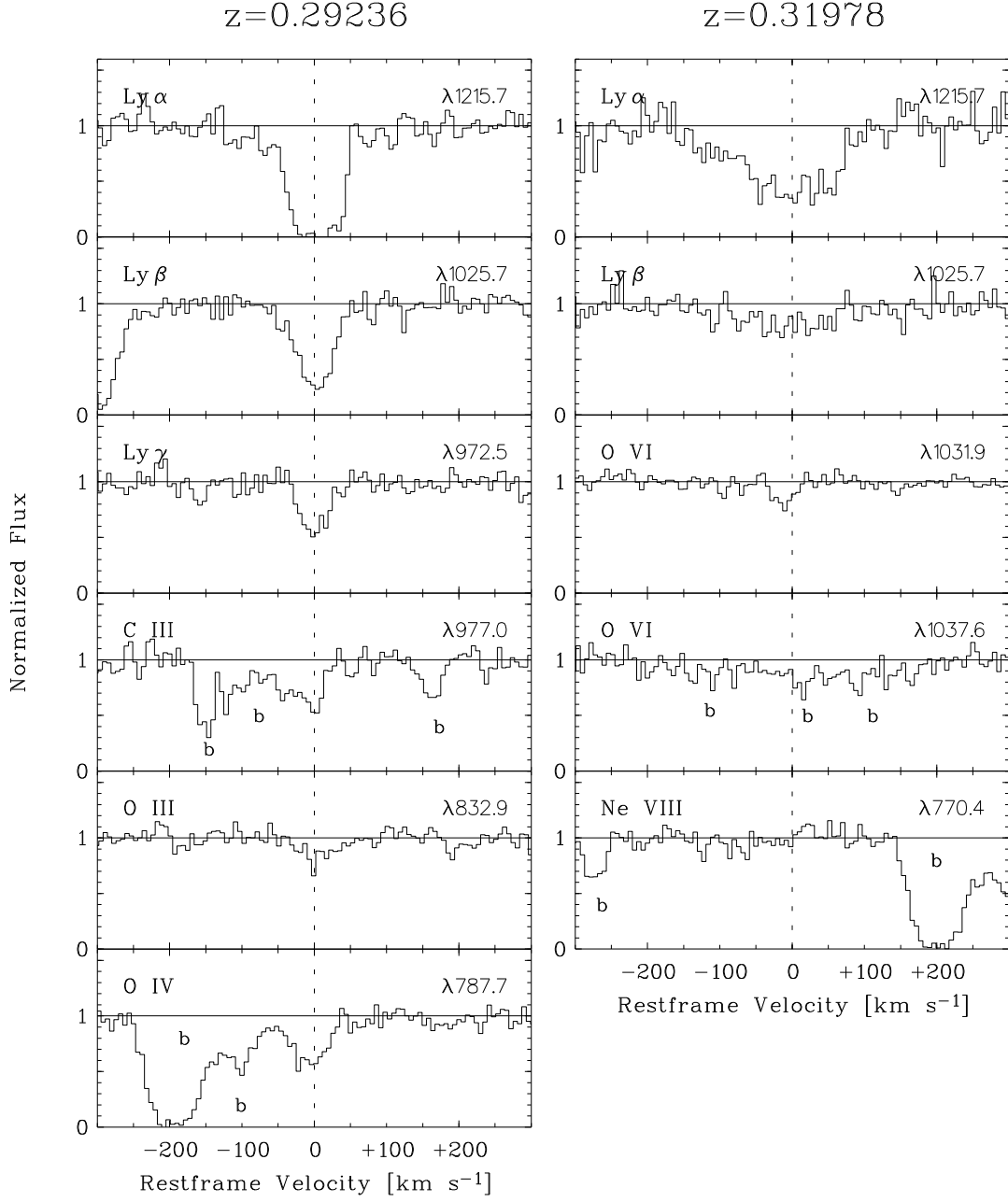


Fig. 20.— Continuum-normalized absorption profiles of multiple-line IGM absorbers towards PG 1259+593 (ctd).

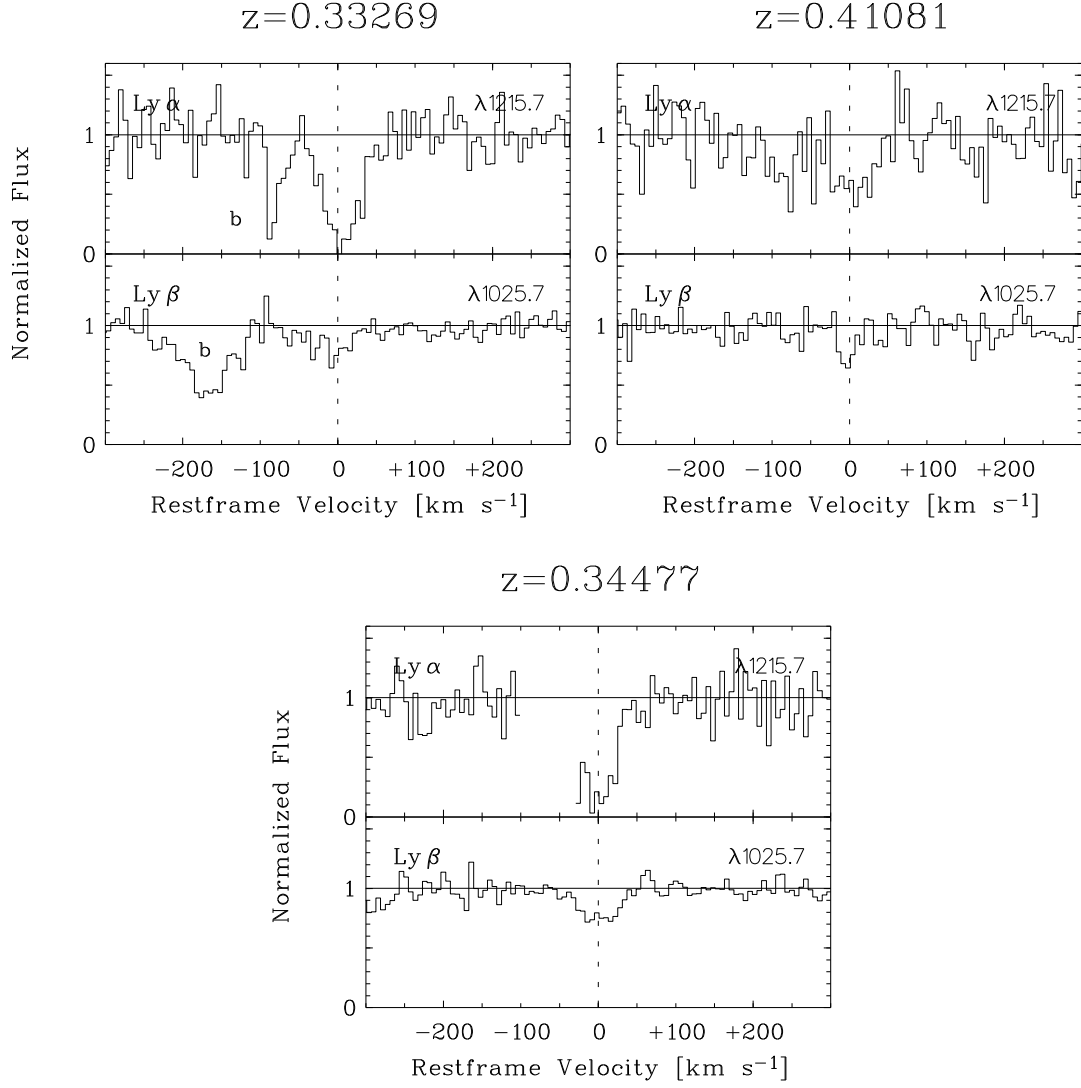


Fig. 21.— Continuum-normalized absorption profiles of multiple-line IGM absorbers towards PG 1259+593 (ctd).

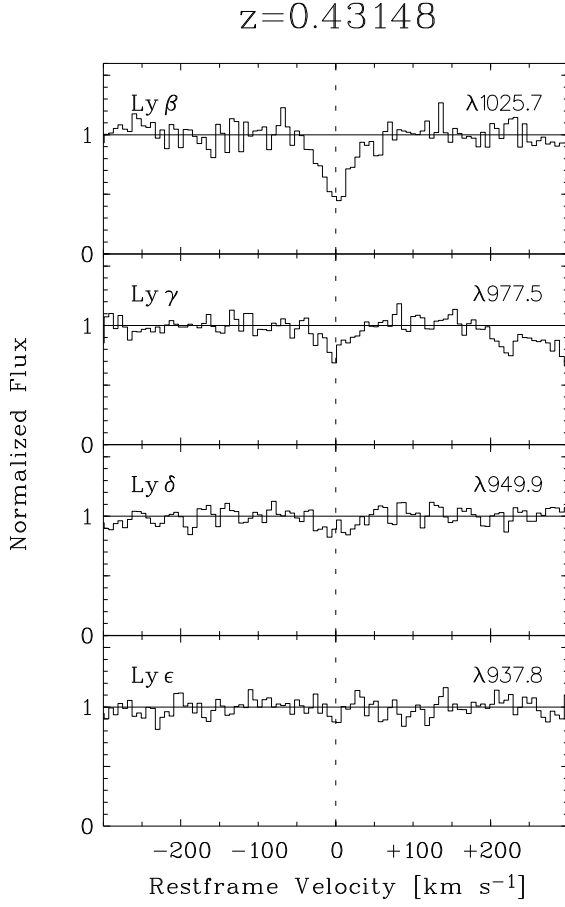


Fig. 22.— *Upper two panels:* Number Distribution of HI  $b$ -values and column densities for all absorption systems (upper left panel and upper right panel, respectively). The thin lines show the distributions for the total sample of available  $b$  values and column densities, whereas the thick lines show the distributions for  $b$  and  $\log N$  excluding the uncertain cases. *Lower Panel:*  $b$  value versus column density. Data points based on uncertain estimates for  $b$  and  $\log N$  (see Table 5 and §3.4.2) are plotted as open circles; data points based on reliable estimates for these parameters are shown as filled circles.

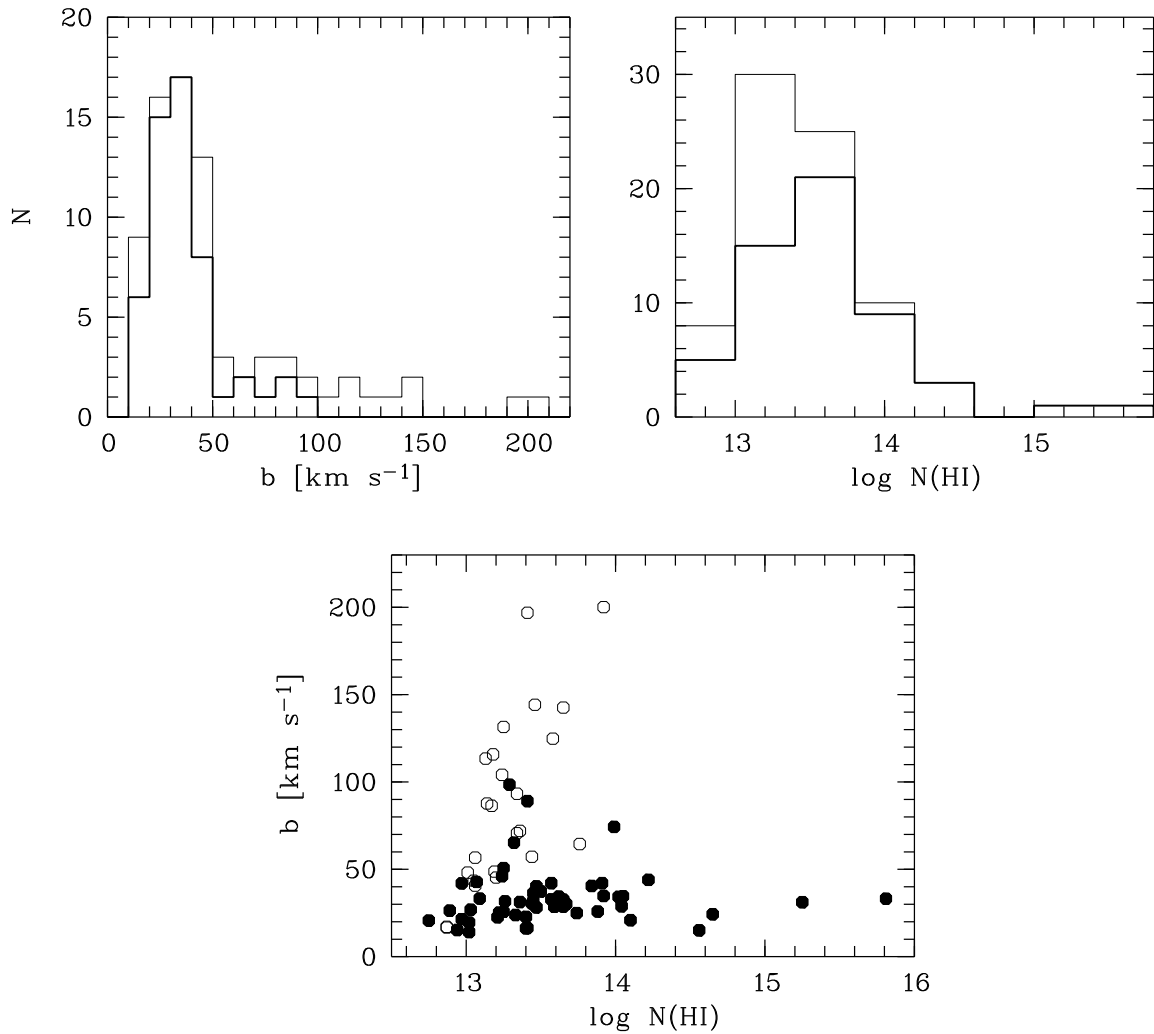


Fig. 23.— Examples for Voigt-profile fits of broad Ly  $\alpha$  lines towards PG 1259+593 (see Table 6). For this plot, the data has been binned to  $30 \text{ km s}^{-1}$  wide pixels. Note that the fitting was performed using unbinned data. Other identified absorption lines in the vicinity of the broad absorption features are labeled in the plot or are indicated with tic marks.

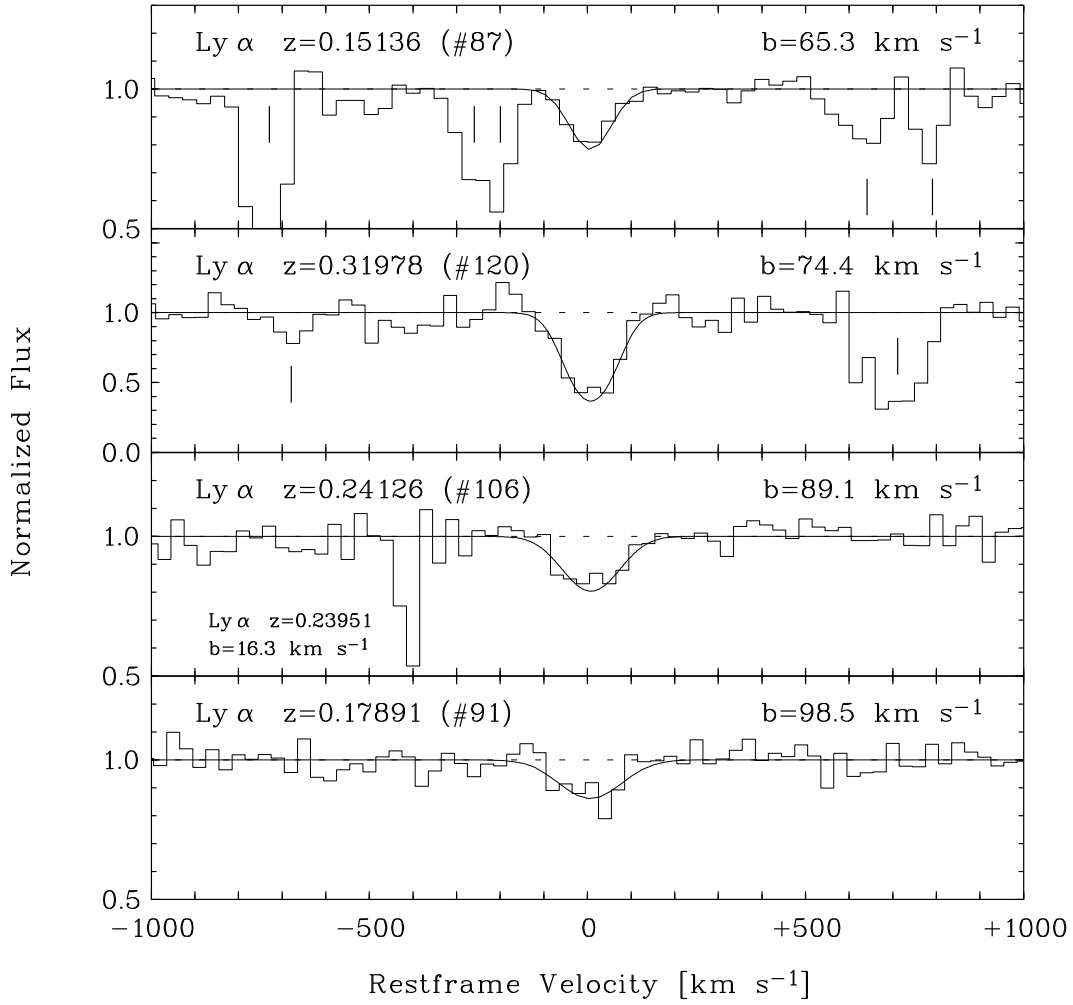


Fig. 24.— Examples for Voigt-profile fits of broad Ly  $\alpha$  candidate lines (uncertain cases) towards PG 1259+593 (see Tables 3 and 5). For this plot, the data has been binned to  $30 \text{ km s}^{-1}$  wide pixels. Note that the fitting was performed using unbinned data.

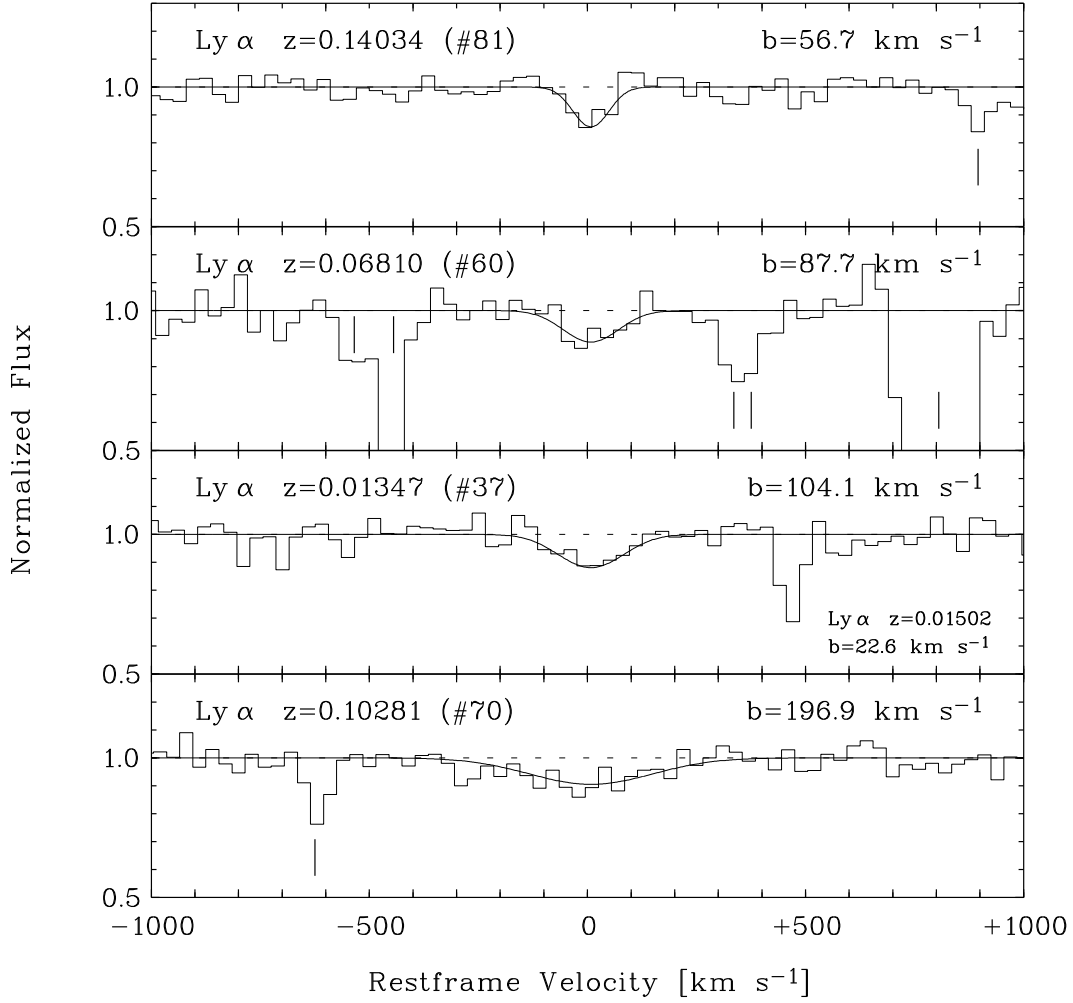


Fig. 25.— Sky positions of PG 1259+593 and UGC 08146 on an image from the *Digitized Sky Survey*. HI contours for UGC 08146 from data of the *Westerbork Synthesis Radio Telescope* (Rhee & van Albada 1996) are overlaid. A HIGHER RESOLUTION VERSION OF THIS FIGURE IS AVAILABLE ON REQUEST.

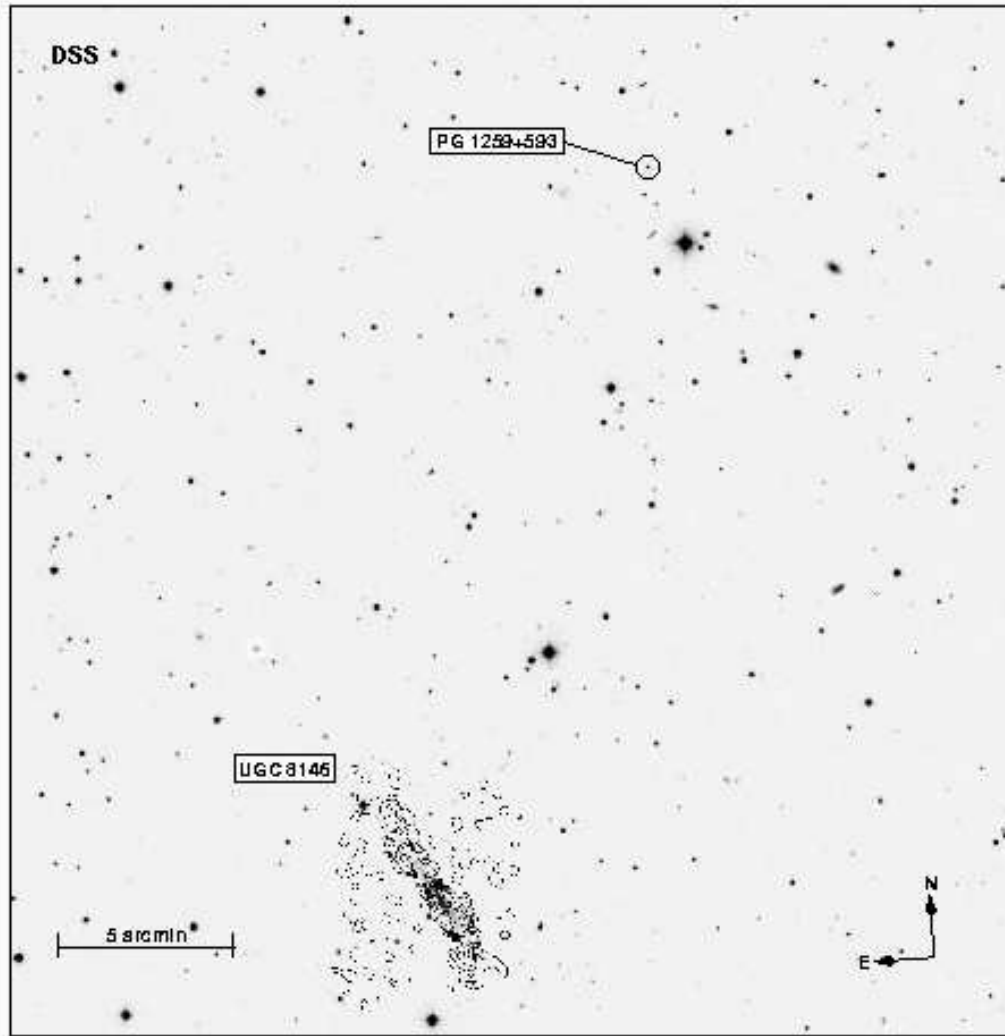




Table 1. Log of FUSE and STIS Observations of PG 1259+593<sup>a</sup>

Instrument	Data Set ID	Obs. Date	Aperture	Exp. Time (ks)	Notes <sup>b</sup>
FUSE	P1080101	2000-Feb-25	30''0 × 30''0	52.4	1
FUSE	P1080102	2000-Dec-25	30''0 × 30''0	56.8	1,2
FUSE	P1080103	2001-Jan-29	30''0 × 30''0	52.0	1,3
FUSE	P1080104	2001-Mar-12	30''0 × 30''0	105.9	1
FUSE	P1080105	2001-Mar-14	30''0 × 30''0	104.0	1
FUSE	P1080106	2001-Mar-17	30''0 × 30''0	63.3	1,3
FUSE	P1080107	2001-Mar-19	30''0 × 30''0	95.7	1
FUSE	P1080108	2001-Mar-22	30''0 × 30''0	33.5	1
FUSE	P1080109	2001-Mar-28	30''0 × 30''0	32.7	1
STIS-E140M	O63G05	2001-Jan-17	0''2 × 0''06	14.4	
STIS-E140M	O63G06	2001-Jan-17	0''2 × 0''06	14.4	
STIS-E140M	O63G07	2001-Jan-18	0''2 × 0''06	14.4	
STIS-E140M	O63G08	2001-Jan-18	0''2 × 0''06	14.4	
STIS-E140M	O63G09	2001-Jan-19	0''2 × 0''06	14.4	
STIS-E140M	O63G11	2001-Jan-19	0''2 × 0''06	9.1	
STIS-E140M	O63G10	2001-Dec-19	0''2 × 0''06	14.4	

<sup>a</sup>This table summarizes the FUSE and STIS observations of PG 1259+593. A more detailed observation log is presented in Sembach et al. (2004).

<sup>b</sup>Notes:

- 1) Exposure time listed represents the exposure time for the LiF 1A channel. The exposure times for the other three channels may be significantly different (see Table 1 in Sembach et al. 2004).
- 2) Alignment problems - no LiF 2, SiC 1 and SiC 2 data.
- 3) Detector high voltage problems during observations.

Table 2. Atomic Data for IGM Absorption Lines<sup>a</sup>

ID	$\lambda_{\text{vac}}$ [Å]	$\log \lambda f$
H I Ly $\alpha$	1215.670	2.704
H I Ly $\beta$	1025.722	1.909
H I Ly $\gamma$	972.537	1.450
H I Ly $\delta$	949.743	1.122
H I Ly $\epsilon$	937.803	0.864
H I Ly $\zeta$	930.748	0.651
H I Ly $\eta$	926.226	0.470
H I Ly $\theta$	923.150	0.311
H I Ly $\iota$	920.963	0.170
H I Ly $\kappa$	919.351	0.043
C III ...	977.020	2.870
C IV ...	1550.777	2.169
	1548.203	2.470
N IV ...	765.148	2.673
O III ...	832.927	1.950
O IV ...	787.711	1.942
O VI ...	1037.617	1.835
	1031.926	2.136
Ne VIII .	780.324	1.596
	770.409	1.900
Si III ...	1206.500	3.304

<sup>a</sup>Wavelengths and  $f$  values are taken from Morton (2003, 1991) and Verner et al. (1994).

Table 3. Multiple-Line IGM Absorbers toward PG 1259+593<sup>a</sup>

ID	No.	$\lambda_{\text{obs}}$ [Å]	$\lambda_{\text{vac}}^b$ [Å]	Instrument	$W_r$ [mÅ]	$v_-$ [km s <sup>-1</sup> ]	$v_+$ [km s <sup>-1</sup> ]	log $N$	$b$ [km s <sup>-1</sup> ]	Method <sup>c</sup>	Comments
$z = 0.00229 \pm 0.00003$											
H I-Ly $\alpha$	31	1218.449	1215.670	STIS E140M	$190 \pm 24$	-110	+80	$13.57 \pm 0.10$	$42.1 \pm 4.4$	PF	
								$13.67 \pm 0.05$	...	AOD	
								$13.61 \pm 0.06$	$44.0^{+9.4}_{-4.1}$	COG	
H I-Ly $\beta$	12	1028.058	1025.722	FUSE LiF 1A	$21 \pm 6$	-85	+85	$13.51 \pm 0.11$	...	AOD	
								$13.61 \pm 0.06$	$44.0^{+9.4}_{-4.1}$	COG	
		1028.103		FUSE LiF 2B	$26 \pm 8$	-95	+95	$13.64 \pm 0.12$	...	AOD	
O VI	14	1034.301	1031.926	FUSE LiF 1A	$63 \pm 22$	-110	+120	$13.73 \pm 0.14$	...	AOD	
								$13.74 \pm 0.09$	44.0	COG <sup>d</sup>	
		1034.312		FUSE LiF 2B	$46 \pm 24$	-130	+150	$13.64 \pm 0.17$	...	AOD	
O VI	...	$\sim 1040.0$	1037.617	FUSE LiF 1A	$\leq 51$	-110	+150	...	...	...	
$z = 0.00760 \pm 0.00002$											
H I-Ly $\alpha$	33	1224.904	1215.670	STIS E140M	$301 \pm 15$	-130	+130	$14.05 \pm 0.05$	$34.6 \pm 2.0$	PF	pos. velocity wing
								$14.03 \pm 0.04$	...	AOD	
								$14.09 \pm 0.04$	$30.6^{+4.9}_{-4.2}$	COG	
H I-Ly $\beta$	13	1033.502	1025.722	FUSE LiF 1A	$75 \pm 6$	-100	+100	$14.07 \pm 0.04$	...	AOD	
								$14.09 \pm 0.04$	$30.6^{+4.9}_{-4.2}$	COG	
		1033.628		FUSE LiF 2B	$60 \pm 9$	-100	+100	$13.98 \pm 0.06$	...	AOD	
O VI	15	1039.771	1031.926	FUSE LiF 1A	$15 \pm 4$	-50	+50	$13.06 \pm 0.04$	...	AOD	
				FUSE LiF 2B	$\leq 9$	-50	+50	...	...	AOD	
$z = 0.02217 \pm 0.00002$											
H I-Ly $\alpha$	39	1242.617	1215.670	STIS E140M	$160 \pm 9$	-90	+90	$13.67 \pm 0.04$	$30.2 \pm 2.2$	PF	
								$13.63 \pm 0.04$	...	AOD	
								$13.58 \pm 0.06$	$34.1^{+11.1}_{-6.0}$	COG	
H I-Ly $\beta$	16	1048.421	1025.722	FUSE LiF 1A	$20 \pm 4$	-45	+60	$13.46 \pm 0.08$	...	AOD	
								$13.58 \pm 0.06$	$34.1^{+11.1}_{-6.0}$	COG	
		$\sim 1048.4$		FUSE LiF 2B	$\leq 27$	-45	+70	...	...	...	
$z = 0.04606 \pm 0.00003$											
H I-Ly $\alpha$	52	1271.812	1215.670	STIS E140M	$878 \pm 29$	-190	+130	...	...	...	incl. Comp. A & B
								$15.58 \pm 0.21$	$47.6 \pm 12.4$	PF	Comp.A; left wing only
H I-Ly $\beta$	18	1073.003	1025.722	FUSE LiF 1A	$377 \pm 17$	-100	+75	$15.81 \pm 0.08$	$33.2^{+6.5}_{-5.1}$	COG	Comp. A ( $v_c \approx 0$ km s <sup>-1</sup> )
					$120 \pm 11$	+76	+160	$14.43 \pm 0.09$	...	AOD	Comp. B ( $v_c \approx +95$ km s <sup>-1</sup> )
								$14.56 \pm 0.15$	$15.1^{+8.4}_{-3.3}$	COG	Comp. B
H I-Ly $\gamma$	9	1017.331	972.537	FUSE LiF 1A	$279 \pm 18$	-70	+70	$15.81 \pm 0.08$	$33.2^{+6.5}_{-5.1}$	COG	Comp. A

Table 3—Continued

ID	No.	$\lambda_{\text{obs}}$ [Å]	$\lambda_{\text{vac}}^{\text{b}}$ [Å]	Instrument	$W_{\text{r}}$ [mÅ]	$v_{-}$ [km s <sup>-1</sup> ]	$v_{+}$ [km s <sup>-1</sup> ]	$\log N$	$b$ [km s <sup>-1</sup> ]	Method <sup>c</sup>	Comments
H I-Ly $\delta$	7	993.451	949.743	FUSE LiF 2B	277 ± 24	-70	+70	15.60 ± 0.12	27.6 <sup>+4.8</sup> <sub>-4.1</sub>	COG	Comp. A
				FUSE LiF 1A	75 ± 13	+71	+150	14.58 ± 0.07	...	AOD	Comp. B
								14.56 ± 0.15	15.1 <sup>+8.4</sup> <sub>-3.3</sub>	COG	Comp. B
				FUSE LiF 2B	69 ± 14	+71	+160	14.55 ± 0.13	...	AOD	Comp. B
H I-Ly $\epsilon$	6	980.978	937.803	FUSE SiC 2A	174 ± 15	-80	+70	15.81 ± 0.08	33.2 <sup>+6.5</sup> <sub>-5.1</sub>	COG	Comp. A
					28 ± 8	+71	+140	14.46 ± 0.11	...	AOD	Comp. B
H I-Ly $\zeta$	5	980.998	930.748	FUSE SiC 2A	146 ± 12	-90	+90	15.81 ± 0.08	33.2 <sup>+6.5</sup> <sub>-5.1</sub>	COG	Comp. A
				FUSE SiC 1B	143 ± 14	-100	+100	15.60 ± 0.12	27.6 <sup>+4.8</sup> <sub>-4.1</sub>	COG	Comp. A
H I-Ly $\eta$	4	973.574	930.748	FUSE SiC 2A	144 ± 13	-70	+80	15.81 ± 0.08	33.2 <sup>+6.5</sup> <sub>-5.1</sub>	COG	Comp. A
				FUSE SiC 1B	95 ± 14	-70	+80	15.60 ± 0.12	27.6 <sup>+4.8</sup> <sub>-4.1</sub>	COG	Comp. A
		968.886	926.226	FUSE SiC 2A	107 ± 19	-80	+90	15.76 ± 0.07	...	AOD	Comp. A
								15.81 ± 0.08	33.2 <sup>+6.5</sup> <sub>-5.1</sub>	COG	Comp. A
H I-Ly $\theta$	3	969.074	923.150	FUSE SiC 1B	132 ± 20	-80	+90	15.88 ± 0.06	...	AOD	Comp. A
								15.60 ± 0.12	27.6 <sup>+4.8</sup> <sub>-4.1</sub>	COG	Comp. A
				FUSE SiC 2A	94 ± 24	-70	+70	15.84 ± 0.11	...	AOD	Comp. A
								15.81 ± 0.08	33.2 <sup>+6.5</sup> <sub>-5.1</sub>	COG	Comp. A
H I-Ly $\kappa$	11	965.707	923.150	FUSE SiC 1B	44 ± 19	-50	+70	15.70 ± 0.15	...	AOD	Comp. A
								15.60 ± 0.12	27.6 <sup>+4.8</sup> <sub>-4.1</sub>	COG	Comp. A
								...	...	...	Comp. A; low S/N
								...	...	...	Comp. A; poss. sat.
C III	11	1022.043	977.020	FUSE SiC 2A	≤ 62	-50	+50	...	...	...	Comp. A; low S/N
				FUSE LiF 1A	209 ± 10	-80	+65	13.80 ± 0.04	...	AOD	Comp. A; poss. sat.
								13.75 ± 0.04	33.2	COG <sup>d</sup>	Comp. A
				FUSE LiF 2B	217 ± 17	-90	+65	13.84 ± 0.04	...	AOD	Comp. A
C IV	123	1022.002	1548.195	FUSE LiF 1A	111 ± 8	+66	+150	13.42 ± 0.04	...	AOD	Comp. B
								13.55 ± 0.07	15.1	COG <sup>d</sup>	Comp. B
				FUSE LiF 2B	100 ± 12	+66	+160	13.43 ± 0.05	...	AOD	Comp. B
				STIS E140M	92 ± 16	-50	+55	13.61 ± 0.08	...	AOD	Comp. A, poss. sat.
O VI	20	1022.043	1031.926					13.73 ± 0.41	7.3 <sup>+8.5</sup> <sub>-4.1</sub>	COG	Comp. A
				...	...	...	Comp. B; blended	...	...	...	...
				...	...	...	...	...	...	...	...
				...	...	...	...	...	...	...	...
O VI	125	1622.350	1550.770	STIS E140M	66 ± 20	-30	+50	13.66 ± 0.12	...	AOD	Comp. A
								13.73 ± 0.41	7.3 <sup>+8.5</sup> <sub>-4.1</sub>	COG	Comp. A
								≤ 13.64	...	AOD	Comp. B
				FUSE LiF 1A	50 ± 7	-70	+40	13.68 ± 0.05	...	AOD	Comp. A
O VI	20	1079.532	1031.926					13.64 ± 0.06	33.2	COG <sup>d</sup>	Comp. A
					45 ± 8	+41	+125	13.63 ± 0.06	...	AOD	Comp. B

Table 3—Continued

ID	No.	$\lambda_{\text{obs}}$ [Å]	$\lambda_{\text{vac}}^b$ [Å]	Instrument	$W_r$ [mÅ]	$v_-$ [km s <sup>-1</sup> ]	$v_+$ [km s <sup>-1</sup> ]	log $N$	$b$ [km s <sup>-1</sup> ]	Method <sup>c</sup>	Comments
O VI	21	~1085.6	1037.617	FUSE SiC 1A	$\leq 47$	-70	+130	$13.70 \pm 0.06$	15.1	COG <sup>d</sup>	Comp. B
Si III	44	1262.060	1206.500	STIS E140M	$81 \pm 13$	-40	+30	$\leq 13.93$	...	AOD	Comp. A & B; low S/N
								$12.74 \pm 0.07$	...	AOD	Comp. A; poss. sat.
								$12.63 \pm 0.08$	33.2	COG <sup>d</sup>	Comp. A
					...	+31	+130	...	...	...	Comp. B; blended
$z = 0.06644 \pm 0.00002$											
H I-Ly $\alpha$	59	1296.440	1215.670	STIS E140M	$162 \pm 12$	-50	+50	$13.65 \pm 0.05$	$28.7 \pm 3.3$	PF	Comp. A ( $v_c \approx 0$ km s <sup>-1</sup> )
								$13.65 \pm 0.06$	...	AOD	Comp. A
					$35 \pm 7$	-141	-51	$13.72 \pm 0.11$	$20.4^{+5.7}_{-3.7}$	COG	Comp. A
					$42 \pm 5$	-70	+70	$12.86 \pm 0.08$	...	AOD	Comp. B ( $v_c \approx -90$ km s <sup>-1</sup> )
H I-Ly $\beta$	22	1093.992	1025.722	FUSE LiF 2A				$13.80 \pm 0.05$	...	AOD	Comp. A
								$13.72 \pm 0.11$	$20.4^{+5.7}_{-3.7}$	COG	Comp. A
$z = 0.08933 \pm 0.00002$											
H I-Ly $\alpha$	65	1324.262	1215.670	STIS E140M	$273 \pm 11$	-100	+100	$14.04 \pm 0.03$	$28.9 \pm 1.7$	PF	
								$14.04 \pm 0.04$	...	AOD	
								$14.05 \pm 0.07$	$27.8^{+1.8}_{-3.2}$	COG	
H I-Ly $\beta$	23	1117.353	1025.722	FUSE LiF 2A	$74 \pm 12$	-90	+90	$14.07 \pm 0.06$	...	AOD	
								$14.05 \pm 0.07$	$27.8^{+1.8}_{-3.2}$	COG	
				FUSE LiF 1B	$68 \pm 8$	-90	+110	$14.02 \pm 0.05$	...	AOD	
H I-Ly $\gamma$	17	1059.413	972.537	FUSE LiF 1A	$24 \pm 4$	-60	+75	$14.02 \pm 0.04$	...	AOD	
								$14.05 \pm 0.07$	$27.8^{+1.8}_{-3.2}$	COG	
				FUSE LiF 2B	$16 \pm 5$	-65	+75	$13.90 \pm 0.07$	...	AOD	
H I-Ly $\delta$	...	~ 1034.6	949.743	FUSE LiF 1A	$\leq 22$	-60	+60	...	...	...	
$z = 0.14852 \pm 0.00003$											
H I-Ly $\alpha$	84	1396.225	1215.670	STIS E140M	$254 \pm 9$	-115	+120	$13.91 \pm 0.06$	$42.1 \pm 2.4$	PF	
								$13.88 \pm 0.04$	...	AOD	
								$13.96 \pm 0.05$	$38.3^{+3.4}_{-3.1}$	COG	
H I-Ly $\beta$	29	1178.173	1025.722	FUSE LiF 1B	$53 \pm 8$	-90	+100	$13.90 \pm 0.06$	...	AOD	
								$13.96 \pm 0.05$	$38.3^{+3.4}_{-3.1}$	COG	
$z = 0.19620 \pm 0.00003$											
H I-Ly $\alpha$	95	1454.186	1215.670	STIS E140M	$201 \pm 14$	-70	+140	$13.65 \pm 0.05$	$32.7 \pm 3.2$	PF	Comp. A ( $v_c \approx 0$ km s <sup>-1</sup> )
								$13.71 \pm 0.04$	...	AOD	Comp. A
								$13.78 \pm 0.08$	$28.8^{+2.2}_{-4.4}$	COG	Comp. A
					$76 \pm 7$	-235	-71	$13.07 \pm 0.14$	$42.8 \pm 7.2$	PF	Comp. B ( $v_c \approx -120$ km s <sup>-1</sup> )

Table 3—Continued

ID	No.	$\lambda_{\text{obs}}$ [Å]	$\lambda_{\text{vac}}^{\text{b}}$ [Å]	Instrument	$W_{\text{r}}$ [mÅ]	$v_{-}$ [km s $^{-1}$ ]	$v_{+}$ [km s $^{-1}$ ]	$\log N$	$b$ [km s $^{-1}$ ]	Method <sup>c</sup>	Comments								
H I-Ly $\beta$	35	1226.996	1025.722	STIS E140M	$41 \pm 7$	$-70$	$+50$	$13.19 \pm 0.04$	$\dots$	AOD	Comp. B								
								$13.79 \pm 0.07$	$\dots$	AOD	Comp. A								
								$13.78 \pm 0.08$	$28.8^{+2.2}_{-4.4}$	COG	Comp. A								
					$\leq 20$	$-200$	$-71$	$\dots$	$\dots$	$\dots$	Comp. B								
$z = 0.21949 \pm 0.00003$																			
H I-Ly $\alpha$	100	1482.429	1215.670	STIS E140M	$552 \pm 26$	$-160$	$+120$	$15.25 \pm 0.06$	$31.2^{+4.1}_{-2.7}$	COG	neg. velocity wing								
H I-Ly $\beta$	40	1250.844	1025.722	STIS E140M	$263 \pm 32$	$-50$	$+80$	$15.08 \pm 0.08$	$32.3 \pm 1.4$	PF	blended by Galactic S II								
H I-Ly $\gamma$	30	1186.000	972.537	STIS E140M	$217 \pm 24$	$-110$	$+100$	$15.25 \pm 0.06$	$31.2^{+4.1}_{-2.7}$	COG									
								$15.32 \pm 0.12$	$29.7 \pm 3.1$	PF									
H I-Ly $\delta$	28	1186.043		FUSE LiF 2A	$\dots$	$\dots$	$\dots$	$\dots$	$\dots$	$\dots$	detector edge								
		1158.204	949.743	FUSE LiF 2A	$148 \pm 10$	$-100$	$+100$	$15.31 \pm 0.04$	$\dots$	AOD									
		27	1158.189		FUSE LiF 1B	$153 \pm 11$	$-120$	$+120$	$15.25 \pm 0.06$	$31.2^{+4.1}_{-2.7}$	COG								
									$15.32 \pm 0.04$	$\dots$	AOD								
H I-Ly $\epsilon$		1143.618	937.804	FUSE LiF 2A	$88 \pm 6$	$-60$	$+70$	$15.17 \pm 0.08$	$30.5^{+5.1}_{-4.6}$	COG									
								$15.27 \pm 0.05$	$\dots$	AOD									
								1143.600		FUSE LiF 1B	$64 \pm 7$	$-70$	$+75$	$15.25 \pm 0.06$	$31.2^{+4.1}_{-2.7}$	COG			
														$15.14 \pm 0.05$	$\dots$	AOD	too weak		
H I-Ly $\eta$	26	1129.574	926.226	FUSE LiF 2A	$35 \pm 4$	$-70$	$+70$	$15.17 \pm 0.08$	$30.5^{+5.1}_{-4.6}$	COG									
								$15.22 \pm 0.05$	$\dots$	AOD									
								1129.459		FUSE LiF 1B	$30 \pm 4$	$-70$	$+75$	$15.25 \pm 0.06$	$31.2^{+4.1}_{-2.7}$	COG			
														$15.17 \pm 0.05$	$\dots$	AOD			
H I-Ly $\theta$	25	1125.792	923.150	FUSE LiF 2A	$25 \pm 6$	$-45$	$+60$	$15.17 \pm 0.08$	$30.5^{+5.1}_{-4.6}$	COG									
								$15.22 \pm 0.09$	$\dots$	AOD									
								1125.814		FUSE LiF 1B	$20 \pm 5$	$-50$	$+60$	$15.25 \pm 0.06$	$31.2^{+4.1}_{-2.7}$	COG			
														$15.11 \pm 0.11$	$\dots$	AOD			
H I-Ly $\iota$	24	1123.122	920.963	FUSE LiF 2A	$17 \pm 3$	$-45$	$+45$	$15.17 \pm 0.08$	$30.5^{+5.1}_{-4.6}$	COG									
								$15.18 \pm 0.07$	$\dots$	AOD									
								1123.074		FUSE LiF 1B	$14 \pm 4$	$-50$	$+55$	$15.25 \pm 0.06$	$31.2^{+4.1}_{-2.7}$	COG			
														$15.13 \pm 0.11$	$\dots$	AOD			
H I-Ly $\kappa$	$\dots$	$\sim 1121.1$	919.351	FUSE LiF 2A	$\leq 15$	$-40$	$+40$	$15.17 \pm 0.08$	$30.5^{+5.1}_{-4.6}$	COG									
								$\dots$	$\dots$	$\dots$	$\dots$	$\dots$	$\dots$	$\dots$	$\dots$				
								C III	31	1191.464	977.020	STIS E140M	$107 \pm 12$	$-70$	$+70$	$13.62 \pm 0.13$	$12.2 \pm 2.4$	PF	narrow; poss. sat.
																$13.64 \pm 0.05$	$\dots$	AOD	

Table 3—Continued

ID	No.	$\lambda_{\text{obs}}$ [Å]	$\lambda_{\text{vac}}^{\text{b}}$ [Å]	Instrument	$W_{\text{r}}$ [mÅ]	$v_{-}$ [km s <sup>-1</sup> ]	$v_{+}$ [km s <sup>-1</sup> ]	log $N$	$b$ [km s <sup>-1</sup> ]	Method <sup>c</sup>	Comments
N IV	1	933.125	765.148	FUSE SiC 2A	$\leq 72$	-80	+80	$13.33 \pm 0.06$ $\leq 13.35$	31.2 ...	COG <sup>d</sup> AOD	uncertain; low S/N
O III	8	1015.790	832.927	FUSE LiF 1A	$36 \pm 5$	-80	+90	$13.82 \pm 0.06$ $13.78 \pm 0.07$ $13.85 \pm 0.08$	...	AOD COG <sup>d</sup> COG <sup>d</sup>	
O IV	2	1015.802	787.711	FUSE LiF 2B	$43 \pm 5$	-80	+90	$13.95 \pm 0.05$	...	AOD	poss. sat.
		960.569		FUSE SiC 2A	$103 \pm 13$	-80	+90	$14.27 \pm 0.05$ $14.37 \pm 0.07$	...	AOD COG <sup>d</sup>	
O VI	44	1258.330	1031.926	FUSE SiC 1B	$65 \pm 16$	-100	+100	$14.21 \pm 0.10$	...	AOD	double peak
				STIS E140M	$90 \pm 7$	-120	+60	$13.96 \pm 0.04$ $13.87 \pm 0.04$	...	AOD COG <sup>d</sup>	
O VI	49	1265.312	1037.617	STIS E140M	$27 \pm 6$	-100	+50	$13.68 \pm 0.06$ $13.68 \pm 0.05$	$16.2 \pm 2.4$ $15.5 \pm 1.9$	PF PF	Comp. B ( $v_{\text{c}} \approx -50$ km s <sup>-1</sup> ) Comp. A ( $v_{\text{c}} \approx 0$ km s <sup>-1</sup> )
								$13.72 \pm 0.08$ $13.87 \pm 0.04$	...	AOD COG <sup>d</sup>	
Si III	98	1471.328	1206.500	STIS E140M	$11 \pm 3$	-50	+50	$12.04 \pm 0.07$ $11.82 \pm 0.10$	$7.9 \pm 2.0$ ...	PF AOD	narrow
Ne VIII	...	$\sim 939.5$	770.409	FUSE SiC 2A	$\leq 38$	-150	+100	$\leq 13.94$	...	AOD	
$z = 0.22313 \pm 0.00002$											
H I-Ly $\alpha$	101	1486.918	1215.670	STIS E140M	$247 \pm 8$	-100	+100	$13.92 \pm 0.04$ $13.88 \pm 0.04$	$34.8 \pm 1.1$ ...	PF AOD	poss. saturated
H I-Ly $\beta$	41	1254.602	1025.722	STIS E140M	$63 \pm 7$	-100	+100	$14.01 \pm 0.06$ $13.99 \pm 0.05$	$25.6^{+3.8}_{-2.5}$ ...	COG AOD	
								$14.01 \pm 0.06$	$25.6^{+3.8}_{-2.5}$	COG	
O VI	46	$\sim 1262.2$	1031.926	STIS E140M	...	...	...	...	...	...	blended
O VI	51	1269.367	1037.617	STIS E140M	$57 \pm 14$	-120	+120	$13.99 \pm 0.11$ $14.02 \pm 0.08$	...	AOD COG <sup>d</sup>	
Ne VIII	...	$\sim 939.5$	770.409	FUSE SiC 2A	$\leq 30$	-100	+100	$\leq 13.75$	...	AOD	
$z = 0.22471 \pm 0.00003$											
H I-Ly $\alpha$	102	1488.849	1215.670	STIS E140M	$169 \pm 12$	-100	+100	$13.59 \pm 0.06$ $13.64 \pm 0.04$	$28.9 \pm 1.7$ ...	PF AOD	too weak
H I-Ly $\beta$	42	1256.198	1025.722	STIS E140M	$16 \pm 4$	-90	+90	$13.57 \pm 0.08$ $13.41 \pm 0.10$	$36.1^{+4.0}_{-3.6}$ ...	COG AOD	
								$13.57 \pm 0.08$	$36.1^{+4.0}_{-3.6}$	COG	

Table 3—Continued

ID	No.	$\lambda_{\text{obs}}$ [Å]	$\lambda_{\text{vac}}^{\text{b}}$ [Å]	Instrument	$W_{\text{r}}$ [mÅ]	$v_{-}$ [km s <sup>-1</sup> ]	$v_{+}$ [km s <sup>-1</sup> ]	$\log N$	$b$ [km s <sup>-1</sup> ]	Method <sup>c</sup>	Comments
$z = 0.25642 \pm 0.00002$											
H I-Ly $\alpha$	107	1527.390	1215.670	STIS E140M	$184 \pm 6$	-80	+90	$13.74 \pm 0.03$	$25.0 \pm 0.9$	PF	
								$13.74 \pm 0.04$	...	AOD	
								$13.73 \pm 0.05$	$27.1^{+3.0}_{-2.4}$	COG	
H I-Ly $\beta$	57	1288.741	1025.722	STIS E140M	$36 \pm 6$	-80	+80	$13.75 \pm 0.06$	...	AOD	
								$13.73 \pm 0.05$	$27.1^{+3.0}_{-2.4}$	COG	
$z = 0.25971 \pm 0.00003$											
H I-Ly $\alpha$	109	1531.396	1215.670	STIS E140M	$249 \pm 10$	-120	+120	$13.84 \pm 0.12$	$40.5 \pm 4.9$	PF	
								$13.80 \pm 0.04$	...	AOD	poss. saturated
								$13.95 \pm 0.05$	$28.2^{+1.8}_{-2.5}$	COG	
H I-Ly $\beta$	58	1292.154	1025.722	STIS E140M	$56 \pm 7$	-100	+120	$13.93 \pm 0.05$	...	AOD	
								$13.95 \pm 0.05$	$28.2^{+1.8}_{-2.5}$	COG	
O VI	61	1299.933	1031.926	STIS E140M	$76 \pm 12$	-110	+110	$13.84 \pm 0.07$	...	AOD	
								$13.83 \pm 0.07$	28.2	COG <sup>d</sup>	
O VI	62	1307.067	1037.617	STIS E140M	$34 \pm 10$	-100	+100	$13.79 \pm 0.11$	...	AOD	
								$13.83 \pm 0.07$	28.2	COG <sup>d</sup>	
Ne VIII	...	$\sim 970.5$	770.409	FUSE SiC 2A	$\leq 43$	-90	+90	$\leq 13.96$	...	AOD	
$z = 0.28335 \pm 0.00003$											
H I-Ly $\alpha$	111	1560.135	1215.670	STIS E140M	$158 \pm 9$	-150	+100	$13.59 \pm 0.10$	$37.0 \pm 5.2$	PF	neg. vel. wing ?
								$13.59 \pm 0.04$	...	AOD	
								$13.61 \pm 0.07$	$28.6^{+5.8}_{-4.2}$	COG	
H I-Ly $\beta$	64	1366.551	1025.722	STIS E140M	$27 \pm 8$	-90	+90	$13.61 \pm 0.13$	...	AOD	uncertain; det. feature
								$13.61 \pm 0.07$	$28.6^{+5.8}_{-4.2}$	COG	
$z = 0.29236 \pm 0.00003$											
H I-Ly $\alpha$	113	1571.050	1215.670	STIS E140M	$404 \pm 19$	-150	+150	$14.65 \pm 0.09$	$24.3 \pm 2.8$	PF	
								$14.50 \pm 0.04$	$31.2^{+3.8}_{-3.1}$	COG	
H I-Ly $\beta$	66	1325.600	1025.722	STIS E140M	$160 \pm 7$	-90	+90	$14.47 \pm 0.05$	$26.2 \pm 1.6$	PF	
								$14.52 \pm 0.04$	...	AOD	
								$14.50 \pm 0.04$	$31.2^{+3.8}_{-3.1}$	COG	
H I-Ly $\gamma$	43	1256.869	972.537	STIS E140M	$59 \pm 5$	-80	+80	$14.50 \pm 0.05$	...	AOD	
								$14.50 \pm 0.04$	$31.2^{+3.8}_{-3.1}$	COG	
H I-Ly $\delta$	36	$\sim 1227.3$	949.743	STIS E140M	...	...	...	...	...	...	present, but blended
C III	47	1262.683	977.020	STIS E140M	$79 \pm 14$	-50	+50	$13.18 \pm 0.07$	...	AOD	uncertain, blended
								$13.17 \pm 0.09$	31.2	COG <sup>d</sup>	



Table 3—Continued

ID	No.	$\lambda_{\text{obs}}$ [Å]	$\lambda_{\text{vac}}^{\text{b}}$ [Å]	Instrument	$W_{\text{r}}$ [mÅ]	$v_{-}$ [km s <sup>-1</sup> ]	$v_{+}$ [km s <sup>-1</sup> ]	log $N$	$b$ [km s <sup>-1</sup> ]	Method <sup>c</sup>	Comments
O III	19	1076.439	832.927	FUSE LiF 1A	$37 \pm 10$	-60	+60	$13.80 \pm 0.06$ $13.79 \pm 0.05$	... 31.2	AOD COG <sup>d</sup>	
O IV	10	1017.979	787.711	FUSE LiF 1A	$72 \pm 6$	-50	+50	$14.16 \pm 0.04$ $14.08 \pm 0.06$	... 31.2	AOD COG <sup>d</sup>	
		1017.945		FUSE LiF 2B	$62 \pm 8$	-55	+55	$14.10 \pm 0.05$	...	AOD	
$z = 0.30434 \pm 0.00003$											
H I-Ly $\alpha$	116	1585.630	1215.670	STIS E140M	$240 \pm 17$	-150	+150	$13.76 \pm 0.14$ $13.76 \pm 0.04$ $13.74 \pm 0.05$	$64.5 \pm 9.6$ ... $54.2^{+7.8}_{-8.6}$	PF AOD COG	Component A ( $v_c \approx 0$ km s <sup>-1</sup> ); broad neg. velocity wing ?
					$192 \pm 44$	+151	+400	$13.48 \pm 0.21$	$124.8 \pm 21.5$	PF	Component B ( $v_c \approx +290$ km s <sup>-1</sup> ); broad; uncertain
H I-Ly $\beta$	57	1337.887	1025.722	STIS E140M	$38 \pm 4$	-90	+90	$13.92 \pm 0.04$	$34.7 \pm 9.6$	PF	narrow; line width
				$13.79 \pm 0.05$	...	AOD	inconsistent with Ly $\alpha$	$13.74 \pm 0.05$	$54.2^{+7.8}_{-8.6}$	COG	
$z = 0.31978 \pm 0.00003$											
H I-Ly $\alpha$	120	1604.411	1215.670	STIS E140M	$389 \pm 16$	-220	+150	$13.98 \pm 0.06$	$74.4 \pm 8.7$	PF	very broad; neg. velocity wing ?
H I-Ly $\beta$	72	1353.713	1025.722	STIS E140M	$110 \pm 13$	-180	+130	$14.07 \pm 0.09$	$62.7 \pm 12.1$	PF	
O IV	...	$\sim 1039.6$	787.711	FUSE LiF 1A	$\leq 14$	-50	+50	$\leq 13.30$	...	AOD	
O VI	74	1361.865	1031.926	STIS E140M	$25 \pm 4$	-65	+60	$13.49 \pm 0.07$ $13.44 \pm 0.06$	$19.3 \pm 4.2$ ...	PF AOD	
O VI	78	$\sim 1369.4$	1037.617	STIS E140M	...	...	...	...	...	...	blended
Ne VIII	...	$\sim 1016.8$	770.409	FUSE LiF 1A	$\leq 15$	-90	+90	$\leq 13.57$	...	AOD	
$z = 0.33269 \pm 0.00003$											
H I-Ly $\alpha$	124	1620.107	1215.670	STIS E140M	$202 \pm 19$	-50	+90	$13.88 \pm 0.08$ $13.76 \pm 0.04$ $13.98 \pm 0.11$	$25.9 \pm 3.2$ ... $19.3^{+5.1}_{-3.6}$	PF AOD COG	poss. saturated
H I-Ly $\beta$	77	1367.029	1025.722	STIS E140M	$58 \pm 10$	-80	+90	$13.94 \pm 0.07$ $13.98 \pm 0.11$	... $19.3^{+5.1}_{-3.6}$	AOD COG	
$z = 0.34477 \pm 0.00005$											
H I-Ly $\alpha$	126	1634.834	1215.670	STIS E140M	...	...	...	...	...	...	detector gap
H I-Ly $\beta$	80	1379.357	1025.722	STIS E140M	$52 \pm 6$	-110	+90	$14.02 \pm 0.08$ $13.91 \pm 0.05$	$34.3 \pm 4.4$ ...	PF AOD	
$z = 0.41081 \pm 0.00004$											
H I-Ly $\alpha$	134	1715.089	1215.670	STIS E140M	$152 \pm 34$	-100	+100	...	...	PF	low S/N; neg. velocity wing ?

Table 3—Continued

ID	No.	$\lambda_{\text{obs}}$ [Å]	$\lambda_{\text{vac}}^{\text{b}}$ [Å]	Instrument	$W_{\text{r}}$ [mÅ]	$v_{-}$ [km s <sup>−1</sup> ]	$v_{+}$ [km s <sup>−1</sup> ]	log $N$	$b$ [km s <sup>−1</sup> ]	Method <sup>c</sup>	Comments
H I-Ly $\beta$	94	1447.101	1025.722	STIS E140M	25 ± 5	−60	+60	13.56 ± 0.12	...	AOD	
								13.57 ± 0.08	32.8 <sup>+6.4</sup> <sub>−4.2</sub>	COG	
								13.60 ± 0.05	...	AOD	
								13.57 ± 0.08	32.8 <sup>+6.4</sup> <sub>−4.2</sub>	COG	
$z = 0.43148 \pm 0.00003$											
H I-Ly $\beta$	97	1468.305	1025.722	STIS E140M	79 ± 5	−100	+100	14.10 ± 0.06	20.9 ± 4.3	PF	
								14.15 ± 0.04	...	AOD	
								14.09 ± 0.07	29.0 <sup>+4.9</sup> <sub>−3.8</sub>	COG	
H I-Ly $\gamma$	83	1392.146	972.537	STIS E140M	22 ± 4	−80	+80	14.04 ± 0.07	...	AOD	
								14.09 ± 0.07	29.0 <sup>+4.9</sup> <sub>−3.8</sub>	COG	
H I-Ly $\delta$	73	1359.501	949.743	STIS E140M	13 ± 4	−70	+70	14.14 ± 0.11	...	AOD	
								14.09 ± 0.07	29.0 <sup>+4.9</sup> <sub>−3.8</sub>	COG	
H I-Ly $\epsilon$	71	1342.494	937.804	STIS E140M	10 ± 4	−50	+50	14.09 ± 0.07	29.0 <sup>+4.9</sup> <sub>−3.8</sub>	COG	
C III	86	1398.715	977.020	STIS E140M	...	...	...	...	...	...	blended
$z = 0.43569 \pm 0.00003$											
H I-Ly $\beta$	99	1472.614	1025.722	STIS E140M	79 ± 9	−90	+90	14.22 ± 0.10	44.0 ± 3.9	PF	aligned with FOS Ly $\alpha^{\text{e}}$
								14.13 ± 0.15	...	AOD	

<sup>a</sup>Equivalent widths, velocities, column densities, and  $b$  values refer to the rest frame. Errors are  $1\sigma$  estimates (see §2.3), upper limits are  $3\sigma$ .

<sup>b</sup>Vacuum wavelengths from Morton (2003, 1999) and Verner et al. (1994).

<sup>c</sup>PF = profile fit; AOD = apparent optical depth method; COG = curve of growth.

<sup>d</sup>Fixed  $b$  value (derived from H I) is used to determine  $\log N$  with the COG method. Note that the  $1\sigma$  error given for  $\log N$  therefore does not include the intrinsic uncertainty for  $b$ .

<sup>e</sup>See Bahcall et al. (1993).

Table 4. Overview Column Densities for Multiple-Line IGM Absorbers<sup>a</sup>

$z$	H I	C III	C IV	O III	O IV	O VI	Si III	Ne VIII
0.00229	13.6	...	...	n.a.	n.a.	(13.7) <sup>b</sup>	...	n.a.
0.00760	14.1	...	...	n.a.	n.a.	(13.1)	...	n.a.
0.02217	13.7	...	...	n.a.	n.a.	...	...	n.a.
0.04606 A	15.8	13.8	13.6	n.a.	n.a.	13.7	12.7	n.a.
0.04606 B	14.5	13.4	$\leq 13.6$	n.a.	n.a.	13.6	bld.	n.a.
0.06644 A	13.7	...	...	n.a.	n.a.	...	...	n.a.
0.06644 B	12.9	...	...	n.a.	n.a.	...	...	n.a.
0.08933	14.0	...	...	n.a.	n.a.	...	...	n.a.
0.14852	13.9	...	n.a.	...	n.a.	...	...	n.a.
0.19620 A	13.7	...	n.a.	...	...	...	...	...
0.19620 B	13.1	...	n.a.	...	...	...	...	...
0.21949	15.2	13.6	n.a.	13.8	14.3	14.0 <sup>c</sup>	12.0	$\leq 13.9$
0.22313	13.9	...	n.a.	...	...	(14.0)	...	$\leq 13.8$
0.22471	13.6	...	n.a.	...	...	...	...	...
0.25642	13.7	...	n.a.	...	...	...	...	...
0.25971	13.8	...	n.a.	...	...	13.8	...	$\leq 14.0$
0.28335	13.6	...	n.a.	...	...	...	...	...
0.29236	14.5	13.2	n.a.	13.8	14.2	...	...	...
0.30434 A	13.7	...	n.a.	...	...	...	...	...
0.30434 B	13.6	...	n.a.	...	...	...	...	...
0.31978	14.0	...	n.a.	...	...	(13.4)	...	$\leq 13.6$
0.33269	13.9	...	n.a.	...	...	...	...	...
0.34477	13.9	...	n.a.	...	...	...	...	...
0.41081	13.6	...	n.a.	...	...	...	...	...
0.43148	14.1	bld.	n.a.	...	...	...	...	...
0.43569	14.1	...	n.a.	...	...	...	n.a.	...

<sup>a</sup>The following abbreviations are used: ...= species not detected; n.a.= species not available in the FUSE and STIS bandpass; bld.= blending problems.

<sup>b</sup>Column densities for tentative detections are given in brackets.

<sup>c</sup>Total O VI column density for the two components (see §3.2.4).

Table 5. Probable and Possible Single-Line Ly  $\alpha$  Absorbers towards PG 1259+593<sup>a</sup>

No.	$z$	$\lambda_{\text{obs}}$ [Å]	$W_{\lambda}$ [mÅ]	$\log N^{\text{b}}$	$b^{\text{b}}$ [km s <sup>-1</sup> ]	Status <sup>c</sup>	Comments
33A	0.00440	1221.024	215 ± 24 :	13.65 ± 0.14 :	142.6 ± 29.4 :	UC	Component A
33B	0.00505	1221.812	133 ± 20 :	13.44 ± 0.10 :	57.2 ± 8.9 :	UC	Component B
37	0.01347	1232.046	90 ± 17 :	13.24 ± 0.14 :	104.1 ± 17.5 :	UC	...
38	0.01502	1233.924	73 ± 6	13.21 ± 0.06	22.6 ± 4.4	OK	...
48	0.03924	1263.372	41 ± 5	12.94 ± 0.05	15.3 ± 2.8	OK	...
50	0.04250	1267.334	58 ± 7 :	13.06 ± 0.06 :	40.7 ± 4.9 :	UC	...
53	0.05112	1277.819	168 ± 9	13.62 ± 0.07	34.4 ± 2.5	OK	pos. vel. wing <sup>d</sup>
54	0.05257	1279.576	28 ± 6	12.75 ± 0.06	20.7 ± 3.0	OK	...
55	0.05376	1281.024	119 ± 7	13.44 ± 0.04	30.5 ± 1.9	OK	...
56	0.05586	1283.572	149 ± 20 :	13.46 ± 0.14 :	144.2 ± 27.9 :	UC	...
60	0.06810	1298.456	72 ± 10 :	13.14 ± 0.09 :	87.7 ± 9.2 :	UC	poss. mult. comp. <sup>e</sup>
63	0.08041	1313.423	45 ± 7	12.97 ± 0.10	42.0 ± 4.5	OK	...
67	0.09196	1327.468	72 ± 22 :	13.13 ± 0.21 :	113.4 ± 29.2 :	UC	neg. vel. wing <sup>f</sup>
68	0.09591	1332.267	45 ± 5	12.97 ± 0.03	21.5 ± 2.3	OK	...
70	0.10281	1340.654	136 ± 18 :	13.41 ± 0.17 :	196.9 ± 31.2 :	UC	poss. mult. comp. <sup>e</sup>
75	0.12188	1363.834	53 ± 8	13.03 ± 0.07	26.9 ± 4.2	OK	...
76	0.12387	1366.252	124 ± 10	13.47 ± 0.06	28.2 ± 3.0	OK	...
79	0.13351	1377.977	53 ± 11 :	13.01 ± 0.08 :	48.1 ± 4.3 :	UC	...
81	0.14034	1386.276	60 ± 10 :	13.06 ± 0.07 :	56.7 ± 5.4 :	UC	...
82	0.14381	1390.498	80 ± 15 :	13.18 ± 0.13 :	115.8 ± 9.6 :	UC	...
85A	0.15029	1398.405	82 ± 9	13.25 ± 0.11	25.7 ± 4.3	OK	Component A
85B	0.15058	1398.722	124 ± 14	13.45 ± 0.13	32.0 ± 5.1	OK	Component B
87	0.15136	1399.668	106 ± 9	13.32 ± 0.09	65.3 ± 5.5	OK	...
88	0.15435	1403.311	77 ± 4	13.22 ± 0.04	25.2 ± 1.9	OK	...
89	0.16647	1418.044	113 ± 13 :	13.34 ± 0.08 :	93.3 ± 8.9 :	UC	poss. neg. vel. comp. <sup>g</sup>
90	0.17148	1424.130	94 ± 19 :	13.25 ± 0.16 :	131.5 ± 17.4 :	UC	...
91	0.17891	1433.167	101 ± 10	13.29 ± 0.10	98.5 ± 9.1	OK	...
92	0.18550	1441.174	77 ± 11 :	13.17 ± 0.12 :	86.4 ± 10.0 :	UC	...
93	0.18650	1442.390	50 ± 4	13.02 ± 0.03	19.6 ± 1.4	OK	...
96	0.19775	1456.070	92 ± 8	13.33 ± 0.06	23.9 ± 2.8	OK	pos. vel. wing <sup>d</sup>
103	0.22861	1493.587	133 ± 10	13.47 ± 0.05	40.3 ± 2.9	OK	...
104	0.23280	1498.676	140 ± 12	13.50 ± 0.07	37.4 ± 3.2	OK	...

Table 5—Continued

No.	$z$	$\lambda_{\text{obs}}$ [Å]	$W_{\lambda}$ [mÅ]	$\log N^{\text{b}}$	$b^{\text{b}}$ [km s $^{-1}$ ]	Status $^{\text{c}}$	Comments
105	0.23951	1506.835	$92 \pm 5$	$13.40 \pm 0.03$	$16.3 \pm 1.3$	OK	...
106	0.24126	1508.963	$130 \pm 12$	$13.41 \pm 0.09$	$89.1 \pm 6.9$	OK	...
108	0.25875	1530.230	$35 \pm 10 :$	$12.87 \pm 0.09 :$	$16.6 \pm 4.1 :$	UC	...
110	0.28014	1556.227	$36 \pm 6 :$	$12.87 \pm 0.05 :$	$17.1 \pm 1.8 :$	UC	...
112	0.28853	1566.428	$111 \pm 16 :$	$13.34 \pm 0.11 :$	$70.7 \pm 8.5 :$	UC	...
114	0.29847	1578.515	$61 \pm 9$	$13.09 \pm 0.10$	$33.3 \pm 2.9$	OK	...
115	0.30164	1582.366	$86 \pm 12$	$13.26 \pm 0.14$	$31.7 \pm 4.7$	OK	...
117	0.30906	1591.389	$78 \pm 9 :$	$13.20 \pm 0.10 :$	$45.3 \pm 5.0 :$	UC	...
118	0.31070	1593.370	$103 \pm 9$	$13.40 \pm 0.07$	$22.8 \pm 2.9$	OK	...
119	0.31682	1600.816	$62 \pm 14 :$	$13.05 \pm 0.17 :$	$43.5 \pm 6.4 :$	UC	...
121	0.32478	1610.496	$86 \pm 12$	$13.24 \pm 0.15$	$46.1 \pm 10.2$	OK	...
122	0.33128	1618.397	$45 \pm 13 :$	$12.98 \pm 0.24 :$	$18.6 \pm 3.5 :$	UC	...
127	0.34802	1638.750	$78 \pm 14 :$	$13.19 \pm 0.14 :$	$48.7 \pm 6.2 :$	UC	...
128	0.34914	1640.112	$103 \pm 11$	$13.36 \pm 0.09$	$31.3 \pm 4.8$	OK	...
129	0.35375	1645.719	$94 \pm 8$	$13.41 \pm 0.06$	$16.4 \pm 1.8$	OK	...
130	0.37660	1673.489	$127 \pm 15$	$13.45 \pm 0.13$	$36.4 \pm 6.2$	OK	...
131	0.37909	1676.519	$116 \pm 19 :$	$13.36 \pm 0.15 :$	$72.0 \pm 8.9 :$	UC	neg. vel. wing $^{\text{f}}$
133	0.38266	1680.862	$403 \pm 77 :$	$13.92 \pm 0.42 :$	$200.1 \pm 22.8 :$	UC	poss. mult. comp. $^{\text{f}}$
134	0.38833	1687.753	$47 \pm 13$	$13.02 \pm 0.19$	$14.1 \pm 3.8$	OK	...
135	0.41786	1723.654	$88 \pm 10$	$13.25 \pm 0.08$	$50.7 \pm 3.9$	OK	pos. vel. wing. $^{\text{d}}$

$^{\text{a}}$ We list in this table all unidentified statistically significant absorption lines with  $\lambda > 1218$  Å observed in the spectrum of PG 1259+593. Most of these lines probably are Ly  $\alpha$  absorbers although the lines are too weak to confirm with a detection of Ly  $\beta$ . The very broad and weak lines listed could be undulations in the continuum of PG 1259+593, broad Ly  $\alpha$  absorbers, or weak complex multi-component Ly  $\alpha$  absorbers.

$^{\text{b}}$ Values for  $\log N$  and  $b$  from lines that are flagged as uncertain (UC; see below) are marked with a colon behind the numbers.

$^{\text{c}}$ The status of a line is either uncertain (UC) or OK. The flag UC is given to those lines for which we see evidence that effects such as continuum undulations, unresolved line blending, fixed-pattern features, etc. are possibly influencing the significance of the detection of a true IGM feature or add an additional

uncertainty for determining  $\log N$  and  $b$  that is not accounted for in the formal  $1\sigma$  error estimate listed (see also §2.3).

<sup>d</sup>ine shows a positive-velocity wing.

<sup>e</sup>ine shows evidence for a multi-component structure.

<sup>f</sup>ine shows a negative-velocity wing.

<sup>g</sup>ine shows evidence for an additional component at negative velocities.

Table 6. Broad Ly  $\alpha$  Absorbers towards PG 1259+593<sup>a</sup>

No.	$z$	$\lambda_{\text{obs}}$ [Å]	$\log N(\text{H I})$	$b(\text{H I})$ [km s <sup>-1</sup> ]	$T^{\text{b}}$ [10 <sup>5</sup> K]	$\log f_{\text{H}}^{\text{c}}$	$\log N(\text{H}^0 + \text{H}^+)^{\text{d}}$
Broad Ly $\alpha$ systems without O VI detection							
103	0.22861	1493.587	$13.47 \pm 0.05$	$40.3 \pm 2.9$	$\leq 0.98$	$\leq 4.83$	$\leq 18.30$
63	0.08041	1313.423	$12.97 \pm 0.10$	$42.0 \pm 4.5$	$\leq 1.06$	$\leq 4.90$	$\leq 17.87$
84	0.14852	1396.225	$13.91 \pm 0.06$	$42.1 \pm 2.4$	$\leq 1.07$	$\leq 4.91$	$\leq 18.82$
95B	0.19620	1454.186	$13.07 \pm 0.14$	$42.8 \pm 7.2$	$\leq 1.10$	$\leq 4.94$	$\leq 18.01$
99 <sup>e</sup>	0.43569	1472.614 <sup>e</sup>	$14.22 \pm 0.10$	$44.0 \pm 3.9$	$\leq 1.16$	$\leq 4.99$	$\leq 19.21$
121	0.32478	1610.496	$13.24 \pm 0.15$	$46.1 \pm 10.2$	$\leq 1.28$	$\leq 5.07$	$\leq 18.31$
87	0.15136	1399.668	$13.32 \pm 0.09$	$65.3 \pm 5.5$	$\leq 2.56$	$\leq 5.65$	$\leq 18.97$
106	0.24126	1508.963	$13.41 \pm 0.09$	$89.1 \pm 6.9$	$\leq 4.76$	$\leq 6.12$	$\leq 19.53$
91	0.17891	1433.167	$13.29 \pm 0.10$	$98.5 \pm 9.1$	$\leq 5.83$	$\leq 6.26$	$\leq 19.55$
Broad Ly $\alpha$ systems with O VI detection							
32	0.00229	1218.449	$13.57 \pm 0.10$	$42.1 \pm 4.4$	$\leq 1.07$	$\leq 4.91$	$\leq 18.48$
120	0.31978	1604.410	$13.99 \pm 0.09$	$74.3 \pm 11.5$	$\leq 3.32$	$\leq 5.91$	$\leq 19.90$

<sup>a</sup>Broad Ly  $\alpha$  absorbers (including one Ly  $\beta$  line) without evidence for blending and sub-component structure are listed.

<sup>b</sup>A limit for  $T$  is listed assuming the line broadening is dominated by thermal Doppler broadening.

<sup>c</sup> $\log f_{\text{H}} = \log (\text{H}^+ / \text{H}^0)$  assuming the gas is in collisional ionization equilibrium at the estimated temperature.

<sup>d</sup>Estimated total hydrogen column density in each system.

<sup>e</sup>Broad Ly  $\beta$  line. Corresponding Ly  $\alpha$  absorption is redwards of the available STIS wavelength range.



Table 7. Galaxies and Galaxy Groups in the General Direction of PG 1259+593<sup>a</sup>

ID	Type <sup>b</sup>	$\alpha$ (2000)	$\delta$ (2000)	Ang. Sep. [arcmin]	$z_{\text{gal}}$	$z_{\text{near.abs.}}$	$\rho_{75}$ [kpc]
PG 1259+593	QSO	13 01 12.9	+59 02 06	...	0.47780	...	...
1259+5920 (+0270−0313)	G	13 01 16.4	+59 01 35	0.7	0.19670	0.19620	120
1259+5920 (−0234+0685)	G	13 01 09.8	+59 03 15	1.2	0.24120	0.24126	248
CGCG 294-006	G	12 59 26.1	+59 01 06	13.8	0.04683	0.04606	701
UGC 08146	G	13 02 08.1	+58 42 05	21.3	0.00224	0.00229	55
Mrk 0233	G	12 58 29.7	+59 07 57	21.8	0.02762	0.02217	671
SBS 1256+596	G	12 58 25.8	+59 21 53	29.1	0.02840	0.02217	922
Mrk 0232	G	12 57 17.5	+59 04 02	30.3	0.02152	0.02217	735
SBS 1304+594	G	13 06 07.1	+59 13 03	39.3	0.03219	0.03924	1403
CGCG 294−015	G	13 06 36.9	+58 45 51	44.9	0.02805	0.02217	1405
FGC 1524	G	12 55 47.1	+59 21 52	46.1	0.04295	0.04606	2165
UGC 08046	G	12 55 04.0	+58 47 25	49.8	0.00858	0.00760	491
CGCG 239−042	G	12 54 49.8	+58 52 56	50.2	0.00861	0.00760	496
WBL 425	GGr	12 54 38.0	+58 49 45	52.4	0.00850	0.00760	512
UGC 08040	G	12 54 43.5	+58 46 36	52.6	0.00839	0.00760	507
SBS 1252+591	G	12 54 22.5	+58 53 42	53.6	0.00828	0.00760	509
Mahtessian 185	GGr	12 54 56.2	+58 32 46	56.9	0.00953	0.00760	622

<sup>a</sup>Based on a search in the NED data archive available at <http://nedwww.ipac.caltech.edu> with a search radius of 60'0 centered on PG 1259+593.

<sup>b</sup>QSO = quasar; G = galaxy; GGr = galaxy group.